1-19-2022 2:30 PM

Evaluation of clamp-on ultrasonic liquid flowmeters

Muhammad Ali, *The University of Western Ontario*

Supervisor: Savory, Eric, *The University of Western Ontario*

A thesis submitted in partial fulfillment of the requirements for the Master of Engineering Science degree in Mechanical and Materials Engineering

Abstract

The clamp-on ultrasonic flowmeter measures the fluid flow velocity and flowrate with the help of ultrasonic waves. Flow profile distortion due to pipe network disturbances cause uncertainty in the flowrate measurement. A numerical and experimental investigation is conducted to model the performance of a clamp-on ultrasonic flowmeter on a straight pipe and at x/d=1 downstream of a 90^0 elbow for the flowrate range of 0.3-2.5m^3/hr. The average percentage error in the flowrate at x/d=1 downstream of the elbow estimated from the numerical and experimental study is 8.6% and 10.8% respectively. The correction factors suggested for the numerical and experimental data reduces the average percentage error to 0.7% and 2.3% respectively. The repeatability tests show ±1.8% uncertainty in the flowrate. Integrating velocity along the acoustic path can roughly estimate measurement uncertainty due to flow profile without simulating the ultrasonic wave propagation numerically. This research will help increase the use of clamp-on ultrasonic flowmeters in practical applications with reduced uncertainty.

Keywords

Clamp-on ultrasonic flowmeters, Liquid metering, correction factors, reducing uncertainty in the flowrate measurement

Summary for Lay Audience

Various different types of flowmeters are used to measure the flowrate of a liquid inside a pipe but this thesis focuses on a clamp-on ultrasonic liquid flowmeter. A clamp-on ultrasonic flowmeter sends and receives ultrasonic signals between its two transducers which are clamped on the outer side of a pipe. The ultrasonic signal that propagates in the direction of the fluid flow travels faster when compared to the ultrasonic signal that travels in the opposite direction of the fluid flow. The time difference between the two signals and the time taken by the individual signals to propagate inside the fluid is used to estimate the fluid velocity and volume flowrate. The disturbance in the fluid flow profile due to pipe bends causes an error in the readings of these flowmeters. In this thesis, a 3D numerical approach to model the working of a clamp-on ultrasonic flowmeter in the presence of a fluid flow inside a straight pipe and downstream of a 90^0 elbow is proposed. An experimental study is also conducted to investigate the performance of an existing clamp-on ultrasonic flowmeter in both conditions. A percentage error due to the distorted fluid flow profile at the downstream of an elbow is observed in the numerical and experimental study. Correction factors are proposed which could be applied to such flowmeters installed in similar flow conditions to reduce the uncertainty in the measurement. This study contributes towards further development in the existing clamp-on ultrasonic flowmeters and will also help in the use of these flowmeters in practical applications with greater accuracy.

Acknowledgments

First and foremost, I would like to express sincere gratitude to my research supervisor Dr. Eric Savory, who has been very supportive throughout the completion of the thesis. His valuable knowledge, productive feedback and constant encouragement guided me during the MESc. program. His vision of research and different perspective of a research outcome has guided me enormously. He has always been available for constructive discussions on my research and related topics. I would like to thank him for providing funds to acquire the licenses of the software's used in this research and related computational resources. I would also like to thank Professor C.T. DeGroot and Professor Kelly Ogden for being my advisory committee members.

I would also like to acknowledge the support, I received from my colleagues in the Advanced Fluid Mechanics Group. They have been very supportive throughout my research progression and always been available for discussion.

I would also like to acknowledge the financial support I received from the department of Mechanical and Materials Engineering at Western University and the Natural Sciences and Engineering Research Council (NSERC). I would like to thank the industry partner VIP metering, eXact systems for their funding and support.

Last but not the least; I owe thanks to my mother without her mental support and constant encouragement, it would not have been possible for me to finish this work.

Table of Contents

List of Tables

List of Figures

List of Appendices

List of Abbreviations, Symbols, Nomenclature

Latin Symbols

A	Pipe area (m^2)
c	Speed of sound inside the fluid (m/s)
$c_{incident}$	Speed of sound in the incident medium (m/s)
$c_{transmitted}$	Speed of sound in the transmitted medium (m/s)
c_{wedge}	speed of sound in the wedge (m/s)
C_{μ}	Turbulence model constant (for $SST\ k-\omega$ model)
d, d_3	Pipe inner diameter (m)
d_1	Vertical distance travelled by the wave in the wedge (m)
d_2	Pipe thickness (m)
d	Coupling property (m/V or C/N)
d^T	Piezoelectric charge constant (m/V)
D	Electric displacement field (C/m^2)
E	Electric field (V/m)
f_o	Frequency of the ultrasonic pulse (Hz)
$f_{clamp-on}$	Flowrate measured by the clamp-on ultrasonic flowmeter (m^3/hr)
F_1	Blending function for the $SST\ k-\omega$ model
k	Turbulent kinetic energy (m^2/s^2)
K	Flow profile correction factor

L	Length of the acoustic path inside the fluid (m)
m	Slope of a straight line
p	Pressure (Pa)
p	Acoustic pressure perturbation (Pa)
p_t	Total pressure (Pa)
p_0	Mean flow pressure (Pa)
p_1	Variation in pressure (Pa)
P_k	Production term
Q	Volume flowrate (m^3/s)
Q_m, f_p	Monopole domain source
q_d, f_v	Dipole domain source
r	Radius of curvature of the centreline of the elbow (m)
R	Radius of the pipe (m)
Re	Reynolds number
S	Strain rate
s_E	Material Compliance (m^2/N)
S_{ij}	Mean rate-of-strain rate tensor
T	Shear Stress (N/m^2)
T_o	Time period of the ultrasonic pulse (s)
t	Flow time (s)

t_1	Time taken by the ultrasonic wave inside the fluid to propagate in the direction of the fluid flow (s)
t_2	Time taken by the ultrasonic wave inside the fluid to propagate in the opposite direction of the fluid flow (s)
t_{wedge}	Time taken by the ultrasonic wave inside the wedge (s)
t_{wall}	Time taken by the ultrasonic wave inside the pipe wall (s)
t_{delay}	Time taken by the ultrasonic wave inside the pipe wall and the wedge (s)
t_{down}	Total time taken by the ultrasonic wave to propagate inside the wedge, pipe wall and fluid in the opposite direction of the fluid flow (s)
t_{up}	Total time taken by the ultrasonic wave to propagate inside the wedge, pipe wall and fluid in the direction of the fluid flow (s)
u	Streamwise axial velocity (m/s)
u	Acoustic velocity perturbation (m/s)
U	Bulk velocity (m/s)
u'	Velocity fluctuations in the axial direction (m/s)
$\overline{u'}, \overline{v'}, \overline{w'}$	Root-mean square velocity fluctuations in x, y and z direction (m/s)
$\overline{u'u'}$	Reynolds normal stress components (m^2/s^2)
$\overline{u'v'}$	Reynolds shear stress component (m^2/s^2)
$\overline{U}$	Mean velocity (m/s)
U_{max}	Maximum velocity of the fluid along the centre of the pipe (m/s)

V	Velocity estimated by the ultrasonic signals integrated along the acoustic path (m/s)
V_a, V_{bulk}	Velocity of the fluid integrated over the pipe cross-section (m/s)
V_{4-20mA}	Voltage in the 4-20mA loop (V)
x	Distance downstream of the elbow (m)
x_1, x_2, x_3	Horizontal distances travelled by the ultrasonic wave in the wedge, pipe wall and fluid (m)
Z	Specific acoustic Impedance (rayl)

Greek symbols

Δt	Time difference between the two ultrasonic signals (s)
ΔP	Pressure differential (Pa)
ε^T	Piezoelectric charge constant (F/m or C/Vm)
λ	Wavelength of the acoustic signal (m)
μ	Dynamic viscosity (N-s/m^2)
μ_t	Turbulent viscosity (m^2/s^{-1})
ρ	Density (kg/m^3)
ρ_0	Mean flow density
σ_{ij}	Stress tensor due to molecular viscosity (N/m^2)
σ_k	Turbulent Prandtl number of turbulent kinetic energy

σ_ω	Turbulent Prandtl number of turbulent specific dissipation rate
Ω_{ij}	Mean rotation rate tensor
Ω	Unit of resistance Ohm
ω	Specific dissipation rate of turbulent kinetic energy (s^{-1})
τ_{ij}	Sub-grid scale stresses
$\emptyset$	Orientation angle for mounting clamp-on ultrasonic flowmeter around the pipe (deg)
θ	Elbow's rotation angle (deg)
θ_c	Critical angle
$\theta_1, \theta_2, \theta_3$	Angle of the ultrasonic wave in the wedge, pipe wall and fluid
$\theta_{incident}$	Angle of incidence
$\theta_{transmitted}$	Angle of the ultrasonic wave in the transmitted medium
$\sigma_{\omega1}, \sigma_{\omega2}, \sigma_{k1}, \sigma_{k2}$	$SST\ k-\omega$ model constants
$\beta_1, \beta_2, \gamma_1, \gamma_2, {\beta_o}^*$	$SST\ k-\omega$ model constants
$\alpha, \beta_o, \sigma_\omega, \sigma_d, \sigma_k$	$k-\omega$ model constants

Abbreviations

DG	Discontinuous Galerkin
DAQ	Data Acquisition device
FEM	Finite element method

UFM	Ultrasonic flowmeter
CFD	Computational Fluid Dynamics
LES	Large Eddy Simulation
RANS	Reynolds Averaged Navier Stokes
SST	Shear stress transport
TKE	Turbulent kinetic energy

1 Introduction

This thesis discusses the performance of a clamp on ultrasonic liquid flowmeter installed in non-ideal locations. The literature review is presented in this chapter.

1.1 Background

Ultrasonic flowmeters (UFM) were first introduced in 1959 for blood flow analysis by Satomura (1959). Later in 1963, Miaki et al. (1967) introduced an ultrasonic flowmeter for industrial use. These flowmeters used to work on the "Doppler shift frequency" principle. This measurement principle required seeding of the fluid with particles. The principle of "Time-of-flight" to measure liquid flowrate was introduced by Matikainen et al. (1986) and a flowmeter was developed in 1990s. This principle does not require particles in the fluid and hence, flowmeters working on this principle had an advantage over the earlier ones in terms of accuracy and applications. According to Sanderson & Yeung (2002), the uncertainty in the measurement of a Doppler shift ultrasonic flowmeter is greater than 10% and for time-of-flight ultrasonic flowmeter can be 1% - 3% according to Baker (2000).

There are two types of Ultrasonic flowmeters working on the time-of-flight principle: In-line and Clamp-on. In-line ultrasonic flowmeters have "reflectors" installed inside the pipe which are in contact with the moving fluid as shown in figure 1.1. Due to this reason, they are called In-line, Wetted or Intrusive ultrasonic flowmeters. In-line ultrasonic flowmeters have an uncertainty close to $\pm 1\%$ (Baker, 2000).

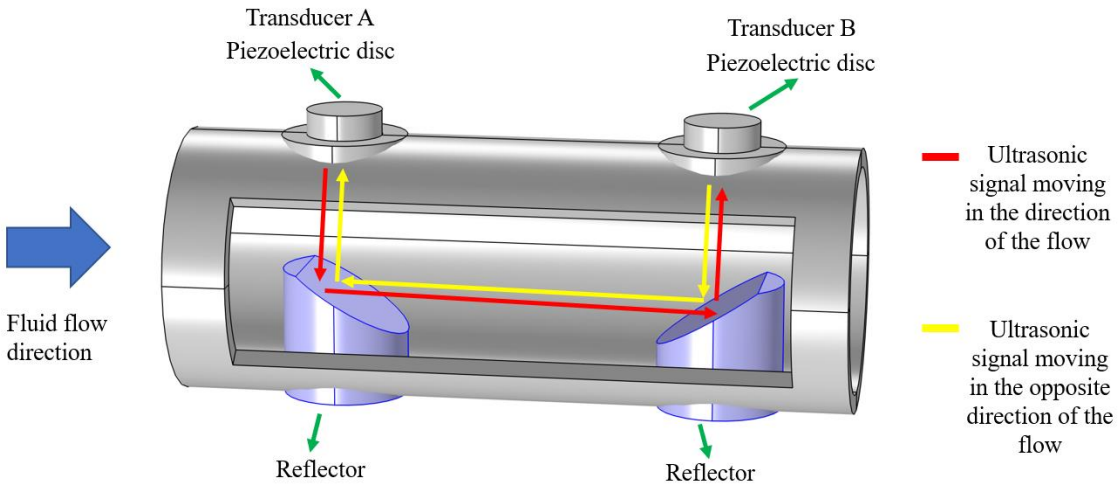

Figure 1.1 In-line ultrasonic flowmeter

On the other hand, Clamp-on ultrasonic flowmeters are installed on the outer side of the pipe as shown in figure 1.2 which is why they are called Clamp-on or Non-intrusive flowmeters. They have an uncertainty ranging from 1% - 3% (Baker, 2000). The benefits of clamp-on ultrasonic flowmeter include no contact with the fluid, no moving parts, easy and low-cost installation/maintenance.

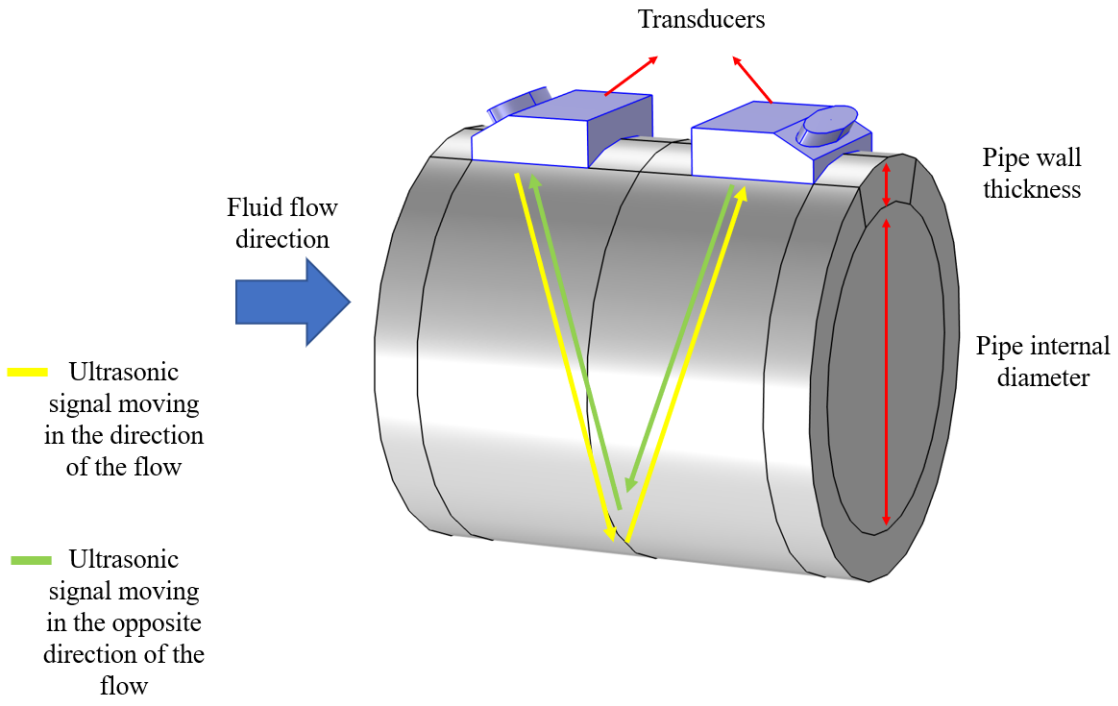

Figure 1.2 Clamp-on ultrasonic flowmeter

The uncertainty of a clamp-on ultrasonic flowmeter measurement depends on various factors which include the internal pipe condition (fouling, corrosion), fluid contamination and fluid flow profile distortion caused by varying upstream pipe conditions. Flow profile distortions are caused by bends, expansions, contractions, valves or pumps upstream/downstream of the flowmeter installation location. The dimensions of the pipe thickness (t) and diameter (d) are used to compute the distance between the transducers for installation. The pipe material should be homogenous because the speed of sound of the ultrasonic wave depends on the medium through which it is propagating (Gu & Cegla, 2019). Similarly, layers of different materials on the pipe surfaces cause scattering and resistance to ultrasonic wave propagation (Gu & Cegla, 2019). In practical applications where a clamp on ultrasonic flowmeter is to be installed the outer surface of the pipe should be cleaned of unwanted layers of material, like paint/grease/dirt (Sanderson & Yeung, 2002). However, internal fouling or upstream/downstream disturbances in the pipe network cannot be altered. Locating an ideal installation location with no fluid flow disturbance and a polished new pipe section is not always possible. 90^0 elbows are an integral and common part of every pipe network. Investigating the uncertainty of a clamp-on ultrasonic

flowmeter installed after a 90^0 elbow will allow the installation of this flowmeter in such a location. The literature review of a fluid flow in a pipe with a 90^0 elbow and flowmeters is discussed further in this chapter.

1.2 Literature review

Fluid flow measurement is required in many practical applications. In this section fluid flow within and downstream of a 90^0 elbow will be discussed. A detailed discussion of types of flowmeters including ultrasonic flowmeters, their working principles and uncertainty in their measurements is included in the review.

1.2.1 Fluid flow in a pipe and elbow section

Turbulence in fluid flow is generated at higher Reynolds number or if it encounters flow disturbances in the pipe network. There are various engineering applications where turbulent flow inside a pipe is not desirable. One of them is piping in nuclear reactors where turbulent flow causes flow accelerated corrosion which causes material failure leading to tragic accidents (Jung & Seong, 2005). This section discusses the turbulent flow within and downstream of a 90^0 elbow. The elbow and pipe sections can be grouped by defining a ratio between elbow and the pipe which is as follows.

$$r/d = \frac{radius\ of\ curvature\ of\ the\ centre-line\ of\ the\ elbow}{pipe\ inner\ diameter} \tag{1.1}$$

The figure 1.3 shows the schematic of an elbow and pipe section where, $\theta = 0^0$ depicts the start of the elbow and $\theta = 90^0$ depicts the exit of the elbow. The measurement locations inside the elbow are defined by the angle θ. The measurement locations downstream of the elbow are defined as multiples of diameter of the pipe (x/d) in table 1.1.

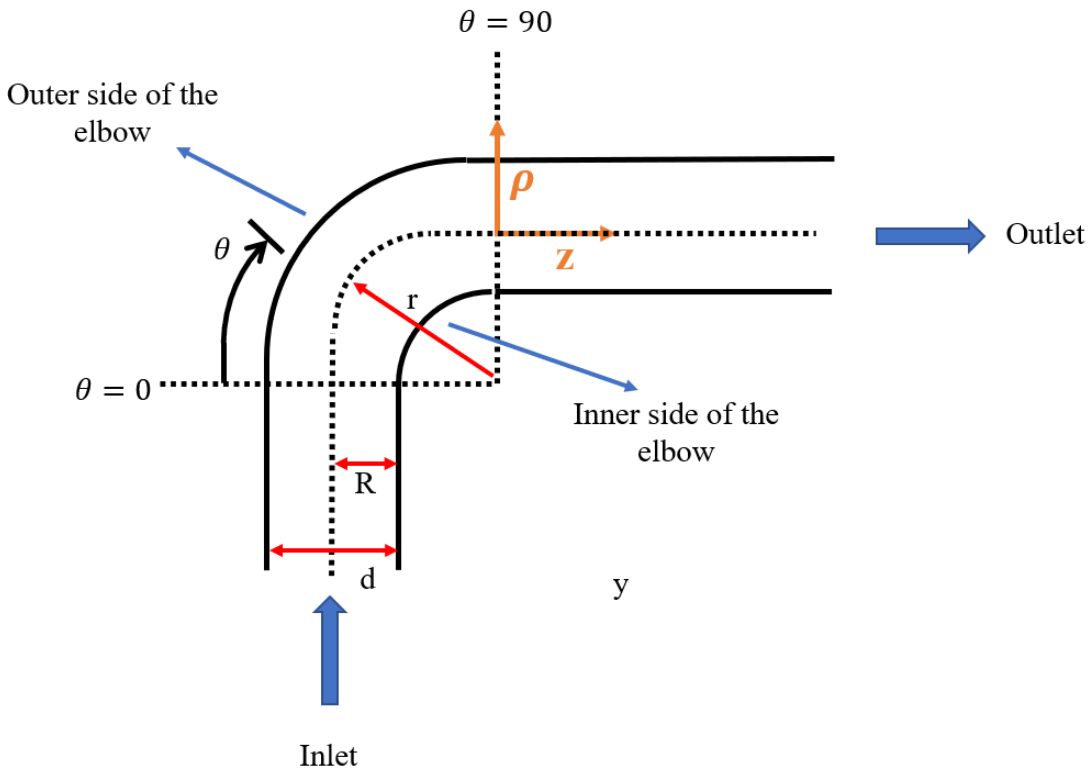

Figure 1.3 Schematic of an elbow and pipe section with cylindrical coordinates

1.2.1.1 Flow within an elbow

The figures presented in this section are plotted by extracting information from different papers to compare and analyze the data in order to understand the flow structure within and downstream of the 90^0 elbow. Table 1.1 summarizes the literature concerning fluid flow within a 90^0 elbow and pipe section for various r/d and Reynolds numbers.

Table 1.1 Summary of literature on fluid flow in elbow-pipe sections arranged in the ascending order of r/d

Authors	r/d	Reynolds number (Re)	Measurement Locations within elbow ($\boldsymbol{\theta}$)	Measurement location downstream of elbow (x/d)	Study methodology
(Wang et al., 2015)	0.82	$0.5, 1\ and\ 2 \times 10^4$	0^0, 30^0, 45^0, 60^0, 90^0	1, 2	Numerical
(Dutta et al., 2016)	1	$1\ to\ 10 \times 10^5$	90^0	-	Numerical
(Rutten et al., 2001)	1	$0.5\ and\ 1 \times 10^4$	-	1	Numerical
(Ikarashi et al., 2018)	1, 1.2, 1.5	$3, 5\ and\ 10 \times 10^4$	0^0, 22.5^0, 45^0, 67.5^0, 90^0	0.5, 1	Experimental
(Ono et al., 2011)	1, 1.5	$1.8\ and\ 5.4 \times 10^5$	90^0	0.53	Experimental
(Tanaka & Ohshima, 2012)	1, 2	$500 - 1.47 \times 10^7$	-	0.5, 1	Numerical
(Tan et al., 2014)	1, 2	6×10^4	0^0, 30^0, 60^0, 90^0	1, 2, 3, 7	Numerical
(Taguchi et al., 2018)	1.5	$5, 10\ and\ 20 \times 10^4$	0^0, 22.5^0, 45^0, 67.5^0, 90^0	-	Experimental
(Röhrig et al., 2015)	1.58	$2.4\ and\ 3.4 \times 10^4$	0^0, 22.5^0, 45^0, 67.5^0, 90^0	0.67	Numerical

(Sudo et al., 1998)	2	6×10^4	0^0, 30^0, 60^0, 90^0	1, 2, 5, 10	Experimental
(Enayet et al., 1982)	2.8	$500, 1093, (4.3 \times 10^4)$	0^0, 30^0, 60^0	1	Experimental
(Kim et al., 2014)	3	$5, 10\ and\ 20 \times 10^4$	-	3.5, 10, 50	Experimental

The normalized streamwise velocity profiles at different values of θ are presented in the figures 1.4 and 1.5. The colours and the markers in these figures depict the r/d and the authors respectively.

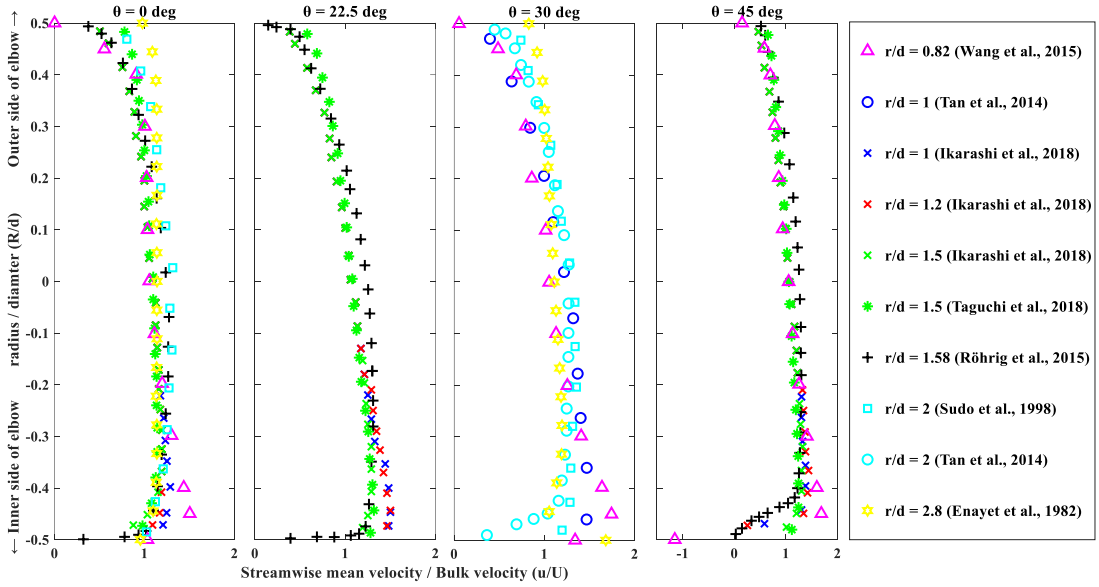

Figure 1.4 Normalized streamwise velocity profile in first half of the elbow

In figure 1.4, at $\theta = 0^0$ (which depicts the inlet of the elbow) most of the velocity profiles are typical of a turbulent profile inside a straight pipe. The profile from Wang et al. (2015) (magenta colour) is different from the others profiles which indicates an upstream disturbance in their setup. At $\theta = 22.5^0$ the streamwise velocity near the inner side of the

elbow increases for lower r/d=(1 blue and 1.2 red), Ikarashi et al. (2018). This phenomenon of increase in axial velocity near the inner side of elbow as compared to the outer side creates a pressure gradient which is responsible for the generation of secondary flow known as Dean vortices, Ikarashi et al., (2018). At $\theta = 22.5^0$, for r/d=1.5 (green, Ikarashi et al. (2018) and Taguchi et al. (2018)) and r/d=1.58 (black, Röhrig et al. (2015)) depict an identical trend which is expected as r/d=1.5 and 1.58 are close to each other. This is expected as the lower the r/d the sharper is the bend and the higher the intensity of the secondary flow. At $\theta = 30^0$, the r/d=1 (blue curve) and r/d=0.8 (magenta curve) show a greater increase in axial velocity when compared to the r/d=2 (cyan curve) or r/d=2.8 (yellow curve) plot at the inner side of the elbow. At $\theta = 30^0$, there is an anomaly in the data presented by Enayet et al. (1982) (yellow curve) at the inner side of the elbow. At $\theta = 45^0$ location, the data presented by Wang et al. (2015) (magenta curve) goes beyond zero close to the inner side of the elbow. This indicates a flow separation at this location. For other r/d the flow has not separated at this location.

This comparison shows that for r/d = 1.5, 1.58, 2 and 2.8, a lower velocity/pressure gradient (hence, a weaker secondary flow) is generated when compared to r/d = 0.82, 1 and 1.2. Due to this higher gradient the flow separates early in the elbow for r/d=0.82.

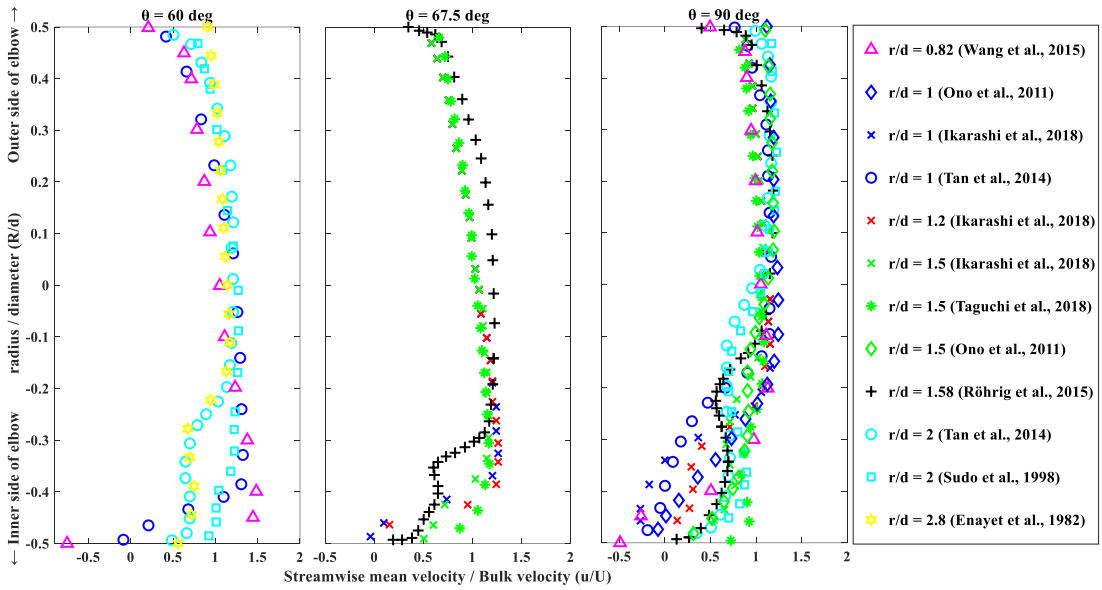

Figure 1.5 Normalized streamwise velocity profiles in second half of the elbow

At $\theta = 60^0$ *and* 67.5^0, for lower r/d = 0.82 and 1 (magenta and blue curves) the axial velocity near the inner side of the elbow goes negative which depicts a flow separation. However, for r/d > 1 the flow is not separated but a low velocity region has extended towards the centre of curvature of the elbow to a quarter of the elbow diameter. For $\theta = 90^0$, for r/d = 0.82 (magenta, Wang et al. (2015)) and blue curves) and r/d=1 (blue, Ikarashi et al. (2018), Tan et al. (2014) and Ono et al. (2011)) depict a trend of a reverse flow near the inner side of the elbow. For r/d = 1.5 and 1.58 (green and black curves) the flow is not reversed but the low velocity region extends towards the centre of curvature of the elbow. For a greater r/d ratio=2 (cyan curves) the low velocity region extends further towards the centre of curvature of the elbow to almost half of the diameter of the elbow.

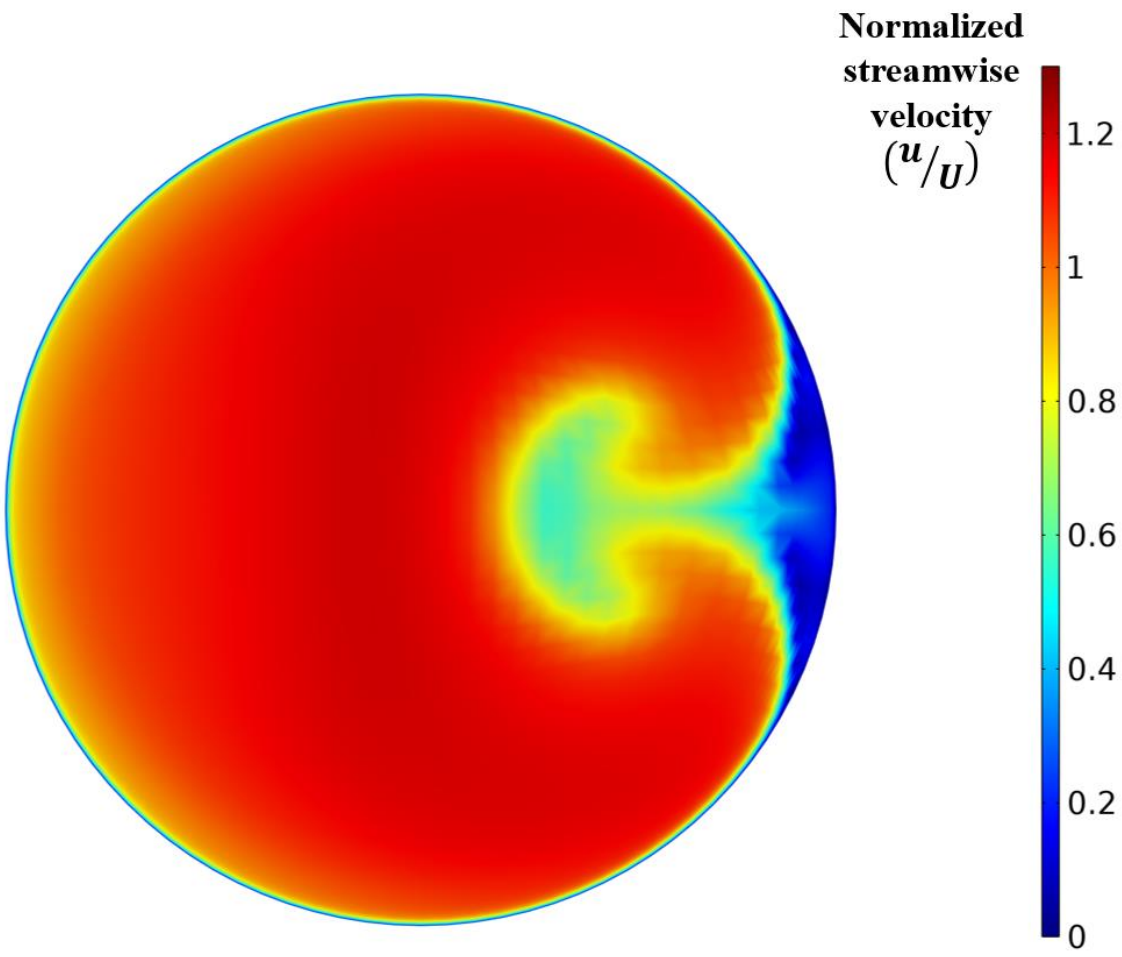

Figure 1.6 Normalized streamwise velocity contour depicting dean vortices at the elbow outlet computed in the numerical study conducted in this thesis

The phenomenon of secondary flow 'Dean vortices' in a fluid flow passing through a 90^0 elbow is shown in figure 1.6. It depicts a cross-sectional view at the elbow outlet where colors represent the streamwise velocity (normal to the elbow outlet cross-section). The right hand side of the figure depicts the inner side of the elbow whereas left hand side of the figure shows the outer side of the elbow. The low velocity region is shown in blue at the inner side of the elbow. Fluid above and below the centre line curls around the low velocity region due to the velocity gradient hence generating Dean vortices.

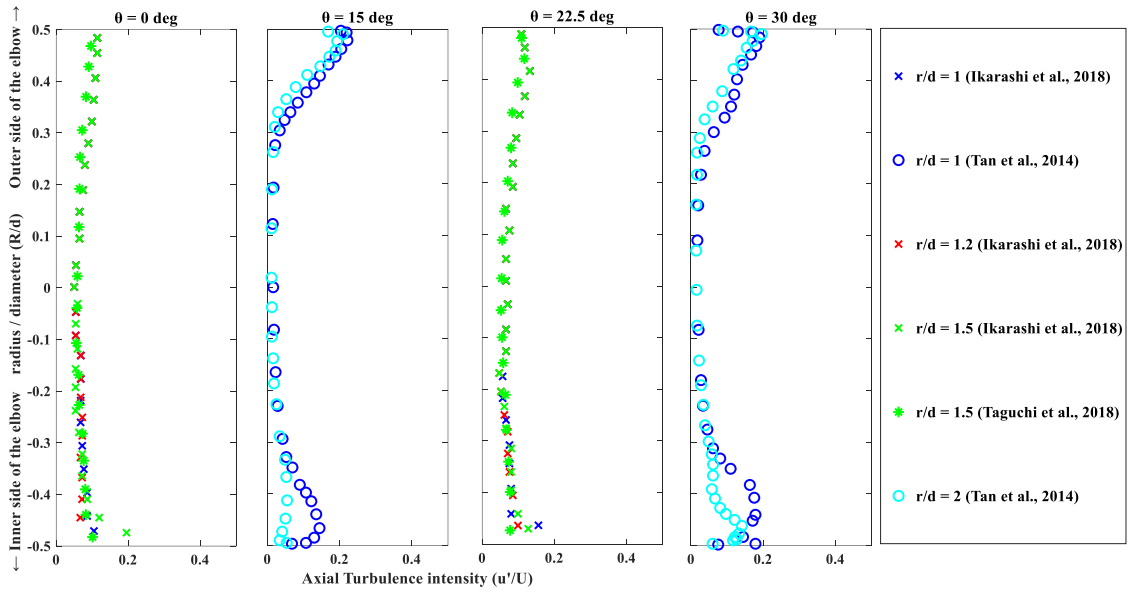

Figure 1.7 Axial turbulence intensity in the first half of the elbow

The turbulence intensity profiles within the elbow are presented in the figures 1.7 and 1.8. Ikarashi et al. (2018) and Taguchi et al. (2018) presented experimental results which show a slight rise in turbulence intensity near the walls. Tan et al. (2014) presented numerical results which show the rise in turbulence intensity on the outer and inner side of the elbow which is expected due to the turbulence being generated by the walls. Turbulence is generated near the walls because of the mean shear between the fluid layers as the velocity of the fluid is zero at the boundary of the wall.

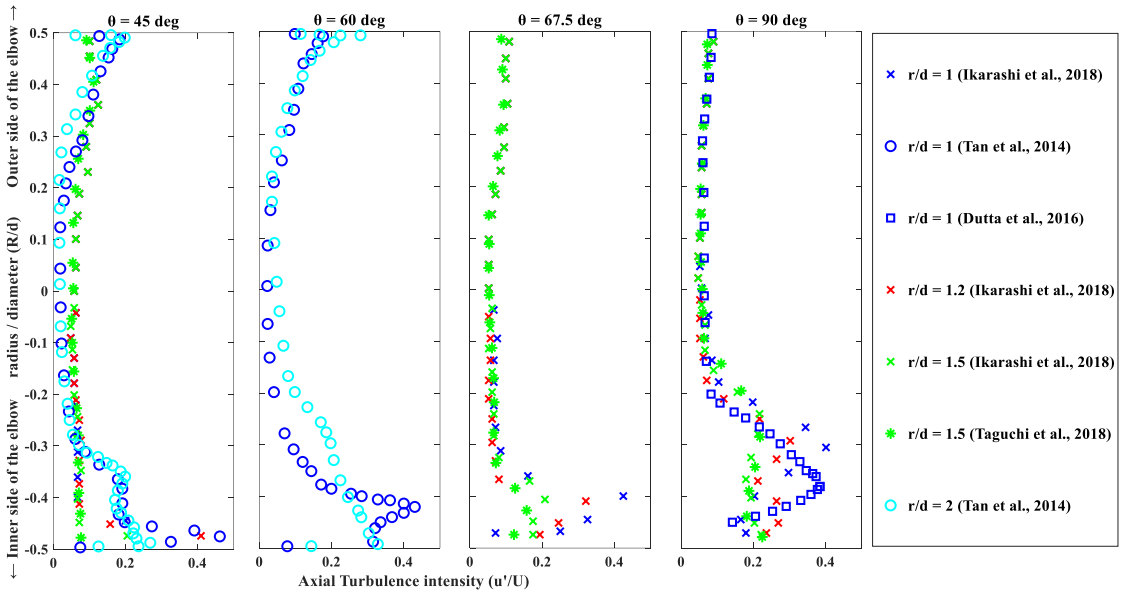

Figure 1.8 Axial turbulent intensity in the second half of the elbow

At all θ, the magnitude of the turbulence intensity close to the inner side of the elbow is higher compared to at the outer side of the elbow. For r/d = 1 and 1.2 (blue and red curves) the magnitude is higher when compared to r/d = 1.5 and 2 (green and cyan curves). As θ increases from 45^0 to 90^0, the location of the peak of the turbulence intensity moves towards the centre of the elbow. This is in accordance with the trend observed in the velocity profiles.

1.2.1.2 Flow downstream of the elbow

The secondary flow developed due to a 90^0 elbow propagates downstream of the elbow. Study of the flow structure downstream of a pipe elbow, helps to determine where the effect of the secondary flow diminishes.

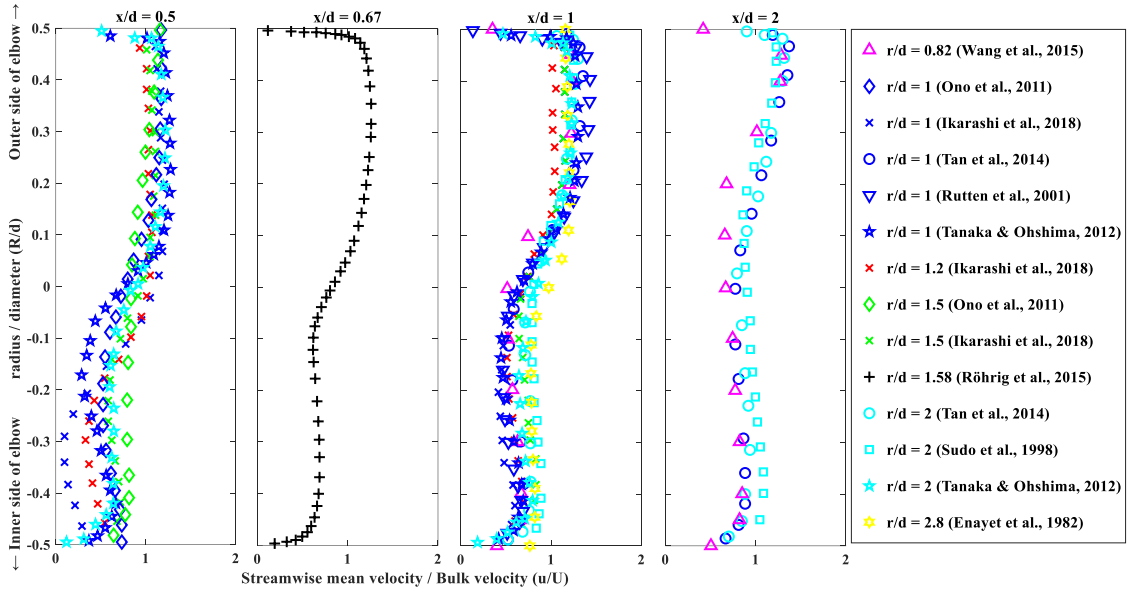

Figure 1.9 Normalized streamwise velocity profiles across the pipe section close to the elbow outlet

The normalized mean flow velocity profiles are presented in figure 1.9 at the locations downstream of the elbow outlet. At x/d=0.5, there is no reverse flow and the low velocity region which originated from the inner side of the elbow extend upwards to almost half of the elbow's diameter. For a lower r/d = 1, 1.2 (blue and red curves) the magnitude of the low velocity is greater when compared to higher r/d = 1.5 and 2 (green and cyan curve). This is consistent with the trend seen in the flow profiles inside the elbow where for a lower r/d the secondary flow is stronger. This secondary flow will take more distance downstream of the elbow to diminish. At x/d=1, the magnitude of the low velocity for r/d = 0.82 1 and 1.2 (magenta, blue and red curves) is greater than for r/d = 1.5, 2 and 2.8 (green, cyan and yellow curves). At x/d=2, the low velocity region starts to diminish for a higher r/d=2 (cyan curve) compared to r/d = 0.82 and 1 (magenta and blue curves).

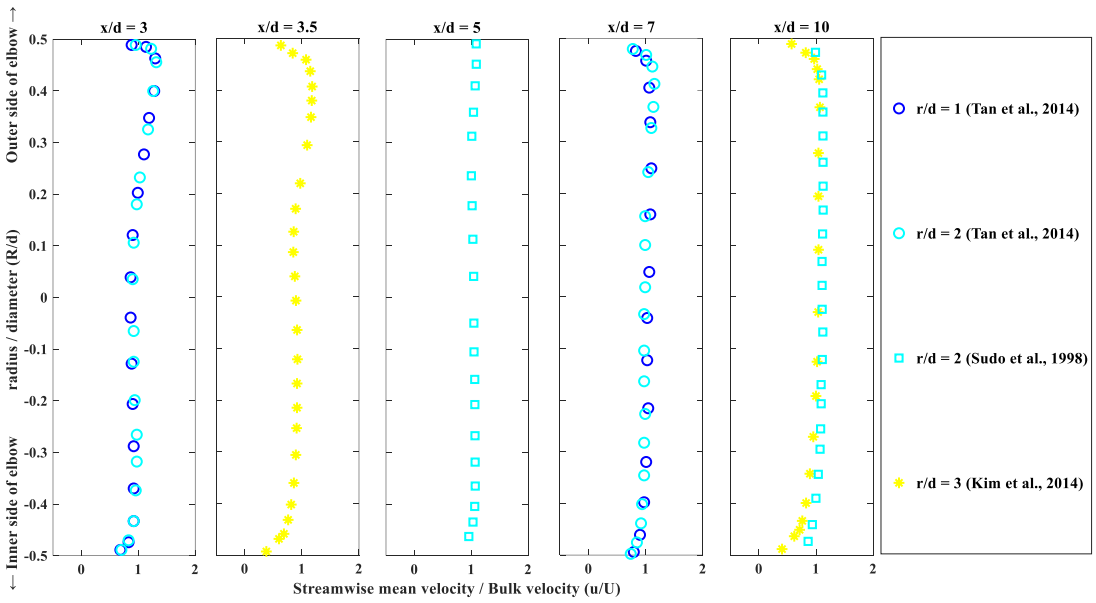

Figure 1.10 Normalized streamwise velocity profiles across the pipe section further downstream of an elbow

The flow profiles are plotted at further downstream locations in the figure 1.10. At x/d = 3 and 3.5, there is a slight low velocity region around the centre of the pipe. The effects of the secondary flow on the flow profile at these locations are small. Further downstream, at x/d = 5, 7, 10 and 50, the flow profile takes on the shape of a turbulent pipe flow. So, beyond x/d=3.5 the effects of the secondary flow generated due to a 90^0 elbow diminishes. At x/d=10, the velocity profile has recovered from the effects of the secondary flow.

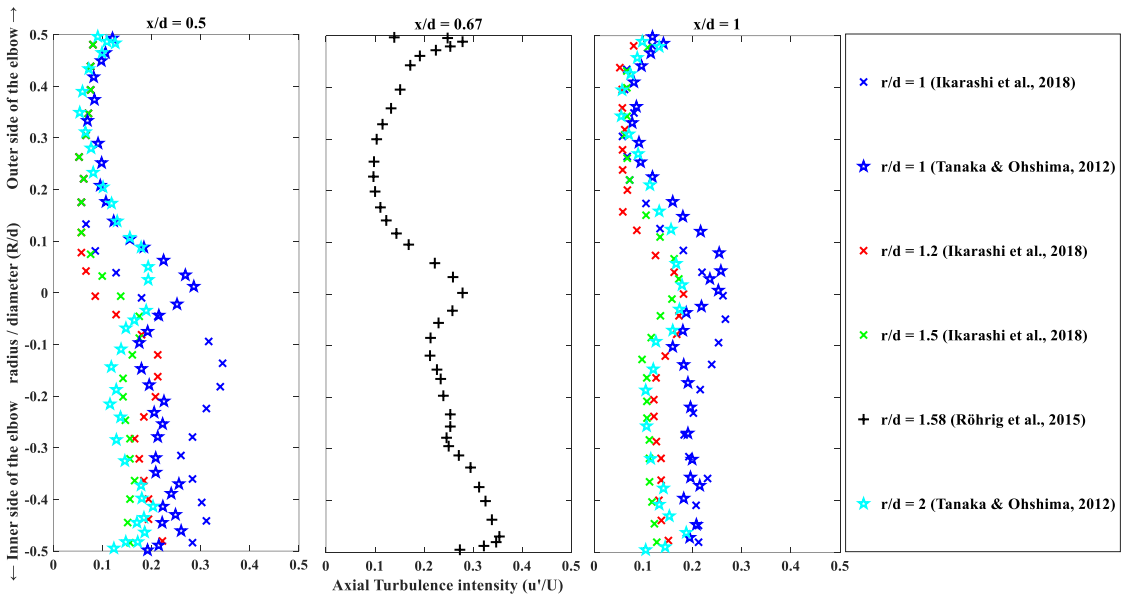

Figure 1.11 Axial turbulence intensity across the pipe section downstream of the elbow

At x/d = 5 and 1, for the r/d = 1 and 1.2 (blue and red curves) the magnitude of the axial turbulence intensity is greater than the r/d = 1.5 and 2 (green and cyan curves). The peak of the turbulence intensity has moved towards the centre of the pipe which is consistent with axial profiles shown in figure 1.9.

The conclusions from this comparative study of fluid flow within a 90^0 elbow and downstream of the elbow are as follows.

- For r/d <= 1, flow separation and adverse velocity gradients are present in the second half (on the inner side) of the elbow due to stronger Dean vortices.
- For r/d > 1, the secondary flow is weak when compared to r/d <= 1. The lower velocity region occurs due to the secondary flow.
- The low velocity region for r/d > 1 extend towards the centre of the elbow as the r/d increases.

- The effects of the secondary flow are dominant until x/d = 3 but they diminish beyond x/d = 5.

Having review the flow regime through and downstream of a 90^0 elbow, the next section discusses the details and types of different flowmeters that may be installed downstream of such an elbow.

1.2.2 Types of flowmeters

Flowmeters are used in our houses to measure water and gas for billing purposes (Terés-Zubiaga et al., 2018). They are also used to measure oil, chemical, coolants and gas flowing in an industrial plant (Sifferman et al., 1989). Their precise measurement is critical for the process and is directly related to the expenses of the company. The choice of flowmeter depends on the application and operating conditions. They are categorized based on measuring principle and their application as mechanical, differential pressure-based, electromagnetic, ultrasonic and Coriolis flowmeters. They are briefly discussed below.

1.2.2.1 Mechanical flowmeters

The mechanical flowmeters have moving parts which are in contact with the flowing fluid. These meters are also called positive displacement meters (Baker & Morris, 1985). These mechanical meters are of various types which include gear meter, turbine meter, single-jet meter and multi-jet meter. Gear meters have small gears which rotate due to fluid flow. They have 2 chambers (as shown in figure 1.12) and a fixed volume of fluid coming from the inlet is stored in one chamber which exerts force on the gears to turn (Li et al., 2009).

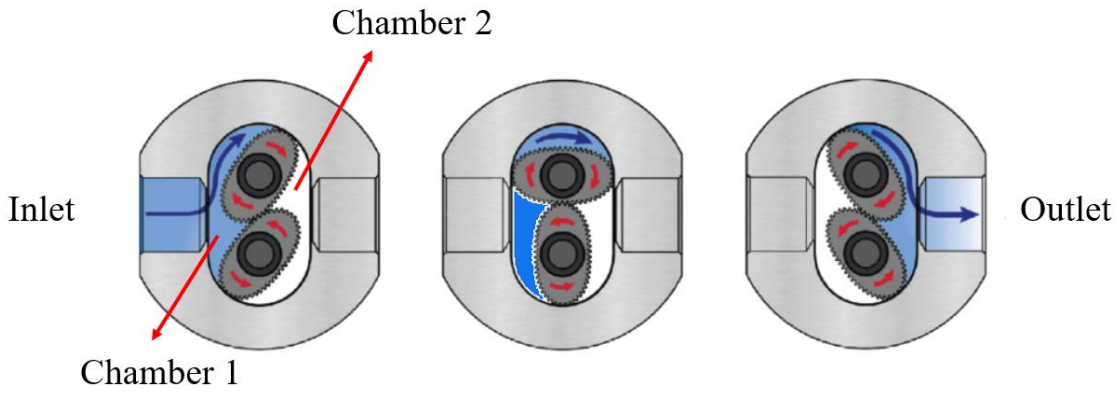

Figure 1.12 Schematic of Oval gear flowmeter adapted from Marx, (2019)

As the gears turn the fluid enters the second chamber. The gears have permanent magnets which are connected to a current transducer which sends an electrical signal for flow measurement. The flowrate range depends upon the design and size of the specific flowmeter. Details of these meters are tabulated in Table 2.

Table 1.2 Details of mechanical meters (Baker, 2000)

Parameters	**Gear meters**	**Turbine meters**
Uncertainty	0.1%-0.3%	0.1%-0.5%
Flowrate range (m^3/hr)	$6 \times 10^{-5} - 60$	$0.03 - 7000$
Advantages	High accuracy Less effected by viscosity Ideal for extremely small flowrates	Greater range of flowrates Can be used briefly at very high flowrates
Disadvantages	Rapidly varying flowrates can cause damage. High initial price and maintenance cost.	Greater pressure drop compared to gear meters.

	Uncertainty increases due to fluid slippage at low and high flowrates May only be used for clean and filtered fluids	Sensitive to flow disturbances, viscosity changes and installation locations. Periodic maintenance needed as deposits on bearings and blades decrease accuracy Less reliable at lower flowrates
Application	Different oils, fuel, wax, paint, dyes	Oil, drinks, dairy, cryogenic fluids

Turbine flowmeters have an axial turbine installed in the path of the moving fluid. The moving fluid exerts force on the turbine blades which rotate with a speed proportional to fluid speed (Xu, 1992). The readings are measured from the analogue meter attached to the flowmeter when a steady state is reached.

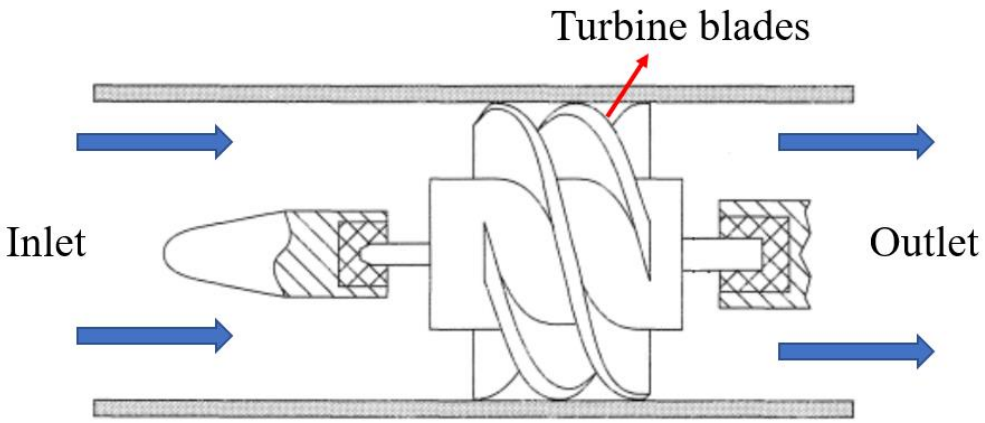

Figure 1.13 Schematic of a turbine flowmeter adapted from (Shekhter, 2011)

These meters are used to measure gas and liquid flowrates (Xu, 1992). Single-jet and multi-jet meters are a development of turbine meters. In a single-jet meter (figure 1.14), a single stream of fluid is focused on the rotating impeller blades (Larraona et al., 2008). However,

in a multi-jet meter (figure 1.15) various streams of fluid are imparted on the impeller through multiple input ports (McDonald, 2014). These streams are directed onto the impeller from different directions which causes an even wear of the impeller blades (Walter et al., 2018).

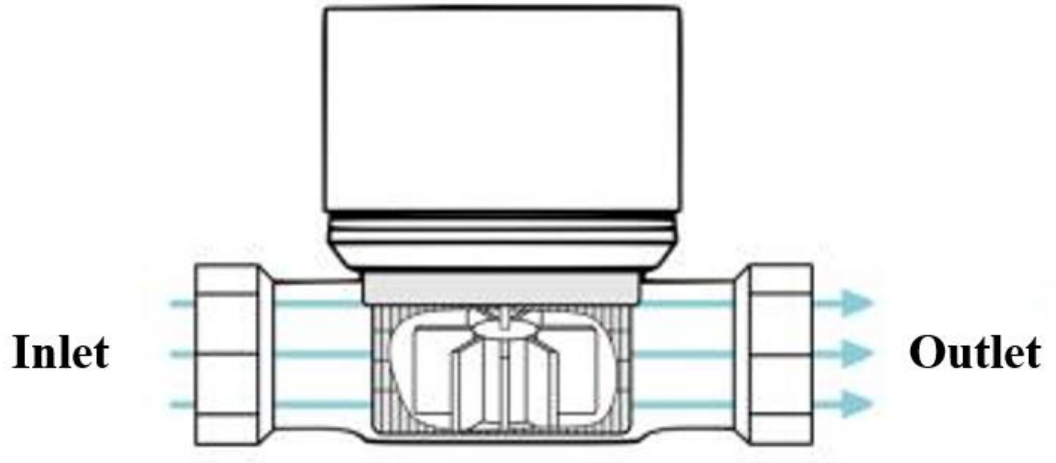

Figure 1.14 Schematic of a single-jet flowmeter (Gaimc, (2018) copyright free)

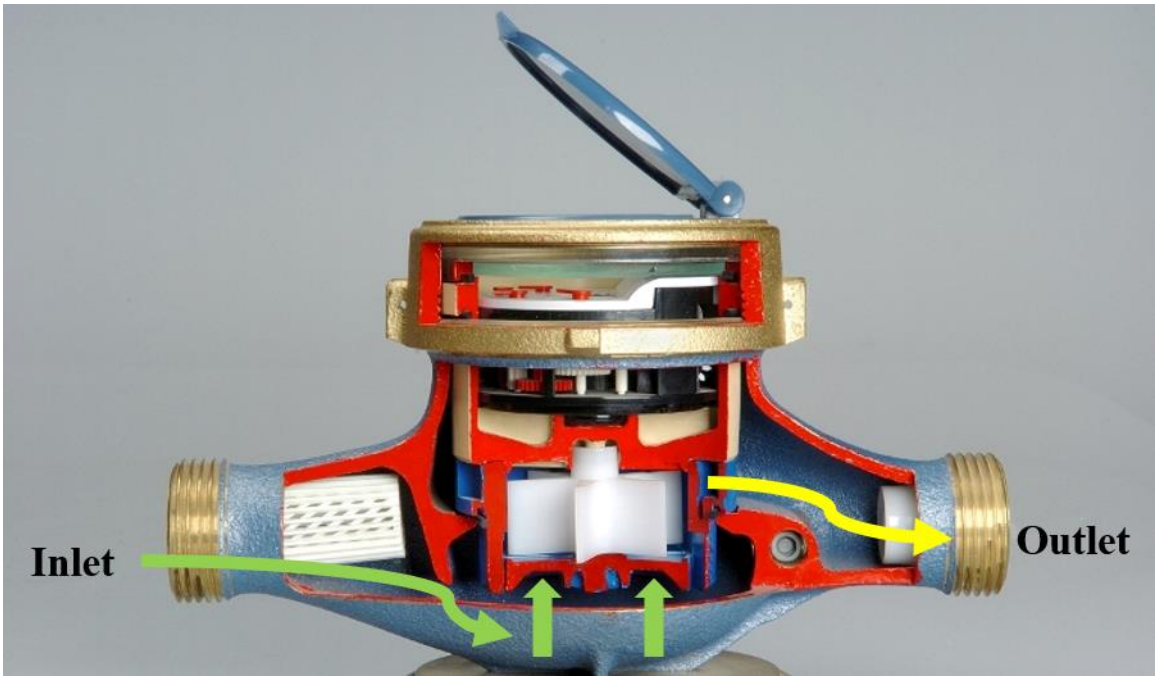

Figure 1.15 Schematic of a multi-jet flowmeter (Yalcin, (2008) copyright free)

1.2.2.2 Differential pressure-based meters

This type of meters includes the Orifice-plate meter and venturi meter. The orifice-plate meter (in figure 1.16) consists of a plate with a hole placed perpendicular to the flow (Morrison et al., 1994). This configuration restricts the flow and causes high energy and pressure losses. There is a differential between static pressures up and downstream of the plate. This change in pressure is used to estimate the flowrate.

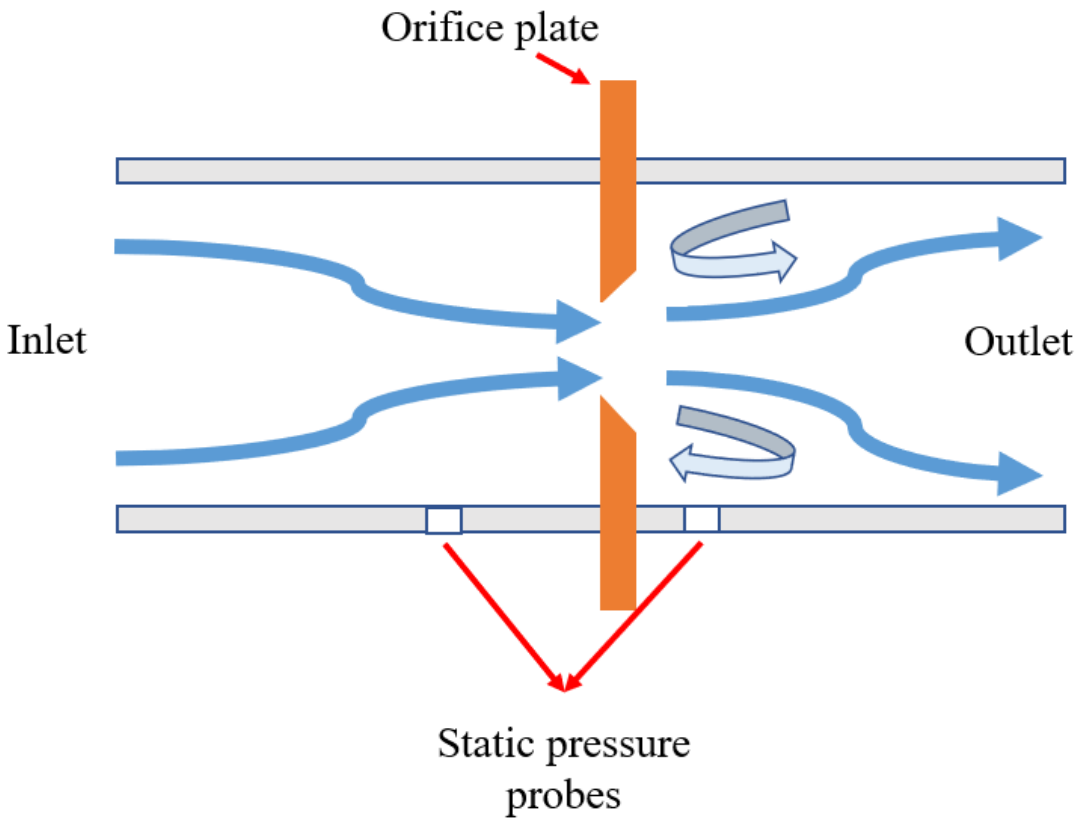

Figure 1.16 Schematic of orifice-plate flowmeter

Further details of these meters are outlined in Table 1.3.

Table 1.3 Details of Pressure based meters (Baker, 2000)

Parameters	Orifice-plate meters	Venturi meters
Uncertainty	2%-2.5%	1%-1.5%
Advantages	No moving parts.	No moving parts.

	Compact design and easy to install on to existing pipe network.	Less affected by upstream flow disturbance compared to other flowmeters Low pressure losses
Disadvantages	Poor pressure recovery and high energy losses Abrasive fluids and deposits cause corrosion and blockage of the hole in the plate. Pulsation in the fluid increases uncertainty. Sensitive to upstream flow disturbances.	Larger device compared to orifice-plate meter.
Application	Gas, steam, water, oil	Water, gases

A venturi flowmeter consists of a straight pipe with different sections of varying diameters usually called the nozzle, throat and diffuser as shown in figure 1.17 Fluid enters the nozzle section with some velocity and pressure. Due to conservation of mass, when fluid reaches the throat its velocity increases, thereby decreasing the pressure. Pressure ports on the inlet and throat measure the difference in pressure from which the flowrate is estimated (Ghassemi & Fasih, 2011).

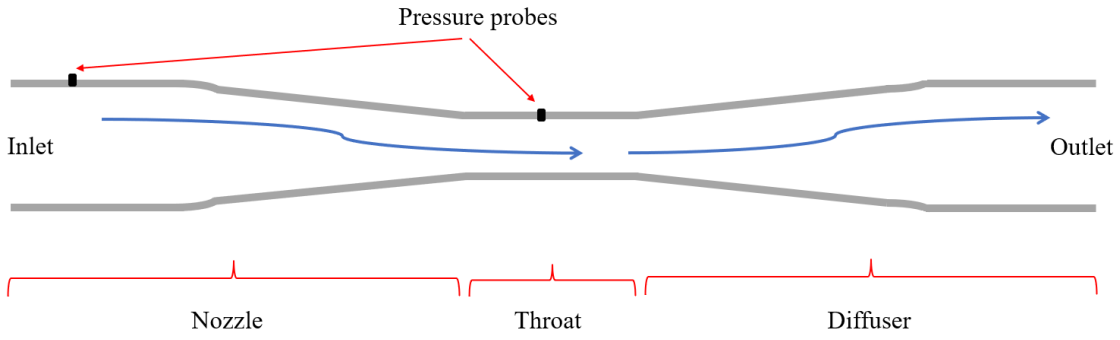

Figure 1.17 Schematic of venturi flowmeter

1.2.2.3 Electromagnetic, Coriolis and Ultrasonic flowmeters

Electromagnetic flowmeters operate on the principle of Faraday's law of electromagnetic induction (Shercliff, 1962). Fluid flows inside a pipe where a coil excited by an alternating current is wrapped around that section as shown in figure 1.18. The coil creates a magnetic field around the pipe. The fluid must be electrically conductive and the pipe should be made up of a non-magnetic material so that the magnetic field created by the coil penetrates the pipe (Baker, 2000).

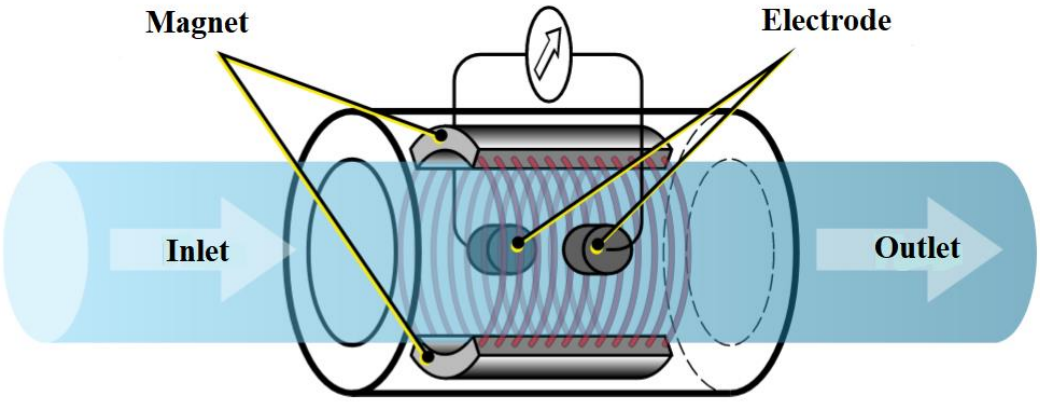

Figure 1.18 Schematic of electromagnetic flowmeter adapted from (O'Neill, 2019)

This coil has two electrodes mounted in the walls of the pipe which are aligned perpendicular to the flow direction as shown in figure 1.18. When the fluid flows in the presence of magnetic field, a potential difference is generated which is sensed by these electrodes (Shercliff, 1962). This potential difference is used to estimate the flow velocity. The table 1.4 draws a comparison between different flowmeters.

Table 1.4 Details of Electromagnetic, Coriolis and Ultrasonic flowmeters (Baker, 2000)

Parameters	Electromagnetic meters	Coriolis meters	Ultrasonic meters
Uncertainty	0.3%-1.5%	0.01%-0.5%	1%-3%

Advantages	Less affected by upstream fluid disturbances when compared to other meters.	Very accurate No bearings or probes	No moving parts No plumbing (clamp-on) which reduces installation cost and time. Low operating cost
Disadvantages	Requires an electrically conducting liquid Frequent maintenance and cleaning of electrodes. Sensitive to pulsating flow and air pockets. Pipe should be of non-magnetic material.	External vibrations close to the operating frequency of the meter causes uncertainty. High initial and operating cost Corrosion fatigue can cause material failure over time.	Sensitive to flow disturbances which increases uncertainty. Fouling or corrosion inside the pipe causes uncertainty.
Application	Conducting liquid	Liquids, gases	Liquids, gases

A Coriolis flowmeter works on the principle of the Coriolis effect. It is also known as a mass flowmeter as it measures mass flowrate of the fluid moving inside the pipe (O'Banion, 2013). In a U-tube Coriolis flowmeter shown in figure 1.19, the fluid flows through the tube which is attached to an actuator that induces vibrations (Sultan & Hemp, 1989). With no fluid flow the vibration of both halves of U-tube is symmetrical or in phase. With a fluid flow, the inlet half-side of the tube lags behind the induced vibration. However, the outlet half side of the tube leads the induced vibration (Sultan & Hemp, 1989). This vibratory motion on both sides of the tube is sensed by two sensors (optical, capacitive or inductive) on each side. The Coriolis force will cause both halves of U-Tube to vibrate out

of synchronization (O'Banion, 2013). The amount of phase shift between the two vibrations is used to estimate the mass of fluid flowing through the tube.

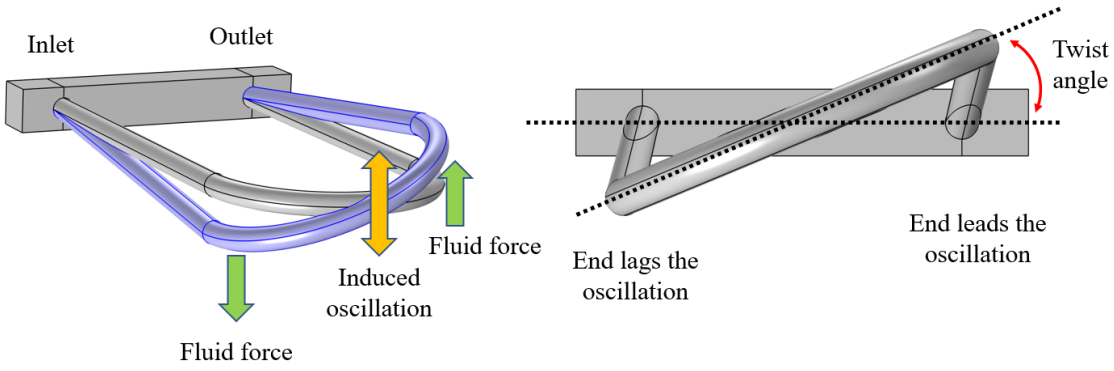

Figure 1.19 Depiction of a U-shaped Coriolis flowmeter

Ultrasonic flowmeter uses ultrasonic signals to estimate the flow velocity and consequently flowrate inside a pipe which is discussed in section 1.2.4.3. These meters are divided into various types depending upon the measuring principle and construction. Ultrasonic flowmeter is discussed further in this chapter.

1.2.3 Ultrasonic flowmeters

The concept of ultrasonic flowmeters for liquids was first presented by (Kritz, 1955). After some years, Herrick & Anderson (1959) proposed the application of these flowmeters for medical purposes like blood flow measurements. Sanderson (1982) highlighted the problems encountered using traditional flowmeters and proposed electromagnetic/ultrasonic flowmeters which are not in contact with the fluid. The performance of ultrasonic flowmeters with 2 pairs of transducers emitting two ultrasonic signals was experimentally studied by Thompson (1978). Lynnworth (1981) discussed various types of ultrasonic flowmeters, their measurement processes and transducer mounting mechanisms. It was not until the early 2000s that ultrasonic flowmeters were installed in industrial setups. According to Choi et al. (2011), in 2006 the ultrasonic flowmeters had a market share of 31% in northern Europe.

1.2.3.1 Types of Ultrasonic flowmeters

Ultrasonic flowmeters are categorized into two types.

- In-line/ wetted/ intrusive
- Clamp-on/ non-intrusive

In-line ultrasonic flowmeters have reflectors inside the pipe where fluid is in contact with the reflectors as shown in figure 1.1. The two transducers (A and B in figure 1.1) mounted on top of the pipe send and receive ultrasonic signals.

On the other hand, clamp-on ultrasonic flowmeters are not in contact with the fluid as shown in figure 1.2. They are clamped on the outer side of an existing pipe network without disturbing the fluid flow, which can be critical in an industrial or residential setups. These ultrasonic flowmeters can work on different measurement mechanisms which are discussed below.

1.2.4 Ultrasonic flow measurement principle

An ultrasonic flowmeter works on one of the following measuring principles.

- Doppler measurement
- Cross-correlation measurement
- Time of flight measurement

Each of these techniques are discussed below. These measurement techniques are used both in clamp-on and in-line ultrasonic flowmeters.

1.2.4.1 Doppler measurement

In this measurement technique, the fluid is seeded with particles which act as ultrasonic wave scatterers (Atkinson, 1976). These particles cause a frequency shift in the ultrasonic wave which is proportional to the particle velocity. This technique measures the velocity of various particles (Baker, 2000). The accuracy of such flowmeters depends on particle

concentration per unit volume, spatial location and flow profile (Sanderson & Yeung, 2002). The uncertainty in measurements increases compared to uniform flow conditions due to flow disturbances in the pipe networks. According to Sanderson & Yeung (2002) the uncertainty in measurements of such flowmeters is close to $\pm 10\%$.

1.2.4.2 Cross-correlation measurement

This method of ultrasonic flow metering is used to measure multiphase flows or flows with particles (Merzkirch et al., 2005). Worch (1998) proposed the application of this measuring principle in clean fluids with air bubbles and turbulent eddies. The schematic of a clamp-on ultrasonic flowmeter working on the cross-correlation principle is shown in figure 9 below. Two pairs of transducers are mounted onto the pipe which are separated by a small distance. A constant ultrasonic signal is generated by the transducer which propagates inside the pipe wall and fluid. Particles / bubbles / eddies modulate the phase of the ultrasonic signal which is detected by the transducer (Baker, 2000).

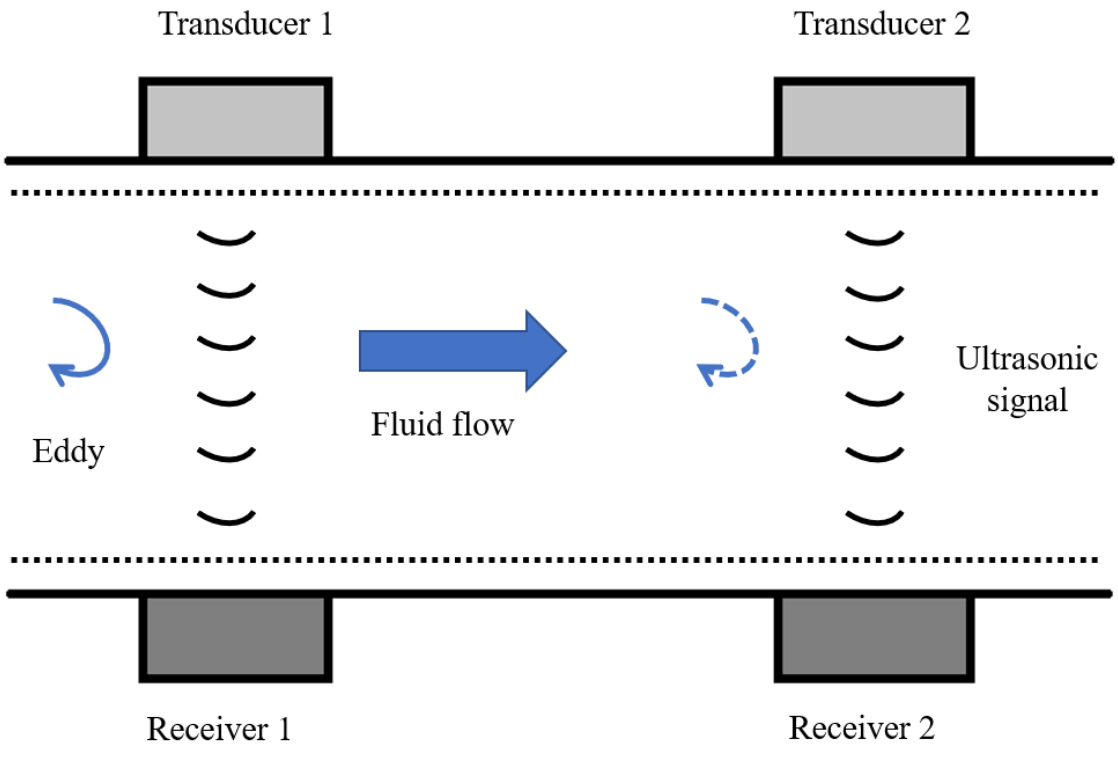

Figure 1.20 Schematic of the cross-correlation principle for an ultrasonic flowmeter

The upstream sensor detects a disturbance at time t while the downstream sensor detects the same fluctuation at time $t + \tau$. The correlation (similarity) between the two signals is computed which provides the transit time of that fluctuation. The transit time of the fluctuation is used to estimate the flow velocity. The uncertainty of such a measurement ranges from $\pm 1\% - \pm 5\%$ according to Sanderson & Yeung (2002) and Worch (1998).

1.2.4.3 Time-of-flight measurement

This principle estimates the time taken by the ultrasonic wave while propagating from one transducer to another. For a single pair of transducers, they can be mounted in one of three arrangements as shown in figure 1.21 below.

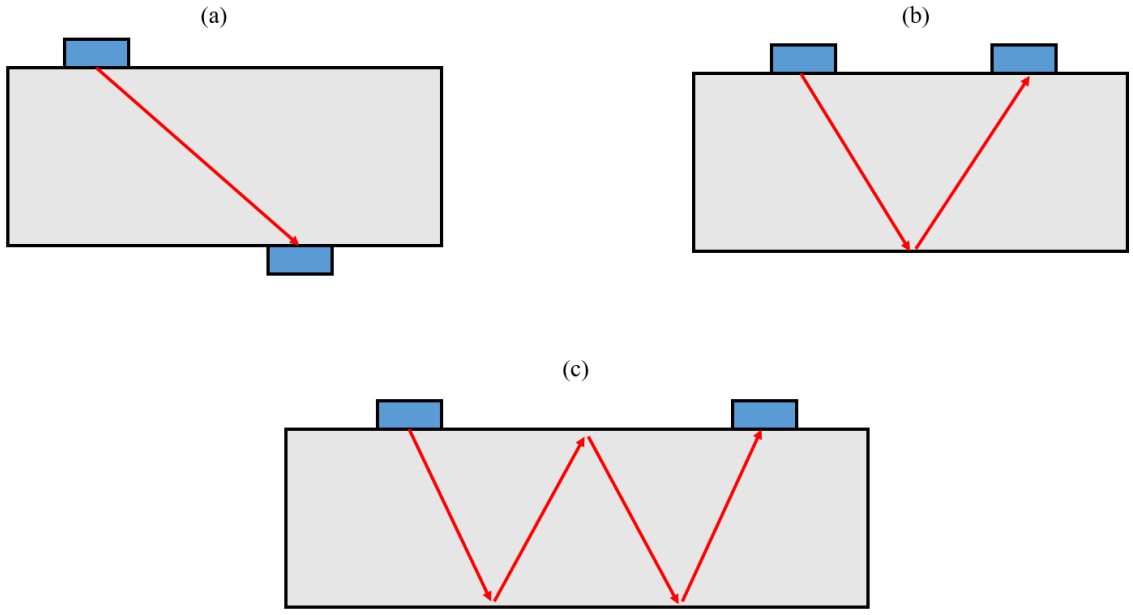

Figure 1.21 Clamp-on transducer mounting mechanisms; (a) Z-type, (b) V-type and (c) W-type

The path taken by an ultrasonic wave inside the pipe depends on the location of the transducers relative to each other (Mahadeva et al., 2009). If the transducers are mounted on opposite sides of the pipe (Z-type), the ultrasonic wave takes a straight path inclined at a specific angle (as shown in (a) in figure 1.21). If the transducers are mounted on one side of the pipe (in the same plane), then, depending upon the distance between the transducers, the ultrasonic wave would either undergo one reflection or two reflections which

correspond to V-type or W-type ((b) or (c) in figure 1.21) arrangements, respectively. Usually, for pipes with smaller diameters a V-type or W-type arrangement is used so that the ultrasonic wave takes more time to travel inside the fluid which increases the accuracy of time-of-flight principle (Schwery et al., 2012). However, for large pipe diameters the V-type or Z-type arrangement can be used (Schwery et al., 2012). If a W-type arrangement is used on a large diameter pipe, the strength of the received signal would be much less, rendering the signal useless because the signal loses its energy as a result of travelling large distances in such a pipe.

The manufacturers do not publish the algorithm and correction factors used in the time-of-flight measurement (Stoker et al., 2012). This section provides the basic mathematics used to estimate the flow velocity from the time-of-flight measurement. Figure 1.22 shows a schematic of clamp-on flowmeter configured in a V-type arrangement. The upstream transducer transmits an ultrasonic signal which travels in the direction of the fluid flow and reaches the downstream transducer (Schwery et al., 2012). After that, the downstream transducer transmits an ultrasonic signal which travels in the opposite direction to the fluid flow and is received by the upstream transducer. The ultrasonic signal travelling in the direction of the fluid flow travels faster when compared to the signal moving opposite to the direction of the fluid flow (Mahadeva et al., 2009). This difference in the time of flight of both signals is estimated and used to compute the velocity of the fluid integrated over the acoustic path.

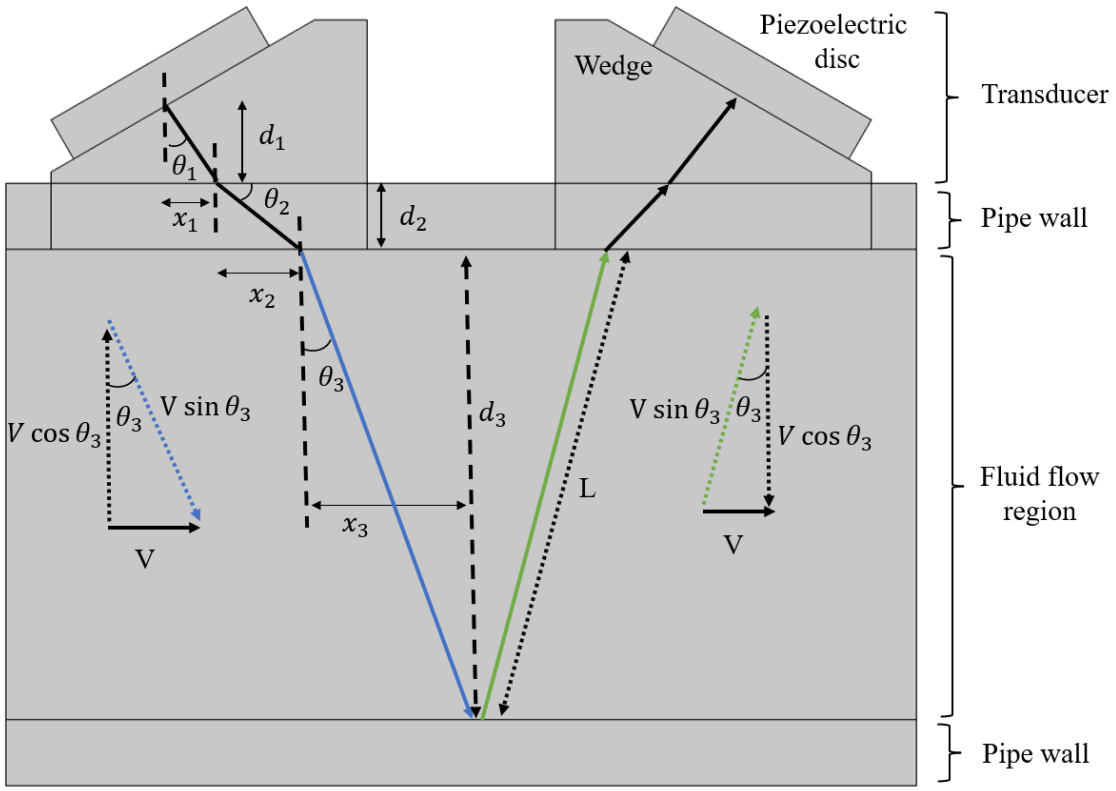

Figure 1.22 Schematic of the Clamp-on ultrasonic flowmeter for the Time-of-flight measurement principle

The details of the variables shown is figure 1.22 are as follows:

θ_1 is the angle of the ultrasonic wave in the wedge, or the piezoelectric disc inclination angle.

θ_2 is the angle of ultrasonic wave in the pipe wall.

θ_3 is the angle of ultrasonic wave in the fluid.

d_1 is the vertical distance travelled by the wave in the wedge

d_2 is the pipe thickness

d_3 is the internal diameter of the pipe

V is the fluid flow velocity

$x_1, x_2\ and\ x_3$ are the horizontal distances travelled by the wave in the wedge, pipe wall and fluid, respectively.

An ultrasonic wave travelling with the speed of sound c makes an angle θ_3 inside the fluid. The velocity of the fluid V can be written in components with respect to the angle θ_3, as shown in figure 1.22. The direction of the wave inside the fluid (travelling with a velocity c) aligns with the sine components of the fluid velocity, as can be seen in the blue and green lines in figure 1.22.

For an ultrasonic wave inside the pipe travelling in the direction of fluid flow, the time taken by the wave to reach the other transducer is given by:

$$t_1 = \frac{L}{c+V\sin\theta_3} + \frac{L}{c+V\sin\theta_3} \tag{1.1}$$

where $L = {}^{d_3}/_{\cos\theta_3}$

$$t_1 = \frac{2d_3}{\cos\theta_3(c+V\sin\theta_3)} \tag{1.2}$$

Similarly, for an ultrasonic wave travelling in the opposite direction to the fluid flow, the time taken by the wave to reach the other transducer is given by:

$$t_2 = \frac{L}{c-V\sin\theta_3} + \frac{L}{c-V\sin\theta_3} \tag{1.3}$$

$$t_2 = \frac{2d_3}{\cos\theta_3(c-V\sin\theta_3)} \tag{1.4}$$

Subtracting $t_2 - t_1$ gives:

$$t_2 - t_1 = \frac{2d_3\ V\sin\theta_3}{\cos\theta_3[(c)^2-(\mathrm{V}\sin\theta_3)^2]} \tag{1.5}$$

Adding $t_2 + t_1$ gives:

$$t_2 + t_1 = \frac{2d_3\, c}{\cos\theta_3[(c)^2 - (\mathrm{V}\sin\theta_3)^2]} \tag{1.6}$$

Taking the ratio gives:

$$\frac{t_2 - t_1}{t_2 + t_1} = \frac{V\sin\theta_3}{c} \tag{1.7}$$

$$V = \frac{t_2 - t_1}{t_2 + t_1}\left(\frac{c}{\sin\theta_3}\right) \tag{1.8}$$

The above equation can be represented in terms of the velocity and the angle that the ultrasonic wave makes in the wedge of the flowmeter. Using Snell's Law:

$$V = \frac{t_2 - t_1}{t_2 + t_1}\left(\frac{c_{wedge}}{\sin\theta_1}\right) \tag{1.9}$$

The time taken by the wave to propagate inside the wedge to reach the wedge-pipe wall boundary can be written by:

$$t_{wedge} = \frac{d_1}{c_{wedge}\cos\theta_1} \tag{1.10}$$

The time taken by the wave to propagate inside the pipe wall to reach the pipe wall-fluid boundary can be written by:

$$t_{wall} = \frac{d_2}{c_{wedge}\cos\theta_2} \tag{1.11}$$

The time taken by the wave to propagate inside the wedge and pipe wall is denoted as t_{delay} which can be written as:

$$t_{delay} = 2 \times (t_{wedge} + t_{wall}) \tag{1.12}$$

For a wave propagating in the direction of the fluid flow, the total time taken by the wave to propagate inside both transducers and the fluid is given by

$$t_{down} = (t_1 + t_{delay}) \tag{1.13}$$

$$t_1 = (t_{down} - t_{delay}) \tag{1.14}$$

Similarly, for a wave which is propagating in the opposite direction of the fluid flow, the total time taken by the wave to propagate inside both transducers and the fluid is given by

$$t_{up} = (t_2 + t_{delay}) \tag{1.15}$$

$$t_2 = (t_{up} - t_{delay}) \tag{1.16}$$

Replacing t_2 and t_1 in equation 2.9

$$V = \frac{t_{up} - t_{down}}{t_{up} + t_{down} - 2t_{delay}} \left(\frac{c_{wedge}}{\sin\theta_1}\right) \tag{1.17}$$

where $\Delta t = t_{up} - t_{down}$

$$V = \frac{\Delta t}{t_{up} + t_{down} - 2t_{delay}} \left(\frac{c_{wedge}}{\sin\theta_1}\right) \tag{1.18}$$

Equation 1.18 gives the velocity of the fluid integrated over the acoustic path if the time of flight of both waves travelling in and opposite to the direction of the fluid flow are known.

The numerical study conducted in this thesis provides the signals moving both in and opposite to the direction of the fluid flow. Cross-correlation is computed between the signals to provide the time difference between the signals Δt.

The flowrate for a circular pipe section can be computed by

$$Q = V_a A = \left(\frac{V}{K}\right) \frac{\pi . {d_3}^2}{4} \tag{1.19}$$

where d_3 is the internal pipe diameter, V is the velocity of the fluid integrated over the acoustic path obtained from equation 1.18, V_a is the velocity integrated over the pipe cross-section and K is a flow profile correction factor.

This velocity (obtained from equation 1.18) can be converted to a velocity integrated over the pipe cross section if the fluid profile is known. A flow profile correction factor “K” can be multiplied to the velocity obtained from equation 1.18. Various components in pipe

networks cause disturbances in flow velocity profiles. Section 1.2.7.4 discusses the available literature on the uncertainty associated with clamp-on ultrasonic flowmeters due to the flow profile shape.

1.2.5 Background of Acoustic waves

Waves which require a medium to transport their energy from one point to another are referred to as mechanical waves (Bécherrawy, 2012). They are produced due to the oscillations of matter. Examples of mechanical waves are water waves, sound waves and seismic waves. Mechanical waves are of three types: Longitudinal, Transverse and Surface.

- Longitudinal waves: When the oscillation of the medium particles is in the direction or opposite to the direction of the propagation of the wave then such waves are called longitudinal waves. They are also called compression or pressure waves because they produce compression (increase pressure) and de-compression (decrease pressure) in the medium as they move. Examples include sound waves and ultrasound waves. (Russell, 2016)

- Transverse waves: When the oscillation of the medium particles is perpendicular to the direction of propagation of the wave then such waves are called transverse waves. They usually occur due to shear stress in elastic solids. Examples include electro-magnetic waves, such as light. (Russell, 2016)

- Surface waves: They propagate along the interface of two media with different densities and decay exponentially. Examples include waves on the surface of ocean, Rayleigh or Love waves that travel along the surface of elastic solids. (Russell, 2016)

Particle velocity, acoustic pressure and intensity are the quantities that describe acoustic waves (Pierce, 2019). These waves travel with an acoustic velocity depending on the speed of sound of the medium. At the interface of two media, these waves undergo phenomena like reflection and refraction similar to light which can be characterized by Snell's law.

$$\frac{\sin\theta_{incident}}{\sin\theta_{transmitted}} = \frac{c_{incident}}{c_{transmitted}} \tag{1.20}$$

where $c_{incident}$ is the speed of sound in incident medium, $c_{transmitted}$ is the speed of sound in the transmitted medium, $\theta_{incident}$ is the angle of incidence of the wave and $\theta_{transmitted}$ is the angle the wave makes in the transmitted medium.

A phenomenon similar to total internal reflection occurs in acoustic waves. According to total internal reflection, an incident wave having an incident angle greater than the critical angle undergoes complete internal reflection. As the refraction angle cannot be greater than 90^0, placing $\theta_{transmitted} = 90^0$ and $\theta_{incident} = \theta_c$ gives the equation for the critical angle as below.

$$\theta_c = \sin^{-1}\left({}^{c_{incident}}/_{c_{transmitted}}\right) \tag{1.21}$$

However, in acoustic waves there are two critical angles corresponding to the longitudinal and transverse speed of sound in the transmitted medium, as given by eq 1.22 using eq 1.21.

$$\sin^{-1}\left(\frac{c_{longitudinal\ incident}}{c_{longitudinal\ transmitted}}\right) < \theta_c < \sin^{-1}\left(\frac{c_{longitudinal\ incident}}{c_{transverse\ transmitted}}\right) \tag{1.22}$$

Depending upon the incident angle there are three scenarios: (Mahadeva et al., 2009)

- If the incident angle is less than the 1st critical angle, then the incident longitudinal wave will have both longitudinal and transverse waves in the transmitted medium.
- If the incident angle is between the two critical angles there is only a transverse wave in the transmitted medium. A longitudinal wave in the transmitted medium converts to a surface wave.
- If the incident angle is greater than the 2nd critical angle, then neither longitudinal nor transverse waves enter the transmitted medium. The phenomenon of total internal reflection occurs.

For the numerical study conducted in this thesis, the angle of a piezoelectric disc (θ_1) is selected following the above guidelines. The 1st and 2nd critical angles estimated from eq 1.22 are 20.7^0 and 41.6^0 respectively. Any angle between the two critical angles can be

chosen so that there is a longitudinal wave in the transducer, a transverse wave in the solid wall of the pipe and a longitudinal wave in the liquid. Due to this, an arbitrary angle of $\theta_1 = 30^0$ is chosen which is between the 1st and 2nd critical angles.

1.2.6 Uncertainty in clamp-on ultrasonic flowmeters

The manufacturers of clamp-on ultrasonic flowmeters claim an uncertainty of 1% (Baker, 2000). This could be true when the flowmeter is installed in ideal conditions and locations. In realistic scenarios often there are non-ideal conditions like an unknown internal pipe condition or upstream disturbance to the flow due to pipe fittings. The factors that affect the uncertainty of a clamp-on flowmeters are as follows.

- Distortion in the fluid flow profile due to disturbances in the pipe network, like bends, contractions, expansions, valves and pumps, air bubbles or contamination of the fluid.

- Unknown pipe conditions, like roughness or fouling due to corrosion on the inner side of the pipe and error in the input of pipe dimensions or material during installation of the flowmeter.

Figure 1.23 below shows some *in-situ* installation sites of flowmeters

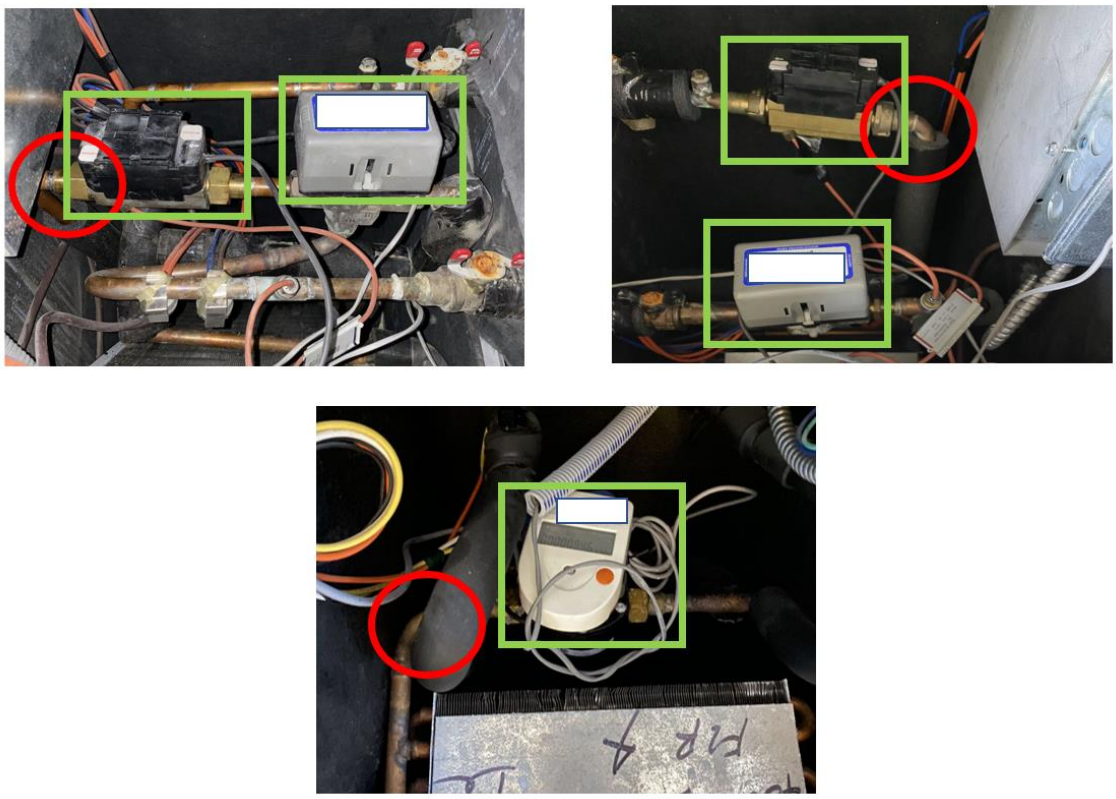

Figure 1.23 *In-situ* flowmeter installation locations (reproduced with the permission of Mr. N Dudalski)

It can be seen in the above figure that only confined spaces are available for meter installation. Such locations have pipe elbows as marked by red circles. The flowmeters are marked by green rectangles. From visual inspection of these photographs, the pipes seem to be of ¾ inch diameter. The reasons of uncertainty in the measurements of a clamp-on ultrasonic flowmeter outlined in the points above are discussed in detail later in this section.

1.2.6.1 Pipe roughness

The pipe's internal condition like wall roughness, corrosion and fouling are unknown parameters when installing a flowmeter in an existing pipe network. An experimental study conducted by Dane & Wilsack (1999) suggests that a rough pipe installed upstream of an in-line ultrasonic gas flowmeter causes an increase of 0.1-0.2% in the flowrate measurement. Zanker (1999) and Calogirou et al. (2001) conducted theoretical studies regarding the effect of pipe roughness on the fluid flow profile inside a pipe. Zanker (1999)

proposed that for a developed turbulent flow in a pipe, the Reynold's number and roughness variations could cause 4% - 9% uncertainty in the flow measurement by an ultrasonic flowmeter. Similarly, Calogirou et al. (2001) estimated that for a developed turbulent flow in a pipe, an increase in wall roughness from $4\mu m - 20\mu m$ will result an over-reading of 0.5% in an in-line ultrasonic flowmeter measurement. If the pipe roughness increases from $1\mu m - 95\mu m$, it can cause an uncertainty in the measurement of a clamp-on ultrasonic flowmeter by 1.5% (Mori et al., 2006). A moderately corroded pipe (rms roughness height of 0.2mm and roughness length of 5mm), the error induced in the measurement of a clamp-on ultrasonic flowmeter due to roughness can be around 2% (Gu & Cegla, 2019). According to section 1.4, the effects of pipe roughness on the measurement uncertainty of a clamp-on ultrasonic flowmeter is outside the scope of this thesis.

1.2.6.2 Installation error

Depending on the type of fluid, material and dimensions of the pipe, the separation distance between the transducers is estimated by the microcontroller of the flowmeter. Snell's law is applied to the ray transmitting from the piezoelectric disc and tracing this ray as it enters the pipe wall, propagates through the fluid and is received at the receiver provides the distance between the transducers. So, an error in the measurement of the pipe dimensions or human input error leads to a weak signal quality which causes uncertainty in the measurement.

Uncertainty caused by installation error was investigated by Mahadeva et al. (2009) and Asikainen & Halttunen (2000) which includes repeatability, the separation distance (V-type arrangement) between the transducers and the effect of temperature. Before clamping a transducer onto a pipe, an acoustic coupling gel is applied at the location of installation to maintain the signal quality. So, repeatability means clamping and un-clamping the transducers and estimating any uncertainty at various flowrates. Schwery et al. (2012) also estimated uncertainty associated with repeatability by taking 6 measurements within flowrate range of 5.4 - 144 m^3/hr.

Experiments were carried out by Schwery et al. (2012) in the laboratory and in the field using a clamp-on ultrasonic flowmeter in a Z-type arrangement. The internal pipe

diameters ranged from 13.15-502.9mm with flow velocity ranging from 0.25-5.1m/s. The authors concluded that for pipes with internal diameter of 10-25mm an 8Mhz frequency transducer should be used, 25-200mm internal diameter pipes should use a 4Mhz frequency transducer and 200-2000mm internal diameter pipes should use 1Mhz frequency transducers, for reliable readings. The data presented by the author does not agrees with his claim of dependence of frequency on the pipe diameters. The uncertainties in a clamp-on ultrasonic flowmeter measurement associated with the above factors are given in Table 1.5.

Table 1.5 Uncertainty in the measurement of a clamp-on ultrasonic flowmeter due to installation errors

	(Mahadeva et al., 2009)	**(Schwery et al., 2012)**	**(Asikainen & Halttunen, 2000)**
Repeatability	$\pm 0.2\%$	$\pm 0.4\%$	$\pm 0.38\%$
Effect of temperature	$0.05\%/℃$	$0.5\% / \pm 15℃$	-
Separation distance while keeping transducers in one plane	1% error if shift in separation distance is $\pm 1mm$	0.1% error if shift in separation distance is $\pm 5\%$	-
Angular displacement of transducer	0.45% error if one transducer is shifted 5mm around the circumference of the pipe	-	-
Outer diameter	-	Error of 1mm in outer diameter causes 1% uncertainty in flowrate	-

Pipe wall thickness	-	Error of 0.5 mm in pipe thickness causes 11% uncertainty in flowrate	Error of 0.1 mm in pipe thickness causes 1.1% uncertainty in flowrate

1.2.6.3 Flow profile distortion due to pipe network disturbances

In pipe networks bends, valves, contractions and expansions cause flow turbulence and flow profile distortions. These disturbances cause uncertainty in the measurement of a clamp-on ultrasonic flowmeter. Sanderson & Yeung (2002) outlined guidelines or best practices for the application/installation of clamp-on ultrasonic flowmeters by collaborating with the users and manufacturers of these flowmeters. The authors have provided the distances downstream of a specific pipe fitting which allow for the uncertainty in the measurement of the ultrasonic flowmeter to be less than 2%. They are tabulated in table 1.6 below. The authors have not mentioned about the range of pipe diameters for which the guidelines mentioned in table 1.6 are applicable. Each clamp-on ultrasonic flowmeter manufacturer suggests straight pipe sections downstream of a pipe fitting to keep the uncertainty in the measurements of the flowmeter at a minimum level (Masasi et al., 2017). Those authors have presented some distances (mentioned in table 1.6), but they have not quantified the uncertainty in the measurement of the flowmeter when installing the meter according to the specified distances. In addition, they have not mentioned the pipe sizes to which these recommendations apply.

Table 1.6 Recommended distance between the pipe disturbance and flowmeter installation

(Sanderson & Yeung, 2002)		**(Masasi et al., 2017)**
Disturbance	x/d required to reduce uncertainty in the measurement below 2%	Recommended downstream distance x/d

Conical contraction	4	10
Conical expansion	18	30
Single 90^0 bend	30	10
Two 90^0 in U	22	-
Two 90^0 in perpendicular plane	47	-
Butterfly valve 2/3 open	18	-
Globe valve 2/3 open	15	-
Gate valve 2/3 open	20	-
Tee	-	50
Valve	-	30
Pump	-	50

For a uniform turbulent velocity profile in a smooth pipe, the velocity "V" obtained from equation 1.18 (velocity integrated over the acoustical path measured by the clamp-on ultrasonic flowmeter) is converted to the velocity integrated over the pipe cross section "V_a" by applying a correction factor "K which is given by:

$$K = \frac{V}{V_a} \tag{1.23}$$

For a turbulent pipe flow, the velocity profile can be represented by empirical relation known as power law which is given by: (Schlichting & Gersten, 1979)

$$\frac{u(r_w)}{U_{max}} = \left(1 - \frac{r_w}{R}\right)^{1/n} \tag{1.24}$$

where $\left(1/n\right) = 0.2525 - 0.0229\log_{10}(Re)$ and $3 \times 10^3 < Re < 5 \times 10^6$.

$$Q = V_a.A = \int u(r_w)dA = U_{max}\int_0^R \left(1 - \frac{r_w}{R}\right)^{1/n} dr_w = U_{max}2\pi {r_w}^2 \frac{n^2}{(n+1)(2n+1)} \quad (1.25)$$

$$V_a = U_{max}\frac{n^2}{(n+1)(2n+1)} \quad (1.26)$$

where $u(r_w)$ is the velocity at a distance r_w from the pipe wall, U_{max} is the maximum velocity, R is the pipe radius. The correction factor $K = 1.119 - 0.011\log_{10}(Re)$, estimated for a turbulent velocity profile in a smooth pipe (using eq 1.23, 1.24 and 1.26) is presented by Lynnworth (1979) and Kocis & Figura,(1996). It is used in equation 1.19 to reduce the uncertainty in the flowrate due to the velocity "V" (integrated over the acoustical path). Sanderson & Yeung (2002), Schwery et al. (2012), Iooss et al. (2002) and Jung & Seong (2005) have used this correction factor in their studies. If the correction factor "K" described above is not applied then an uncertainty of 0.35% in the flowrate measured by a clamp-on ultrasonic flowmeter (Z-type arrangement) is observed according to Iooss et al. (2002).

A correction factor similar to the one above was proposed by Zanker (1999) and Zhang et al. (2019) for a clamp-on ultrasonic flowmeter. For a Z-type transducer arrangement, the velocity along the acoustic path "V_c" can be obtained by integrating eq 1.24 over the pipe radius.

$$V_c = \int u(r_w)dr = U_{max}\int_0^R \left(1 - \frac{r_w}{R}\right)^{1/n} dr_w = U_{max}\frac{n}{(n+1)} \quad (1.27)$$

$$V_c = U_{max}\frac{n}{(n+1)} \quad (1.28)$$

$$K = \frac{V_a}{V_c} = \frac{2n}{(2n+1)} \quad (1.30)$$

where the value of n varies with Reynolds number (example n=6 $Re = 4 \times 10^3$, for n=7 $Re = 2.56 \times 10^4$) as defined by the power law representation of velocity profiles inside a pipe. In order to verify the proposed theoretical correction factor, Zhang et al. (2019)

conducted experiments at various Reynolds number. They concluded a relative error of 0.25% between the proposed theoretical correction factor and experimental data.

The correction factors discussed above only applies to a uniform turbulent flow in a smooth pipe. As discussed in the section 1.2.1, the fluid flow profile is distorted by a 90^0 elbow due to the presence of secondary flow. So, Moore et al. (2000) and Zanker (1999) theoretically estimated the uncertainty in the measurement of a clamp-on ultrasonic flowmeter using the velocity profile at the outlet of an elbow (as shown in figure 1.24).

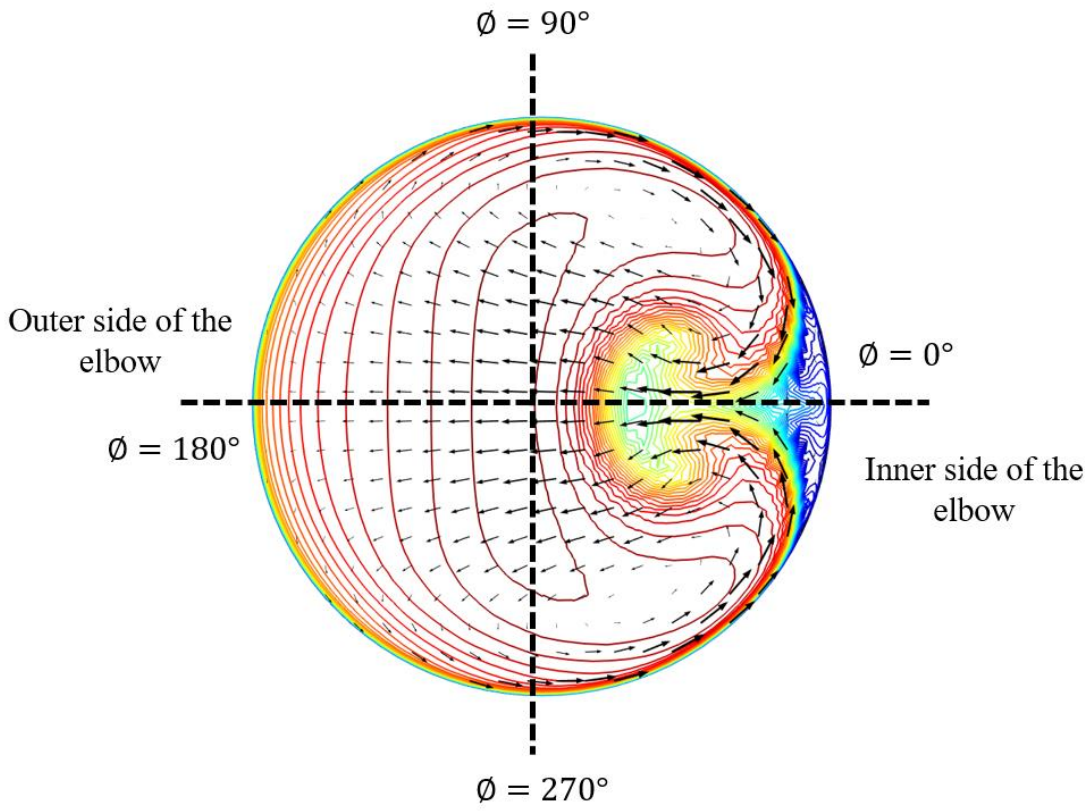

Figure 1.24 Orientation of the clamp-on ultrasonic flowmeter's transducers relative to the secondary flow generated by the elbow

Moore et al. (2000) and Zanker (1999) theoretically proposed a value of "K=0.988 and K=1.02 respectively" (according to eq 1.30) when transducers are mounted on $\emptyset = 0° - 180°$ axis as defined in figure 1.24. Whereas if the transducers are mounted on $\emptyset = 90° - 270°$ axis as defined in figure 1.24 a value of "K=0.97 and K=0.935" are proposed

respectively. These theoretical studies have limitations as the turbulent structure changes downstream of the elbow as discussed in section 1.2.1.

The performance of a clamp-on ultrasonic flowmeter downstream of a 90^0 elbow is experimentally studied by Heritage (1989), Johnson et al. (2001), Stoker et al. (2012) and Asikainen & Halttunen (2000). The figure 1.25 shows the uncertainty in the flowmeter's measurement downstream of the elbow estimated by these authors.

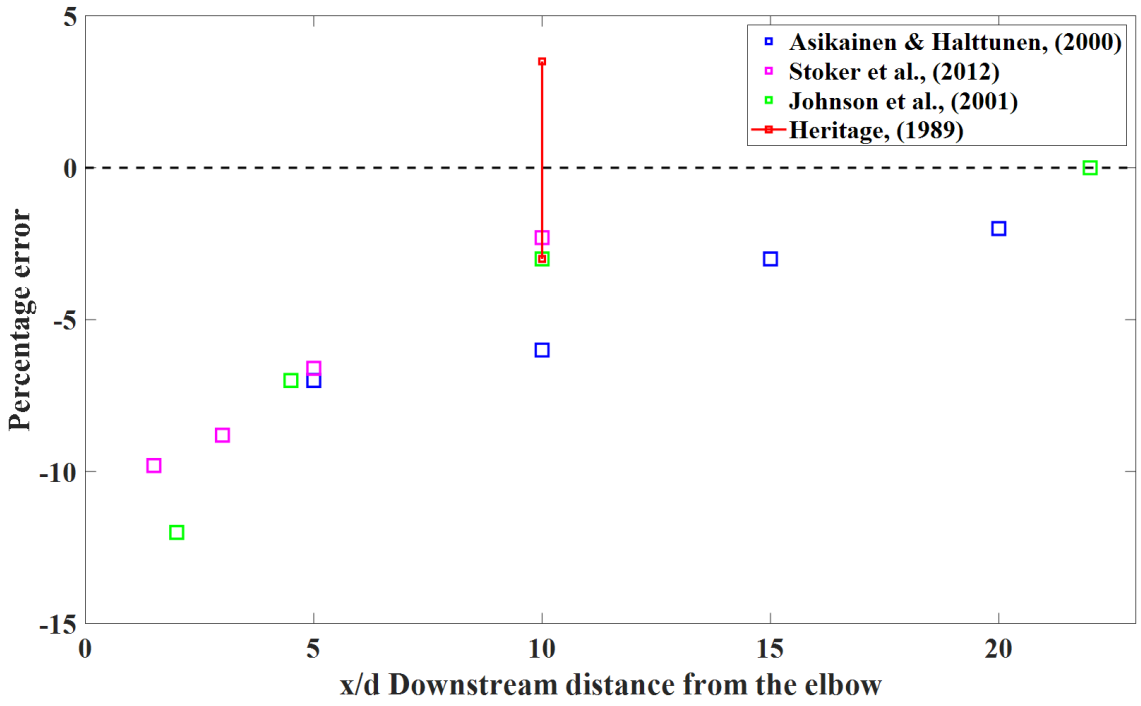

Figure 1.25 Percentage error in the clamp-on flowmeter measurement at various downstream locations

The experimental setup of Heritage (1989) has a r/d=1.5 and a turbine flowmeter was used for reference measurement. The flowrate range of the experiments was $28 - 270\ m^3/hr$. He concluded a percentage error range of -3 to +3.5% (red curve in figure 1.25) in the measurement when the flowmeter is installed at x/d=10 downstream of the elbow (where the transducers are mounted on the $\emptyset = 0° - 180°$ axis as defined in figure 1.24). A percentage error of -2 to -2.5% in the flowrate measurement when the flowmeter is installed at x/d=10, downstream of the elbow (where the transducers are

mounted on the $\emptyset = 90° - 270°$ axis as defined in figure 1.24). Johnson et al. (2001) used venturi flowmeter for reference measurement and conducted experiments in the Reynolds number range of $Re = 1.25 \times 10^5 - 5.02 \times 10^5$. Stoker et al. (2012) used magnetic flowmeter for reference measurement and conducted experiments in the range of $Re = 2.5 \times 10^5 - 7.5 \times 10^5$. Asikainen & Halttunen (2000) used Coriolis flowmeter for reference measurement and conducted experiments at the $Re = 2.25 \times 10^4$. None of the authors except Heritage (1989) have mentioned the r/d value of their experimental setups. It can be concluded from the figure 1.25 that the clamp-on ultrasonic flowmeter under predicts the flowrate when installed downstream of the elbow. The percentage error in the readings of a clamp-on ultrasonic flowmeter close to the elbow is higher compared to further downstream of the elbow. At a downstream length of x/d > 20, the percentage error reaches close to zero.

1.3 Motivation for the current project

The research conducted before the early 2000s did not have access to numerical techniques sophisticated enough to study the behaviour of clamp-on ultrasonic flowmeters. Looking at the previous section, experimental studies have been conducted to quantify the uncertainty in the measurements of a clamp-on ultrasonic flowmeter downstream of an elbow. However, there is a need for a further experimental study due to the following reasons.

- The authors of the existing research have not provided the r/d values of the pipe elbow setups used. Due to this, their results or correction factors cannot be applied to other similar pipe elbow setups.

- Those authors conducted these studies in early 2000s and, over time, the manufacturers of clamp-on ultrasonic flowmeters claim that they have improved the accuracy of the flowmeters compared to the earlier models. This improvement in the flowmeters is attributed to advanced manufacturing techniques,

advancements in piezoelectric materials, software and algorithm advancements in the newer clamp-on ultrasonic flowmeters.

In the previous section, some authors used theoretical relations or integrated the velocity of the fluid along an assumed acoustical path to determine the performance of the flowmeter downstream of a 90^0 elbow. None of the researchers have simulated the propagation of an ultrasonic signal inside a fluid flow, especially in a turbulent flow downstream of an elbow. In order to compare experimental data with numerical model results to study the performance of a clamp-on ultrasonic flowmeter, there is a need to develop a numerical model which models the entire workings of a clamp-on ultrasonic flowmeter.

This thesis addresses the numerical and experimental gaps identified above. The performance of a clamp-on ultrasonic flowmeter with and without a 90^0 elbow is carried out using a numerical and experimental approach. A numerical model is developed using the COMSOL software which simulates the propagation of an ultrasonic signal in the transducers, pipe wall and fluid inside the pipe. Similarly, five clamp-on ultrasonic flowmeters of the same model are tested in a flow rig which will also validate the performance of this specific flowmeter model. The numerical and experimental results help to propose a correction factor which is valid for an *in-situ* installation of these flowmeters in similar flow conditions.

1.4 Scope of present work

In this thesis, the effect of a 90^0 elbow on the measurement uncertainty of a clamp-on ultrasonic flowmeter is discussed. The table below states the parameters which define the scope of the present study. According to Hartogh (2018), a typical household water flowrate can vary between $0.45 - 2.72\ m^3/hr$ which is why a flowrate range of $0.2 - 2.5\ m^3/hr$ is selected for the studies conducted in this thesis.

Table 1.7 Summary of parameters used in the numerical and experimental study conducted in this thesis

Parameters	Values
Pipe size	¾ inch Stainless steel and copper
Elbow	90^0 elbow for ¾ inch pipes r/d = 1.6
Flowrate range (m^3/hr)	0.3 – 2.5
Reynolds number range	$0.34 \times 10^4 - 4.23 \times 10^4$
Flowmeter measurement downstream location x/d	1
Number of clamp-on flowmeters	5
Reference flowmeters	venturi and in-line ultrasonic

The scope of the present study is limited by the additional time that would be necessary to numerically simulate the flowmeter's performance further downstream of an elbow and for pipe disturbances other than the elbow. Parameters that are outside the scope of this study are as follows.

- Effect of pipe roughness and internal pipe condition on the performance of the clamp-on ultrasonic flowmeter.
- Performance of the clamp-on ultrasonic flowmeter downstream of a 90^0 elbow at further x/d locations.

1.5 Organization of this thesis

This thesis is organized into 5 chapters which are as follows:

- Chap 1: Introduction and literature review
- Chap 2: Numerical methodology

- Chap 3: Experimental methodology
- Chap 4: Results and discussion
- Chap 5: Conclusions and future work

1.6 Summary

This chapter has focused on the following points.

- Fluid flow inside a 90^0 elbow generates a secondary flow as it passes through the elbow. The smaller the r/d the stronger the secondary flow. The fluid flow profile inside the elbow develops a low velocity region. This secondary flow diminishes downstream of the elbow.
- There are different types of flowmeters with their respective advantages and disadvantages.
- Ultrasonic flowmeters are categorized as in-line or clamp-on. These flowmeters work on different measurement principles. The time-of-flight principle is commonly used in present day flowmeters.
- Clamp-on ultrasonic flowmeters tend to have higher uncertainty in flow measurement when compared to in-line ultrasonic flowmeters. The factors affecting this uncertainty are discussed. The gap in the research is identified which provides the motivation and scope of the present study.

The next chapter outlines the numerical technique adopted in this thesis.

Chapter 2

2 Numerical Methodology

The numerical modelling of a clamp-on ultrasonic flowmeter is conducted using COMSOL Multiphysics in this thesis. The methodology adopted using this software is discussed in detail.

2.1 Numerical modelling in COMSOL

In order to model this flowmeter, there is an interaction between 4 different physical phenomena: Fluid flow modelling, Structural modelling, Electrostatic modelling and Acoustic modelling.

- Fluid flow is modelled in a straight pipe with and without a 90^0 elbow.
- Electrostatic and structural analysis is combined to model the phenomenon of piezoelectricity in the piezoelectric material inside the transducer.
- Acoustic analysis is used to model the generation, propagation and reception of ultrasonic waves inside transducer, pipe wall and pipe fluid.

The background to these modelling approaches will be discussed initially in this chapter. The selection and validation of the fluid flow model will be presented at the end of this chapter.

2.1.1 Fluid flow modelling

The turbulent fluid flow can be modelled using Reynold's Averaged Navier-Stokes equation (RANS) or Large eddy simulation (LES). The numerical modelling of a turbulent

flow using the RANS approach divides the flow quantities into the mean and fluctuating parts. The RANS equations are used to model the mean quantities while a turbulence closure model models the fluctuations.

A flow is considered to be steady if the fluid properties (like flowrate, velocity, viscosity and density) at a point in the system do not change with time. Turbulence is an unsteady phenomenon. For fluid flow inside a pipe, the flow will reach a steady state where the rate of change of velocity and pressure with time will be small. So, such flows can be assumed as fully developed.

For a steady incompressible Newtonian fluid RANS equations in 3-D are given by:

$$\frac{\partial \bar{u}}{\partial x} + \frac{\partial \bar{v}}{\partial y} + \frac{\partial \bar{w}}{\partial z} = 0 \tag{2.1}$$

$$\rho\left[\bar{u}\frac{\partial \bar{u}}{\partial x} + \bar{v}\frac{\partial \bar{u}}{\partial y} + \bar{w}\frac{\partial \bar{u}}{\partial z}\right] = -\frac{\partial \bar{p}}{\partial x} + \mu\left(\frac{\partial^2 \bar{u}}{\partial x^2} + \frac{\partial^2 \bar{u}}{\partial y^2} + \frac{\partial^2 \bar{u}}{\partial z^2}\right) - \rho\left(\frac{\partial \overline{u\prime u\prime}}{\partial x} + \frac{\partial \overline{u\prime v\prime}}{\partial y} + \frac{\partial \overline{u\prime w\prime}}{\partial z}\right) \tag{2.2}$$

$$\rho\left[\bar{u}\frac{\partial \bar{v}}{\partial x} + \bar{v}\frac{\partial \bar{v}}{\partial y} + \bar{w}\frac{\partial \bar{v}}{\partial z}\right] = -\frac{\partial \bar{p}}{\partial y} + \mu\left(\frac{\partial^2 \bar{v}}{\partial x^2} + \frac{\partial^2 \bar{v}}{\partial y^2} + \frac{\partial^2 \bar{v}}{\partial z^2}\right) - \rho\left(\frac{\partial \overline{v\prime u\prime}}{\partial x} + \frac{\partial \overline{v\prime v\prime}}{\partial y} + \frac{\partial \overline{v\prime w\prime}}{\partial z}\right) \tag{2.3}$$

$$\rho\left[\bar{u}\frac{\partial \bar{w}}{\partial x} + \bar{v}\frac{\partial \bar{w}}{\partial y} + \bar{w}\frac{\partial \bar{w}}{\partial z}\right] = -\frac{\partial \bar{p}}{\partial z} + \mu\left(\frac{\partial^2 \bar{w}}{\partial x^2} + \frac{\partial^2 \bar{w}}{\partial y^2} + \frac{\partial^2 \bar{w}}{\partial z^2}\right) - \rho\left(\frac{\partial \overline{w\prime u\prime}}{\partial x} + \frac{\partial \overline{w\prime v\prime}}{\partial y} + \frac{\partial \overline{w\prime w\prime}}{\partial z}\right) \tag{2.4}$$

where $\bar{u}, \bar{v}\ and\ \bar{w}$ are time averaged velocities along the x, y and z axes respectively. ρ is the density of the fluid. μ is the viscosity of the fluid. The equation 2.1 is the continuity equation, whereas equations 2.2, 2.3 and 2.4 are the momentum equations along the x, y and z axes respectively.

In the momentum equations, the left hand side term denotes the change in mean momentum of the fluid, whereas the terms on the right hand side of the equation are as follows

1st term denotes stresses due to the pressure field

2nd term denotes frictional or viscous stresses

3rd term denotes the Turbulent Reynolds stresses

Closure models are used when we need to model the Reynolds stress term as a function of the mean flow. A common way to model turbulence is to assume that it is diffusive which is the basis of the eddy viscosity concept. In this thesis eddy viscosity turbulence closure models are used which are the $k-\omega$ turbulence model and the Shear-stress-transport (SST) turbulence model, due to their advantages over other models as outlined in Table 2.1.

Table 2.1 Comparison of various Turbulence models

Closure models	**Advantages**	**Disadvantages**
SA model (Spalart & Allmaras, 1992)	One equation model specifically developed for aerospace applications. Easier to solve numerically as linear behviour is assumed near the wall	It cannot be applied to other complex engineering flows where flow changes abruptly from wall-bounded to a free shear flow.
$k-\varepsilon$ model (Launder & Spalding, 1974)	Preferred for high Reynolds number flow away from the wall with relatively small pressure gradients	Not suited for simulating flow close to the wall which is a low Reynolds number region. Not suited for regions of flow separation, re-attachment, adverse pressure gradients and re-circulation.
$k-\omega$ model (Wilcox, 2006)	Applicable to both wall-bounded and free shear flows. Performs better than k-epsilon model in near wall regions and adverse pressure gradients.	Sensitive to free stream turbulent conditions.

	Improved results for shock separated flows.	
$SST\ k-\omega$ model (Menter, 1994)	Merges $k-\omega$ and $k-\varepsilon$ models in a way that near the wall the $k-\omega$ model is used which performs better in such regions and the $k-\varepsilon$ model is used in free shear flow region because it is not affected by the inlet turbulent parameters. Performs better compared to previous models in separated flows and external aerodynamics.	

2.1.1.1 $k-\omega$ model

The $k-\omega$ turbulence model proposed by Wilcox (2006) uses two equations which solve for turbulent kinetic energy k and rate of dissipation ω (specific turbulence dissipation rate) per unit turbulent kinetic energy converted into internal thermal energy.

The transport equation for k is:

$$\rho u.\nabla k = P_k - \rho\beta_o{}^{*} f_\beta k\omega + \nabla.\left((\mu + \sigma_k\mu_T)\nabla k\right) \tag{2.5}$$

where:

$\mu_T = \frac{\rho k}{\omega}$ (Turbulent eddy viscosity)

$P_k = \tau_{ij}\frac{\partial u_i}{\partial x_j}$ (Production term due to mean velocity shear)

$\tau_{ij} = \mu_T \left(2S_{ij} - \frac{2}{3}\frac{\partial u_k}{\partial x_k}\delta_{ij}\right) - \frac{2}{3}\rho k \delta_{ij}$ (Boussinesq Hypothesis: The Reynolds stress term τ_{ij} in the RANS equations are related to mean velocity gradients by this equation. The turbulent eddy viscosity μ_T is computed using turbulence closure models to close the system of RANS equations.)

$S_{ij} = \frac{1}{2}\left(\frac{\partial \overline{u_i}}{\partial x_j} + \frac{\partial \overline{u_j}}{\partial x_i}\right)$ (Mean strain-rate tensor)

$\beta_o{}^* = 0.09$, $f_\beta = \frac{1+85X_\omega}{1+100X_\omega}$, $X_\omega = \left|\frac{\Omega_{ij}\Omega_{jk}S_{ki}}{(\beta_o{}^*\omega)^3}\right|$, $\sigma_k = 0.6$

$\Omega_{ij} = \frac{1}{2}\left(\frac{\partial \overline{u_i}}{\partial x_j} - \frac{\partial \overline{u_j}}{\partial x_i}\right)$ (Mean rotation-rate tensor)

The Transport equation for ω is:

$$\rho u.\nabla\omega = \alpha\frac{\omega}{k}P_k - \rho\beta\omega^2 + \nabla.\left((\mu + \sigma_\omega\mu_T)\nabla\omega\right) + \frac{\rho\sigma_d}{\omega}\nabla k\nabla\omega \qquad (2.6)$$

where $\alpha = \frac{13}{25}$, $\beta = \beta_o f_\beta$, $\beta_o = 0.0708$, $\sigma_\omega = 0.5$, $\sigma_d = \begin{cases} 0, & \nabla k\nabla\omega \le 0 \\ \frac{1}{8}, & \nabla k\nabla\omega > 0 \end{cases}$

In equations 2.5 and 2.6, the term on the left hand side is the Convective term. The terms on the right hand side are source, sink and diffusion terms respectively. The last term on the right hand side of equation 2.6 is a cross-diffusion term which lowers the dependency of the $k-\omega$ model on free stream turbulence parameters.

Turbulent flow is significantly affected by walls due to the no-slip condition. Velocity fluctuations also vanish near the wall. Modelling near the wall is important as they are a source of turbulence. These turbulence models use various wall treatments to model flow behavior near the wall. The wall treatment adjusts according to the mesh resolution near the wall. When the mesh is fine, the wall treatment switches to a low-Reynolds number formulation. When the mesh is coarse, the wall treatment switches to a wall function. By doing this, viscosity affects near the wall are not solved by the RANS equations and instead, a log-law specifies the velocity in cells adjacent to the wall.

2.1.1.2 $SST\ k-\omega$ model

The SST turbulence model combines both the $k-\omega$ model in the region near the wall and the $k-\varepsilon$ model in the free shear flow. This model does not apply wall functions near the wall region where viscous effects are dominant which is why it is also referred to as the low Reynolds number model.

According to the standard $k-\varepsilon$ model, $\varepsilon = C_\mu k\omega$. If we replace this relation in the transport equations of the standard $k-\varepsilon$ model we end up getting the transport equations (eq 2.5, 2.6) for the $k-\omega$ model. The $SST\ k-\omega$ model blends between the $k-\omega$ and the $k-\varepsilon$ models by using a blending function $(1-F_1)$ in the cross-diffusion term (Last term in the equations 2.6 and 2.8). This blending function allows to smoothly transition between the $k-\omega$ and the $k-\varepsilon$ models. A distance "d" is defined away from the closest wall for each cell of the mesh which controls this transition. The value of F_1 varies between 0 and 1. If it is 1 then the cross-diffusion term in the equation 2.8 is zero so the resulting transport equation represents the $k-\varepsilon$ model. If the value of $F_1 = 0$ then the resulting transport equation represents the $k-\omega$ model.

The transport equation for k is:

$$\rho u.\nabla k = P - \rho\beta_o{}^* k\omega + \nabla.\left((\mu + \sigma_k\mu_T)\nabla k\right) \tag{2.7}$$

The Transport equation for ω is:

$$\rho u.\nabla\omega = \frac{\rho\gamma}{\mu_T}P - \rho\beta\omega^2 + \nabla.\left((\mu + \sigma_\omega\mu_T)\nabla\omega\right) + 2(1-F_1)\frac{\rho\sigma_{\omega 2}}{\omega}\nabla k\nabla\omega \tag{2.8}$$

$$\text{(Turbulent eddy viscosity) } \mu_T = \frac{\rho a_1 k}{\max(a_1\omega, SF_2)} \tag{2.9}$$

where $P = \min(P_k, 10\rho\beta_o{}^* k\omega)$, $a_1 = 0.31$, $S = 2\sqrt{S_{ij}S_{ij}}$ (magnitude of shear strain)

Note that the turbulent eddy viscosity μ_T for the $SST\ k-\omega$ model is different than the $k-\omega$ model. Menter (1994) noted that using the earlier expression of μ_T was over predicting the wall shear stress. In order to address this issue, he proposed a new expression for μ_T (equation 2.9) which is called “viscosity limiter”.

The expressions for blending functions F_1 and F_2 are shown below. These expressions provide a smooth transition between the models.

$$F_1 = \tanh \theta_1^{\,4} \tag{2.10}$$

where $\theta_1 = \min\left[max\left(\frac{\sqrt{k}}{\beta_o{}^{*}\omega d}, \frac{500\mu}{\rho\omega d^2}\right), \frac{4\rho\sigma_{\omega 2}k}{CD_{k\omega}d^2}\right]$, $CD_{k\omega} = \max\left(\frac{2\rho\sigma_{\omega 2}}{\omega}\nabla\omega.\nabla k, 10^{-10}\right)$

$$F_2 = \tanh \theta_2^{\,2} \tag{2.11}$$

where $\theta_2 = \max\left(\frac{2\sqrt{k}}{\beta_o{}^{*}\omega d}, \frac{500\mu}{\rho\omega d^2}\right)$

All the constants in the equations 2.7 and 2.8 need to be adjusted for each cell depending upon the respective model being used to compute flow properties in that cell. So, the blending function F_1 is used to define an interpolation function shown below.

$$\emptyset\ (\beta, \gamma, \sigma_\omega, \sigma_k) = F_1\emptyset_\omega + (1 - F_1)\emptyset_\epsilon \tag{2.12}$$

where $\beta_1 = 0.075$, $\beta_2 = 0.0828$, $\gamma_1 = {}^{5}/_{9}$, $\gamma_2 = 0.44$, $\sigma_{k1} = 0.85$, $\sigma_{k2} = 1$, $\sigma_{\omega 1} = 0.5$, $\sigma_{\omega 2} = 0.856$ are the default values of constants estimated empirically by running various simulations and comparing with the experimental data.

The modelling approach for the acoustic simulations is discussed further.

2.1.2 Piezoelectric modelling

Piezoelectricity is the accumulation of charge in a material in response to an applied stress, this phenomenon is referred to as the direct piezoelectric effect. If a piezoelectric material is placed in an electric field the solid develops a strain, which is referred to as the inverse piezoelectric effect. Piezoelectric materials have an unsymmetrical crystal structure where atoms are arranged in an electrically neutral balance. When an external pressure is applied the atoms rearrange in such a way that one side of the material is positively charged and other side as negatively charged. This state of the material is referred to as material polarization. The relationship between material polarization and deformation can be described in two ways; strain-charge form or stress-charge form.

The strain-charge form can be written as follows: (Tiersten, 1988)

$$S = s_E T + d^T E \tag{2.13}$$

$$D = dT + \varepsilon^T E \tag{2.14}$$

where S is the strain (dimensionless quantity), T $\left({}^{N}/_{m^2}\right)$ is the shear stress, E $\left({}^{V}/_{m}\right)$ is the electric field and D $\left({}^{C}/_{m^2}\right)$ is the electric displacement field

Material properties: s_E $\left({}^{m^2}/_{N}\right)$ is the material compliance, d $\left({}^{m}/_{V} = {}^{C}/_{N}\right)$ is the coupling property, d^T $\left({}^{m}/_{V}\right)$ is the piezoelectric charge constant and ε^T $\left({}^{F}/_{m} = {}^{C}/_{Vm}\right)$ is the relative permittivity at constant stress.

The piezoelectric material is modelled using the "Solid mechanics" and "Electrostatics" user interfaces of COMSOL which are coupled via linear constitutive equations (2.13 and 2.14) above which correlate stress and strain with the electric field and displacement.

One of the most widely used piezoelectric materials is lead-zirconate-titanate "PZT-5H" (Piezo, 2020). This material is physically strong, inexpensive to produce and chemically inert (Erturk & Inman, 2011). In the experimental study conducted in this thesis, the material of the piezoelectric discs used in the clamp-on ultrasonic flowmeters is not disclosed by the manufacturer. Due to these reasons, in the numerical study conducted in this thesis, PZT-5H is used as the piezoelectric disc in the transducers.

When a piezoelectric material is exposed to an AC electric field, it changes dimensions cyclically with the frequency of the field. At the resonance frequency, the piezoelectric material converts the electrical energy into the mechanical energy efficiently. In the transducers of a clamp-on ultrasonic flowmeter the ultrasonic wave pulses are generated periodically. In the present numerical study, the interrogation signal generated at the transmitter is a sine wave modulated with a Gaussian pulse. This modulation retains one oscillation of the sine wave and results in the interrogation signal shown in the figure 2.2.

$$Interrogation\ Signal = V \sin 2\pi f_o(t) \times \exp\left(\frac{-(t-T_0)^2}{2\sigma^2}\right) \tag{2.15}$$

where V is the applied voltage, $T_o = 1\mu s$ is the time period of the ultrasonic pulse and f_o is the frequency of the ultrasonic pulse. The variance $\sigma = 0.4 * T_0$ and $0 < t < 5T_o$. These values are selected to retain the first oscillation of the sine wave and the resulting interrogation signal looks like a pulse with a sinusoidal shape shown in the figure 2.2.

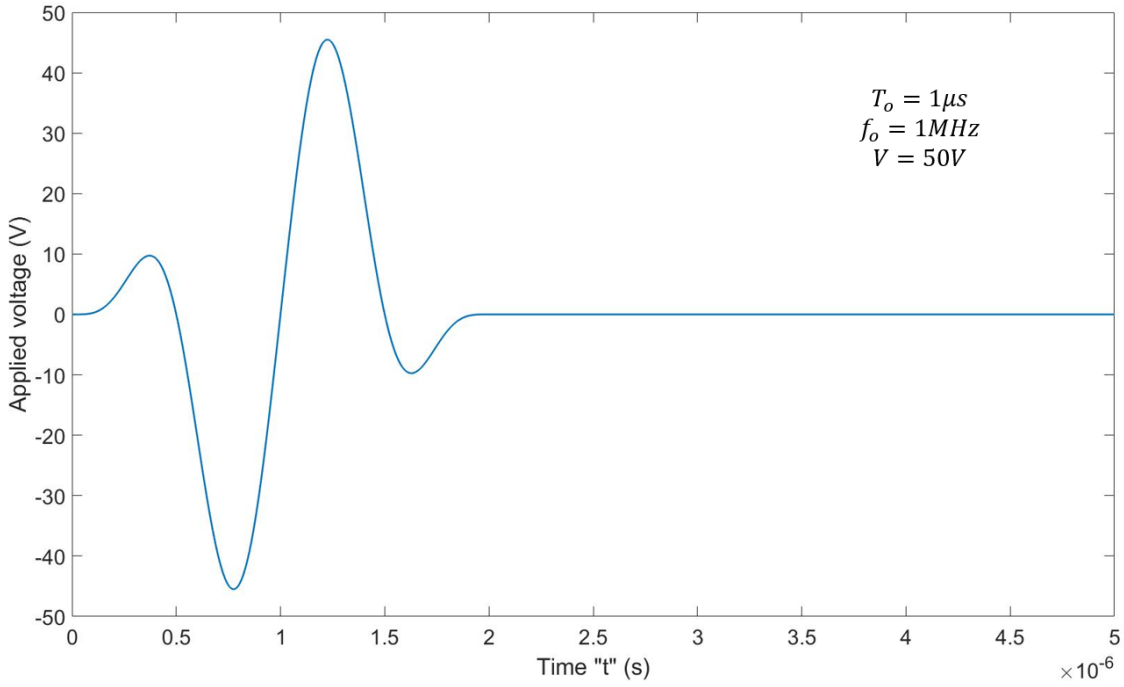

Figure 2.1 Interrogation signal applied at transducer

This interrogation signal will cause a mechanical deformation in the piezoelectric material. This deformation causes a strain in the transducer which comprises of piezoelectric disc attached to a wedge (diagram shown in figure 2.3). This phenomenon generates an ultrasonic wave which travels across the transducer, the pipe wall and the fluid.

2.1.3 Acoustic modelling

The numerical modelling of a clamp-on flowmeter comprises of 3 steps/studies which are as follows.

- Modelling of the transmitter using the “Pressure acoustic” user interface of COMSOL

- Modelling the Ultrasonic wave propagation inside the fluid using the “Convected wave equation” user interface of COMSOL

- Modelling receiver using the “Solid mechanics” and “Electrostatics” user interfaces of COMSOL.

2.1.3.1 Transmitter modelling

The phenomenon of piezoelectricity in the transducer is modelled as discussed in the section 2.2.2. The interrogation signal applied to the piezoelectric disc generates an ultrasonic wave which has a certain velocity and pressure. In order to model the generation of the ultrasonic wave, a small finite domain of static fluid is attached to the transmitter (as shown in figure 2.3). The boundary of the fluid and the pipe wall is called “transmitter-fluid interface”. The modelling of this interface acts as a boundary condition applied to the second study where propagation of the ultrasonic wave inside the fluid is modelled. A transient (time dependent) study is carried out as we are interested in estimating the time-of-flight of the ultrasonic signals.

The “Pressure acoustics” user interface of COMSOL, computes the small pressure variations in the overall fluid pressure caused by the propagation of the acoustic waves in a fluid. It solves the scalar wave equation which can be written as follows. (Pierce, 2019)

$$\frac{1}{\rho c^2}\frac{\partial^2 p_t}{\partial t^2} + \nabla . \left(-\frac{1}{\rho}(\nabla p_t - q_d)\right) = Q_m \tag{2.16}$$

$$p_t = p_0 + p_1 \tag{2.17}$$

where p_t is the total pressure, p_0 is the fluid pressure, p_1 is the variation in pressure, ρ is the density of fluid, c is the speed sound in the fluid, q_d is the dipole domain source and Q_m is the monopole domain source.

A monopole domain source has uniform strength in all directions. This source term added in a model can represent a heat source in the domain causing pressure variations. A dipole domain source is generally stronger in two opposite directions. Such a source can represent a uniform background flow convecting the sound field. These source terms are not used in

this study because the effect of the background fluid flow is modelled in the next step (second study). In the transmitter modelling study, the pressure perturbations caused by the propagation of acoustic wave in a fluid are computed. This study (generation of acoustic waves) acts as a boundary condition for the second study. The figure 2.3 shows the generation of the acoustic waves in the finite fluid domain attached to the transducer.

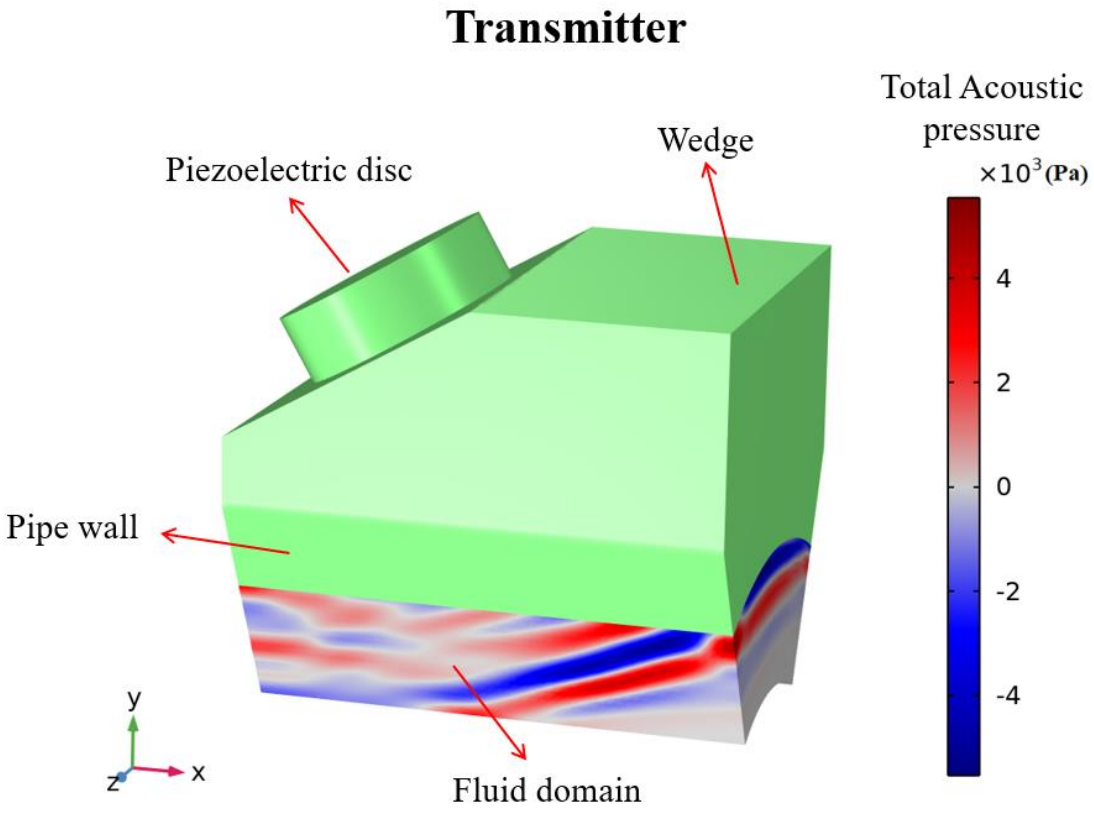

Figure 2.2 Pressure variation due to the generation of acoustic waves in a finite fluid domain

In order to simulate wave propagation in the transducers or through the fluid inside the pipe, the wavelength associated with the acoustic waves must be resolved. The wavelength of this ultrasonic wave depends on the speed of sound of the materials through which it propagates. This wavelength has to be resolved by the mesh which demands mesh elements to be smaller than the wavelength. The resolution of the mesh depends on the type of the model and the discretization technique used by the specific study. In the present study, a

Finite element method (FEM) based pressure acoustic model is used which uses a quadratic discretization technique to discretize the domain. A quadratic or higher discretization technique resolves the curves in a domain efficiently compared to a linear discretization technique (Frei, 2016). According to Marburg (2002), maximum element size in the domain is recommended to be equal or less than $\lambda/5$ which requires a minimum of 5 mesh elements in one wavelength (λ). The clamp-on ultrasonic flowmeters used in the experimental study conducted in this thesis were connected to an oscilloscope in a laboratory to determine the operating frequency. The operating frequency of that meter is 2MHz. Mirshab (2015) states that clamp-on ultrasonic liquid flowmeters work on the operating frequency between 1-3MHz. The operating frequency of 1Mhz is used in the numerical study conducted in this thesis because the mesh required to resolve the wavelength corresponding to 1MHz is coarser compared to the one required to resolve higher frequencies than 1MHz. So, a higher operating frequency for the numerical analysis demands a higher computational resource and longer time to simulate.

2.1.3.2 Wave propagation using the Convected wave equation

The use of a FEM-based model to simulate the propagation of an acoustic wave in a large domain (relative to the wavelength) requires a minimum of 5 mesh elements per wavelength as discussed in the previous section. Simulating a 2D or a 3D case would not only require a greater computational requirement in terms of the processing speed and the storage capacity but would take a lot of time as well. Pierce, (1990) introduced the propagation of an acoustic wave in fluids with unsteady and inhomogeneous flow. Chevaugeon et al. (2005) and Kelly et al. (2018) discussed discontinuous Galerkin DG method for simulating acoustic problems and ultrasonic waves respectively. The "Convected wave equation" user interface of COMSOL simulates wave equation using DG method. The DG method uses a quartic (4^{th} order) discretization scheme which is very memory efficient when it comes to solving many millions of degrees of freedom. According to Chevaugeon et al. (2007), two to three mesh elements per wavelength can be used for modelling wave propagation. This requires a maximum element size in the mesh to be $\lambda/1.5$ and the minimum element size to be $\lambda/2$.

The Convected wave equation user interface of COMSOL, solves the linearized Euler equation also referred to as linear acoustic equation in a moving medium. The linear continuity equation (eq 2.18), momentum equation (eq 2.19) and equation of state (eq 2.20) are mentioned by Pierce (2019) as

$$\frac{\partial \rho}{\partial t} + (\bar{u}.\nabla)\rho + (u.\nabla)\rho_0 + \rho(\nabla.\bar{u}) + \rho_0(\nabla.u) = f_p \tag{2.18}$$

$$\frac{\partial u}{\partial t} + (\bar{u}.\nabla)u + (u.\nabla)\bar{u} + \frac{1}{\rho_0}\nabla p - \frac{\rho}{{\rho_0}^2}\nabla p_0 = f_v \tag{2.19}$$

$$\rho = \frac{p}{{c_0}^2} \tag{2.20}$$

where p is the acoustic pressure perturbation, u is the acoustic velocity perturbation, f_p is the monopole source, f_v is the dipole source and ρ is the acoustic wave density perturbation.

In addition, $\bar{u}$ is the background mean streamwise (in x) flow velocity, p_0 is the background mean flow total pressure, ρ_0 is the background mean flow density and c_0 is the speed of sound. In order to model the influence of background fluid flow on the propagation of the acoustic wave, these background mean flow parameters are imported from the fluid flow CFD study discussed in section 2.1.1.

Several boundary conditions have to be specified at different boundaries to simulate the propagation of the acoustic wave inside the fluid. The figure 2.4 shows the schematic of the flowmeter in 3D with two transducers clamped on to a pipe section.

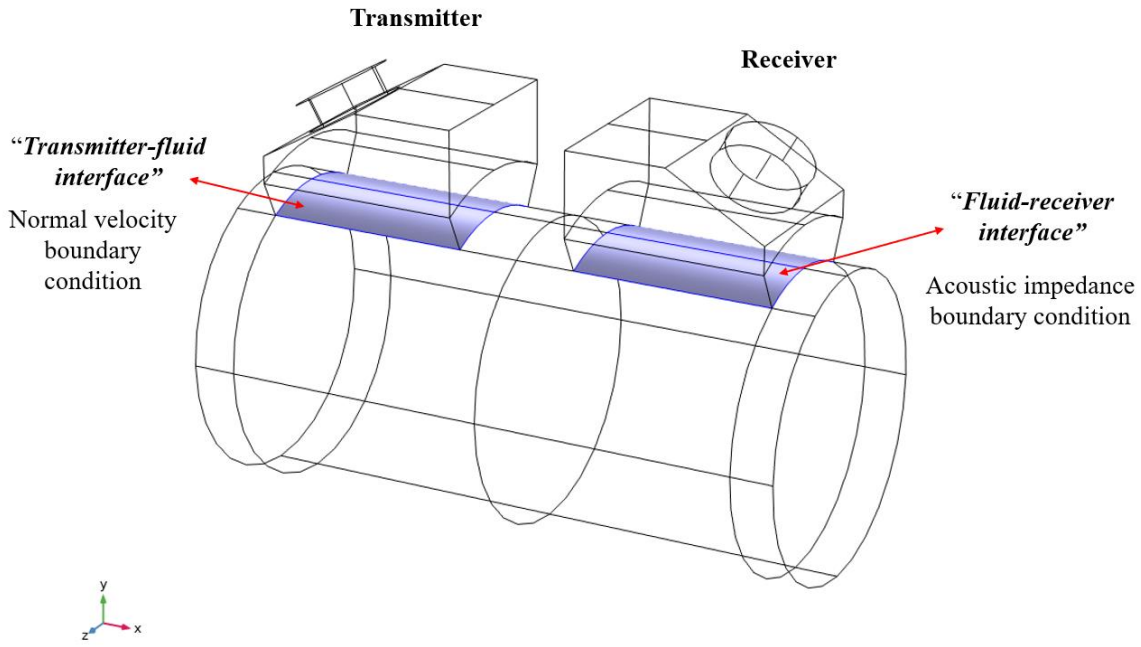

Figure 2.3 3D schematic of the flowmeter specifying an acoustic boundary condition at the highlighted interfaces (the left hand transducer as transmitter case)

These transducers act as a transmitter and a receiver interchangeably, depending upon whether the wave propagation is simulated in the direction of or opposite to the direction of the fluid flow. Considering a case where the left hand transducer acts as transmitter then the highlighted interface on the left side is specified as a "Normal velocity" boundary condition. This boundary condition acts as an external source term f_v in equation 2.19. This boundary condition specifies an inward or outward velocity. The acoustic wave generation simulated in section 2.1.3.1 is specified as a normal velocity boundary condition at the "transmitter-fluid interface" (left hand side highlighted boundary in figure 2.4). This boundary condition allows for the propagation of acoustic waves inside the fluid in the present study.

On the "fluid-receiver interface" (right hand side highlighted boundary in figure 2.4) an "acoustic impedance" boundary condition is applied. The characteristic acoustic impedance is a material property which is a measure of the resistance provided by the material to the acoustic waves (Pierce, 1990).

$$Characteristic\ Acoustic\ Impedance\ Z = \rho . c \quad (2.21)$$

where ρ is the density and c is the speed of sound of the medium in which acoustic wave is propagating. So, if the acoustic impedance of the fluid is used at the "fluid-receiver interface", then that boundary would act like a non-reflecting surface which will absorb the acoustic wave. In reality at a "fluid-receiver interface" the acoustic wave encounters a solid surface (the pipe wall) at which it will undergo refraction and propagate through the pipe wall and the receiver. In order to implement this phenomenon, acoustic impedance of the pipe wall material is specified as a boundary condition at the "fluid-receiver interface".

All of the other walls of the pipe domain are specified as the "Sound-hard wall" boundary condition by default. This boundary condition specifies that the normal component of the acoustic and background fluid velocity is zero. This condition acts like a slip boundary condition which means that the acoustic wave will be reflected completely at such a boundary. In practical scenarios, part of an acoustic wave reflects and part of it transmits through the pipe wall. This boundary condition simplifies the model by not simulating the propagation of wave inside pipe wall sections other than the one attached to the receiver.

2.1.3.3 Receiver modelling

The transducer on the receiver end is modelled using FEM. The mesh resolution is the same as that described in section 2.1.3.1. The phenomenon of direct piezoelectricity is observed in the receiver where the mechanical strain is converted into an electrical potential. In the previous study, the propagation of the acoustic wave was simulated inside the fluid, the wave being generated at the location of the transmitter and ending at the location of the receiver. The pressure component of the acoustic wave causes a mechanical strain in the receiver. The process and relations prescribed in the piezoelectric modelling (section 2.1.2) are followed when simulating transient behaviour of the receiver.

A "boundary load" boundary condition is applied at the "fluid-receiver interface". This boundary condition is used to apply a load at the specified boundary. Under this boundary condition, force or pressure can be specified as a function of time. The acoustic pressure (of the acoustic wave simulated in the previous study) is specified as the input pressure in

the “boundary load” boundary condition. The mechanical strain generated due to this boundary condition is finally converted into electrical potential at the piezoelectric disc. A point probe (monitored location in the simulation) at the centre of the disc provides a plot of floating potential developed in the disc which varies with time. This plot is described as the received signal.

All of the above-mentioned steps used to conduct this numerical study, provide a received signal. These steps are repeated by switching the transmitter and receiver so that the ultrasonic wave propagates in the opposite direction of the fluid flow producing another received signal. These two received signals are then cross correlated to compute the time difference “Δt” between the signals as shown in the figure 2.4.

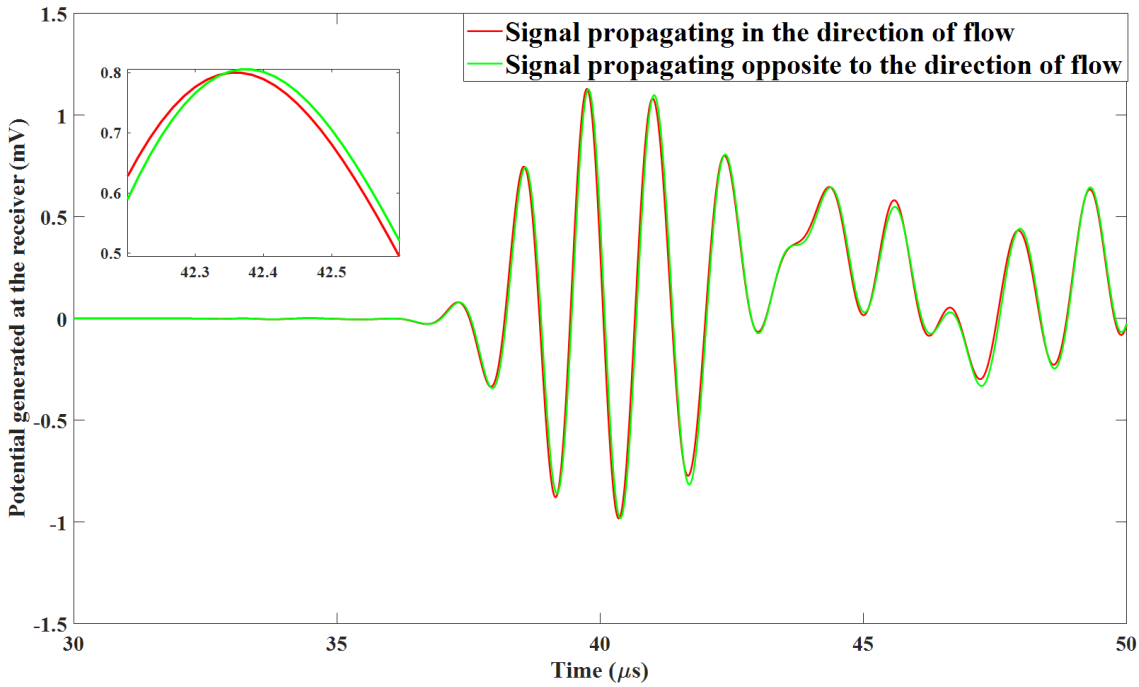

Figure 2.4 Received signals from the numerical simulation for the straight pipe case

In the figure 2.4, the green signal lags the red signal which is expected because the signal which propagates in the opposite direction of the flow (green) will take more time compared to the signal moving in the direction of the flow (red). The time difference between the received signals shown in the figure 2.4 is 25ns. Using the equations 1.18 and 1.19, the flowrate of 1.968 m^3/hr is estimated from the received signals (shown in figure

4.2 with $\Delta t = 25\ ns$). This estimated flowrate can be compared with the flowrate given in the boundary condition of the simulation to determine the validity of the entire numerical method adopted to simulate the working of a clamp-on ultrasonic flowmeter.

According to section 2.1.1, the fluid flow inside the pipe is simulated where the "Inlet" boundary condition is specified. At the inlet of the numerical domain, fluid velocity is defined which is the bulk fluid velocity (which corresponds to a flowrate). The straight pipe domain (shown in figure 2.5) was simulated at a flowrate of $2\ m^3/hr$. The percentage error between the estimated flowrate and the flowrate given as a boundary condition for the straight pipe section is 1.6%. This leads to a conclusion that the entire numerical technique followed to model the working of a clamp-on ultrasonic flowmeter is working correctly.

2.1.4 Numerical model parameters

Two numerical domains for fluid flow are defined which are

1. Clamp-on ultrasonic flowmeter onto a straight pipe section. (figure 2.5)
2. Straight pipe section with a 90^0 elbow where a clamp-on ultrasonic flowmeter is installed downstream of the elbow. (figure 2.6)

Below are the figures of these numerical domains.

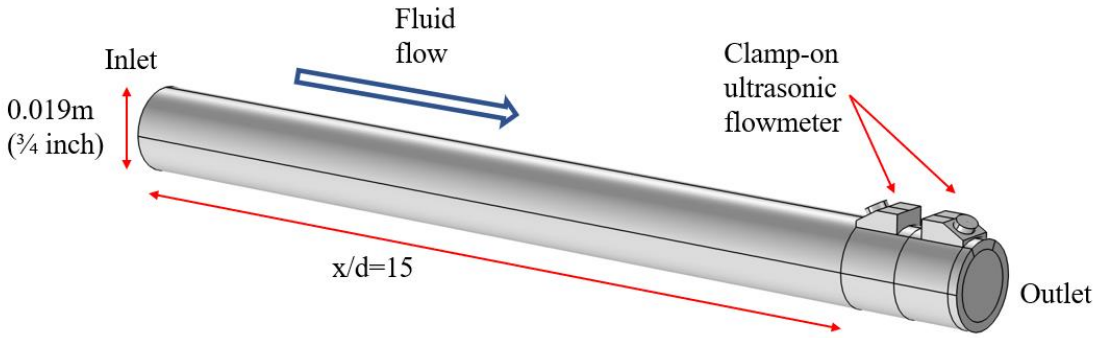

Figure 2.5 Straight pipe section numerical domain

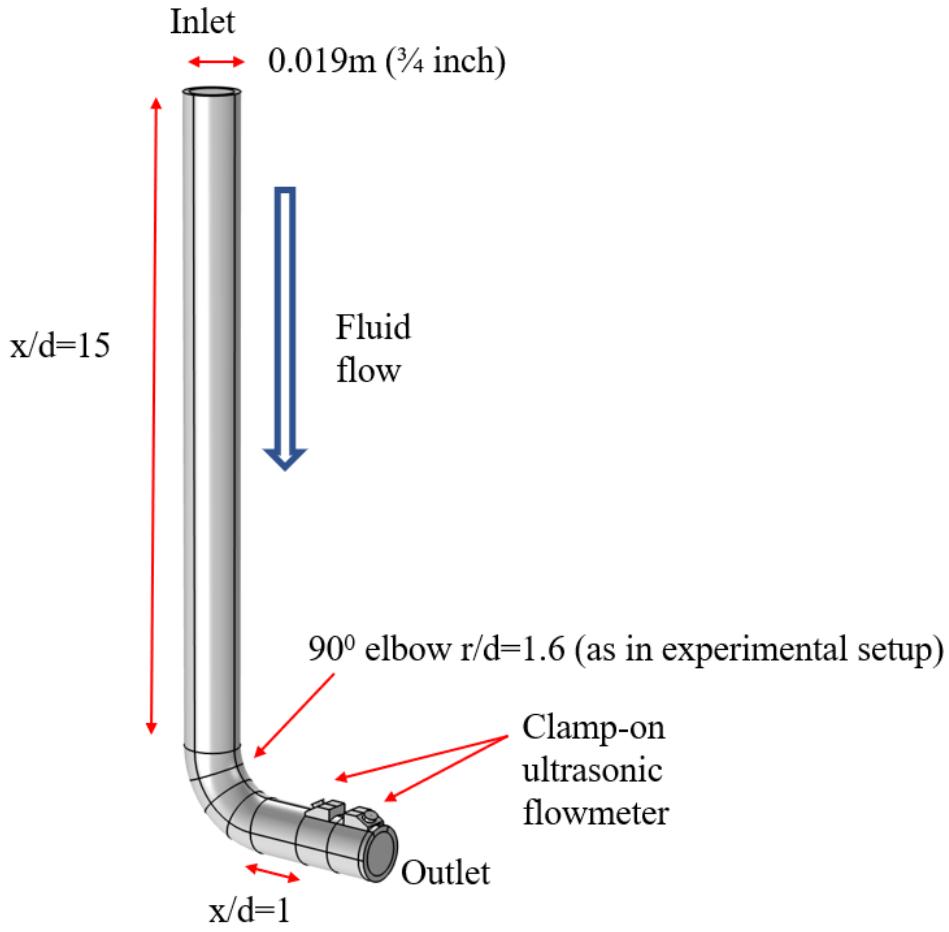

Figure 2.6 Straight pipe with elbow numerical domain

Following the procedure described in section 2.1.3, the velocity estimated by the ultrasonic signals is computed in COMSOL. This velocity can be compared with the velocity entered as the boundary condition at the inlet of the pipe. This comparison determines the accuracy of the entire numerical modelling process. The numerical domain with a straight pipe section is used for this purpose. The numerical domain (pipe with an elbow) is used to observe the uncertainty in the flow velocity induced by a 90^0 elbow when the clamp-on flowmeter is installed at x/d=1 downstream of the elbow. As shown in figure 1.23 (*In-situ* flowmeter installation locations), it can be assumed that even in a confined installation location, a minimum of downstream length x/d=1 after a 90^0 elbow would be available. As discussed in section 1.2.1, at x/d=1 the effect of secondary flow generated due to a 90^0 elbow are dominant compared to the secondary flow further away from the elbow outlet. So, this location is practically available for the meter installation and contains the secondary flow which effects the uncertainty in the readings of these flowmeters.

Many pipe sizes are used in industrial and residential setups to supply water and other fluids. According to Vandervort (2021) 0.019m (¾ inch) diameter stainless steel pipe is commonly used for water supply in households. A pipe of (¾ inch) diameter is used in the numerical and experimental study.

The dimensions of the clamp-on ultrasonic flowmeter's numerical model are depicted in the figure 2.7. The dimensions of the transducers of the physical clamp-on ultrasonic flowmeter used in the experimental study are unknown. The dimensions of the transducers in the figure 2.7 are approximate assumptions to keep the numerical domain small enough which requires minimum computational resource. On the other hand the size of both transducers can be reduced to a limit above which the received ultrasonic signal at the receiver is detectable.

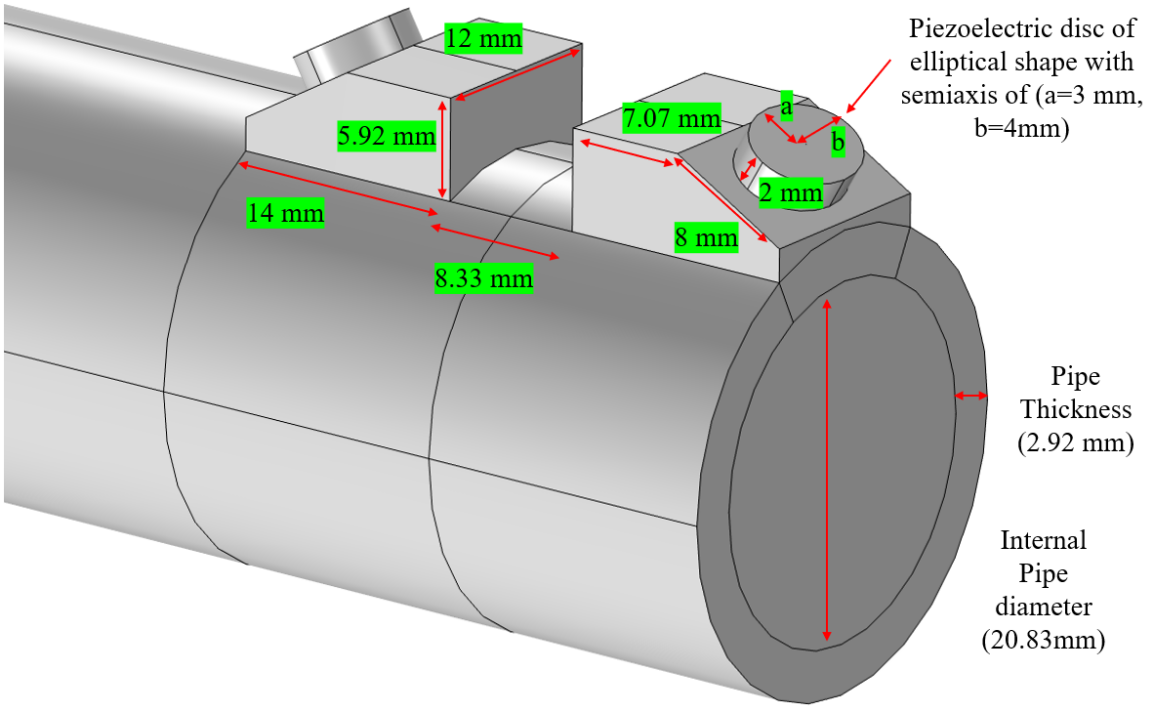

Figure 2.7 Dimensions of numerical domain consisting of pipe and transducers of clamp-on ultrasonic flowmeter

A structured grid is created on the numerical domain of the pipe because of its better element quality compared to hybrid or unstructured grids. Such a grid has quadrilateral shaped cells in 2D and hexahedral shaped cells in 3D. An unstructured grid is generated on the transducers of clamp-on flowmeter due to the shape of the transducer. Such a grid has triangular shaped cells in 2D and tetrahedron shaped cells in 3D. A hybrid grid contains a mix of structured and unstructured portions.

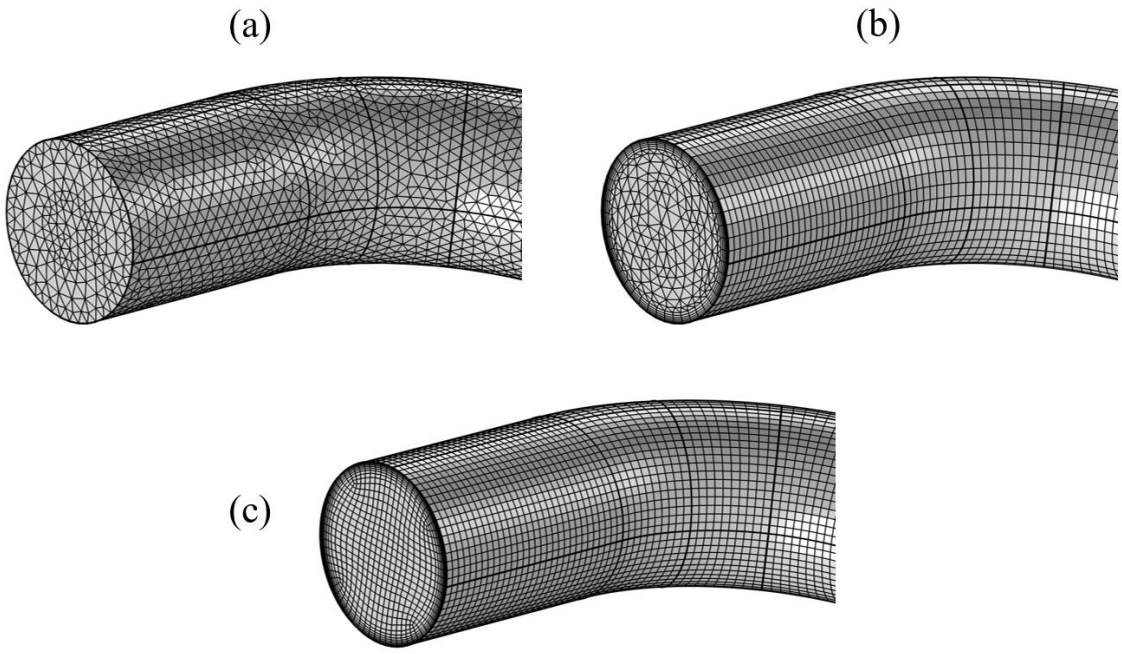

Figure 2.8 (a) Unstructured grid, (b) Hybrid grid, (c) Structured grid

For a fluid flow simulation in a pipe, the boundary layer near the wall of the pipe needs to be resolved by the mesh. An unstructured grid like (a) in the figure 2.8 has large tetrahedral cells along the pipe wall which are unable to resolve the boundary layer. In order to get fine cells near the wall of the pipe, a hybrid grid can be generated as shown in the figure 2.8 (b). In a hybrid grid, a layer of hexahedron cells is generated near the walls to resolve the boundary layer whereas triangular prism cells are generated away from the wall. For this numerical study, a structured grid is chosen over the hybrid grid because for the same number of cells in the domain the element quality for a structured grid is better than the hybrid grid as shown in table 2.2. The table 2.2 shows the type of cells and the element quality where 0 is the worst element quality and 1 is the best element quality.

Table 2.2 Comparison of the element quality between a randomly generated hybrid and a structured grid generated for the pipe and elbow case

	Structured grid	**Hybrid grid**
No. of hexahedron cells	435,744	97,920
No. of triangular prism cells	-	3,389,980

No. of total cells	435,744	436,900
Minimum element quality	0.5996	0.2566
Average element quality	0.9218	0.7976

The mesh resolution and the boundary conditions for modelling of the ultrasonic waves is discussed in the section 2.1.3. The boundary conditions for the fluid flow modelling are discussed here. The inlet and the outlet of the numerical domains (depicted in figure 2.5 and 2.6) are specified as the "velocity inlet" and the "pressure outlet" respectively. All the other walls of the fluid domain are specified as the "no-slip" boundary condition.

The solutions are considered to be converged when the residuals for the continuity equation, momentum equation and turbulent parameters ($k\ and\ \omega$) are reduced to 10^{-3}, 10^{-5} and 10^{-5} respectively. To consider a solution as converged the parameters of interest (like the streamwise velocity profile and the turbulence intensity profile) in the domain should be consistent with reducing the residual. To validate this, a simulation was run for the residual reduction of 10^{-3} and 10^{-5}. The axial velocity profiles and the turbulence intensity profiles at the outlet of the elbow obtained from these two simulations (one with residual reduction of 10^{-3} and second with residual reduction of 10^{-5}) are compared in the figure 2.9.

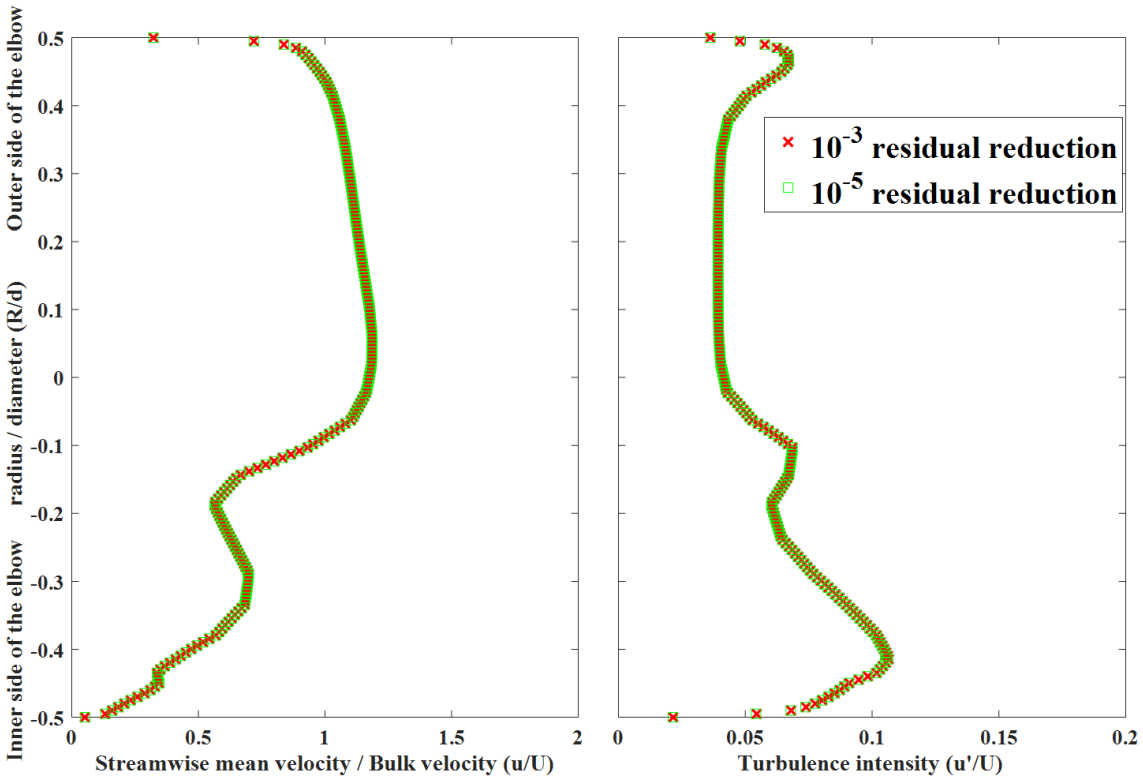

Figure 2.9 Normalized streamwise velocity and turbulence intensity profiles at the elbow outlet for the residual reduction of 10^{-3} and 10^{-5} at the Re = 33843

The root mean square (rms) for the streamwise velocity profile is 1.46×10^{-4}. The rms for the turbulence intensity profile is 4.55×10^{-4}. This study depicts that the change in streamwise velocity profile and the turbulence intensity profile at the elbow outlet is negligible when the residual is reduced from 10^{-3} to 10^{-5}.

2.1.5 Grid independence study

This study is conducted by generating 4 different structured grids. The details of the grids are mentioned in the table 2.3.

Table 2.3 Details of different grids generated for the pipe and elbow case

	M1	**M2**	**M3**	**M4**
No. of total cells	225,250	452,352	911,680	1,806,870
Minimum element quality	0.496	0.596	0.585	0.642
Average element quality	0.9069	0.9245	0.9269	0.9243
Average simulation time	0.88 hours	2 hours	6.5 hours	16 hours

The coarsest mesh (M1) was refined to generate fine meshes (M2, M3 and M4) by increasing the number of cells in the cross-section and in the axial direction of the pipe-elbow domain shown in figure 2.5. The axial velocity profiles and the turbulence intensity profiles at the elbow outlet are plotted for all the grids in the figure 2.10 below.

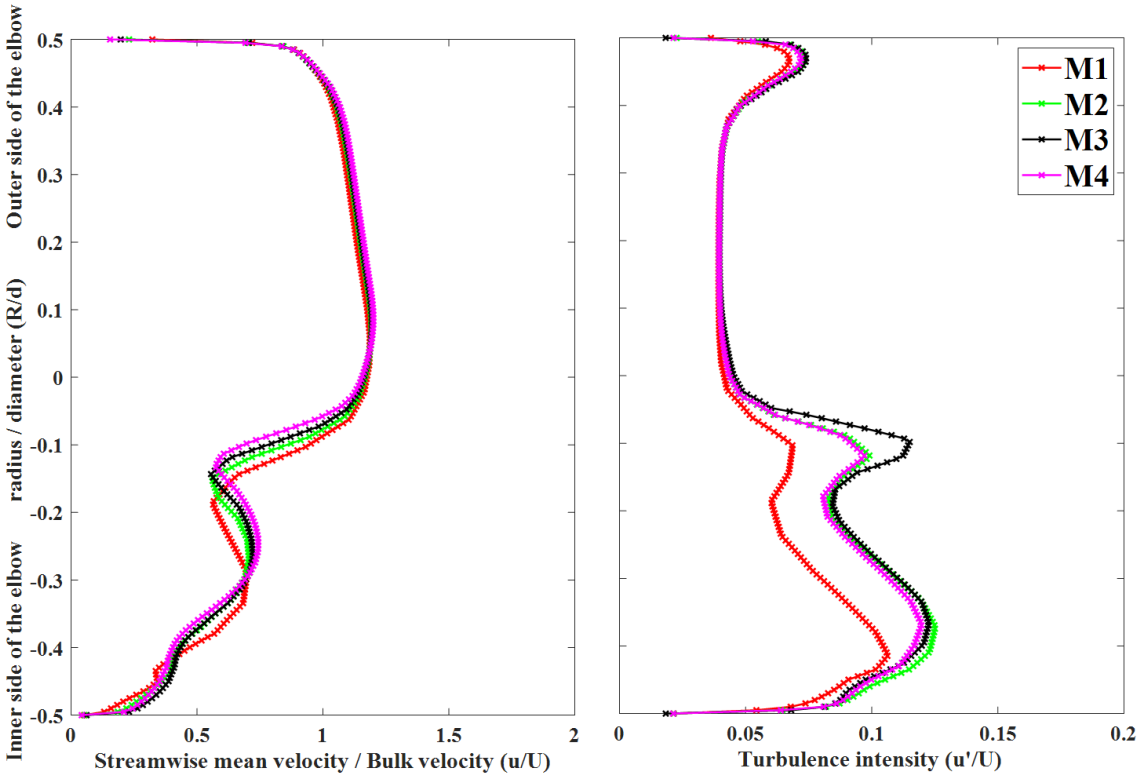

Figure 2.10 Normalized axial velocity and Turbulence Intensity at the elbow outlet for different grids at Re = 33843

For the comparison between the grids, rms is calculated between each grid which is shown in table 2.4 below.

Table 2.4 RMS of data points between different grids

	Normalized axial velocity profile	**Turbulence intensity profile**
RMS (M2-M1)	0.0406	0.0158
RMS (M3-M2)	0.0281	0.0051
RMS (M4-M3)	0.0294	0.0055

The lowest RMS is between the data points of grids M3 and M2. The percentage difference between the RMS (M3-M2) and RMS (M4-M3) for the normalized axial velocity profile

is 4.52%. Similarly, the percentage difference between the RMS (M3-M2) and RMS (M4-M3) for the turbulent intensity profile is 7.55%.

Considering the average simulation time (as mentioned in table 2.3) taken by the grids, further refinement of the grid M4 is not simulated. The grid (M2) can be selected for further numerical analysis as it is estimating the velocity profile and the turbulence intensity profile within 4.52% and 7.55% respectively compared to the finest grid M4. Furthermore, the grid M2 takes considerably less computational time compared to grid M4. The ultrasonic wave propagation time scale is much smaller than turbulent time scale that a variation of normalized velocity profiles and turbulence intensity profiles between the grids M2, M3 and M4 do not affect the ultrasonic wave propagation.

2.1.6 Validation of the fluid flow simulation

The reasons for choosing the RANS approach over the LES for the current study are as follows:

- According to the section 1.2.1, adverse pressure gradients or flow separation in the fluid domain is not expected if the r/d of the pipe-elbow setup is greater than 1.
- Limitation of running LES using COMSOL's GUI interface at compute Canada.
- The time scale of the ultrasonic waves propagating inside the fluid is in nano seconds which is much smaller than Kolmogorov's scales in the fluid.

Due to these reasons the RANS approach is used for the numerical study in this thesis.

Below the figure 2.11, draws a comparison between the published data with the RANS approach. The $k-\omega$ and the $SST\ k-\omega$ turbulence models are used to simulate 3 numerical domains with r/d of 1, 1.58 and 2 (literature is available for these 3 r/d) and the normalized velocity profiles are plotted at the elbow outlet. The published LES or experimental (PIV) data presented by Ikarashi et al. (2018), Röhrig et al. (2015), Tan et al. (2014) and Tanaka et al. (2009).

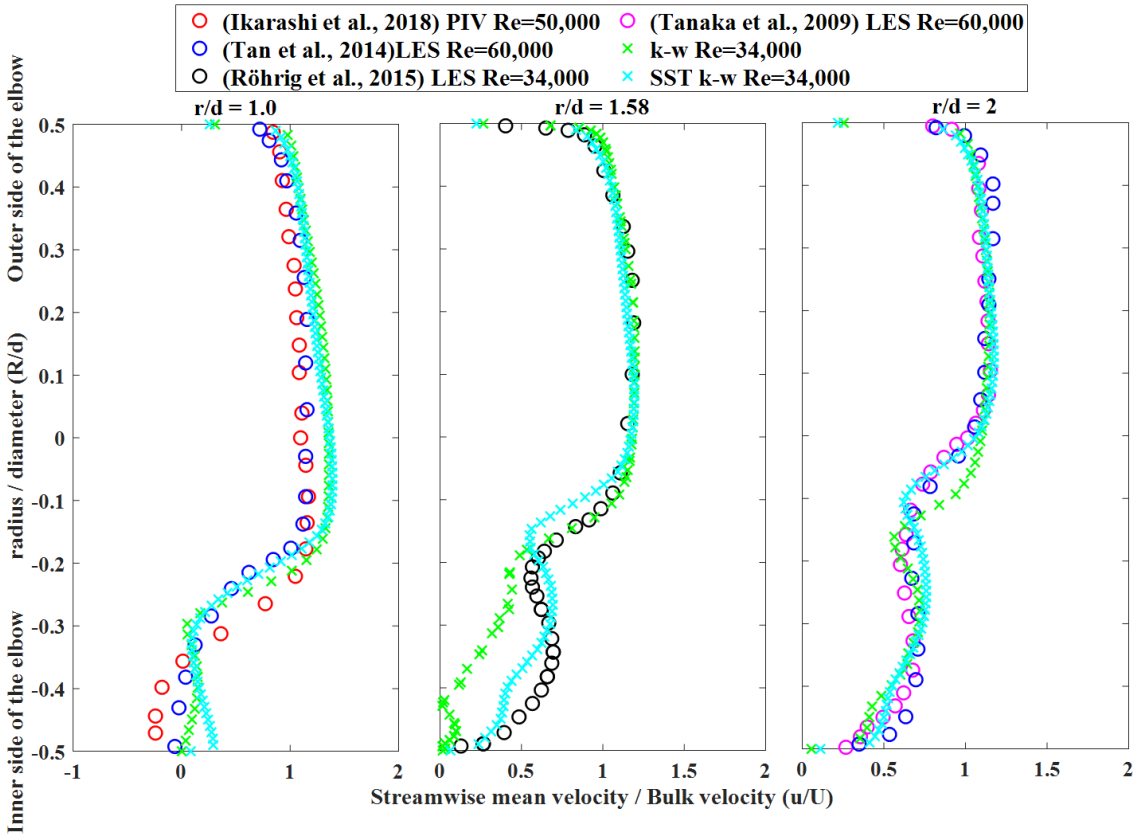

Figure 2.11 Comparison of RANS with published data showing normalized streamwise velocity profiles at the elbow outlet for elbows of different r/d

For r/d = 1 (Left plot in figure 2.11), the experimental and the LES data (red and blue curve) suggests reverse flow close to the inner side of the elbow. However, the data computed through the RANS equations using the $k-\omega$ and the $SST\ k-\omega$ turbulence models (green and cyan curves) is close to LES data but do not depict any reverse flow. For r/d =1.58, the flow profiles computed via RANS equations closely follow the LES data but near the inner side of the elbow the $SST\ k-\omega$ predicts better than the $k-\omega$. For r/d = 2, the RANS equations data closely matches the LES data. It is expected that the data obtained from RANS equations will deviate from the LES data as it does not resolve all the scales of turbulence. From the figure 2.10, for the r/d=1.58 (which is close to the r/d used in this thesis) the $SST\ k-\omega$ predicts better than the $k-\omega$ turbulence model. For this reason and the benefits of the $SST\ k-\omega$ mentioned in the table 2.1, the $SST\ k-\omega$ model is used in this thesis.

2.2 Summary

This chapter discussed the numerical approach adopted to simulate the working of a clamp-on ultrasonic flowmeter in the presence of a background fluid flow. The numerical equations, boundary conditions, convergence criteria, mesh generation and grid independence are discussed in this regard. The next chapter focusses on the details of experimental methodology adopted in this thesis.

Chapter 3

3 Experimental Methodology

A flow rig is used to conduct experiments, details of which are discussed in this chapter.

3.1 Flow rig

The experimental setup used in the present study is designed and developed in the Department of Mechanical and Materials Engineering of University of Western Ontario by Dudalski (2020). The figure 3.1 shows the schematic of the flow rig which consists of Pipe, elbow, valve, pump, reservoir and flowmeters. As mentioned in the section 2.1.4, 0.019m (¾ inch) diameter pipe is used in the flow rig. The schematic of the setup is shown in the figure 3.1.

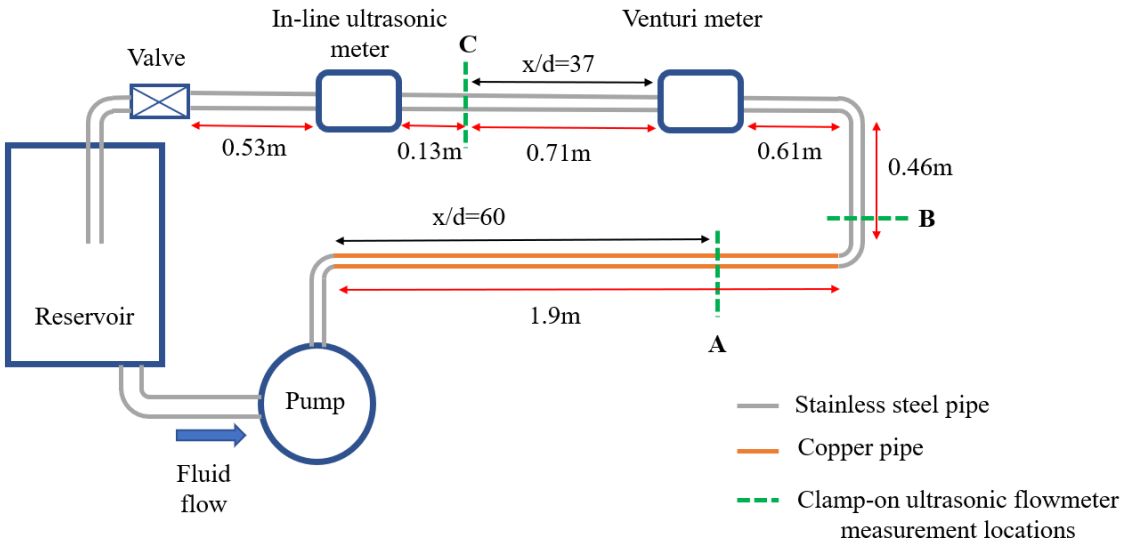

Figure 3.1 Schematic of the flow rig

A copper pipe is installed at one location (as shown in the figure 3.1) while all other pipes and elbows are Stainless steel 316. The fluid used in the flow rig is water at room temperature. The stainless-steel pipes are used to prevent rust. The reservoir has a capacity of 70 litres. The Venturi and the In-line ultrasonic flowmeters are used for reference measurements installed at the locations depicted in the figure 3.1. The location of the test

flowmeters (clamp-on ultrasonic) is indicated by the locations A, B and C in the figure 3.1. As mentioned in the section 1.4, the effect of a 90^0 elbow on the flow measurement by a clamp-on ultrasonic flowmeter is determined by installing it at the location B (which is at x/d=1 downstream of the elbow outlet). The location A and C are used to investigate the performance of the test meters in a uniform flow conditions. At the location A and C, the upstream straight pipe lengths are x/d = 60 and x/d = 37 respectively. As discussed in the section 1.2.6.3, the effects of pipe disturbances on the fluid flow at these locations are minimum.

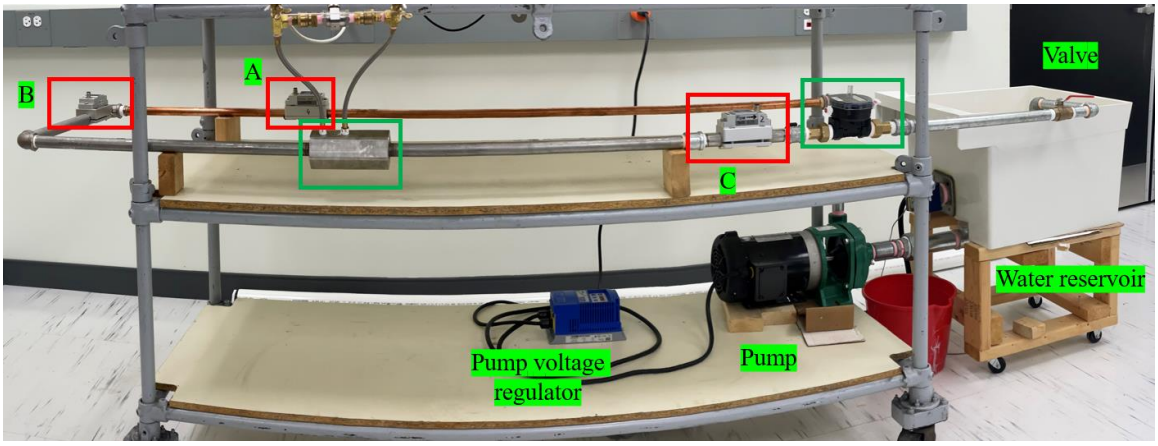

Figure 3.2 Experimental setup in the laboratory

The figures 3.1 and 3.2 can be correlated to understand the setup. In the figure 3.2, red boxes highlight the test flowmeters (clamp-on ultrasonic) and the green boxes show the reference (venturi and the in-line ultrasonic) flowmeters.

3.2 Reference meters

Two flowmeters are used for reference measurements which are discussed below.

3.2.1 Venturi flowmeter

These meters are categorized as differential pressure-based flowmeters (also described in section 1.2.2.2). The volume flowrate is estimated by the equation 3.1.

$$Q = \frac{C}{\sqrt{1-\beta^4}} \frac{\pi d^2}{4} \sqrt{\frac{2\Delta P}{\rho}} \tag{3.1}$$

where ΔP is the pressure differential, ρ is the fluid density (corresponding to fluid's room temperature), d_t is the throat diameter, d is the internal pipe diameter, β is the diameter ratio (d_t/d) and C is the coefficient of discharge according to the Standards (2003). The discharge coefficient "C" depends on Reynolds number "Re_D" and β which is tabulated in the tables A.1-A.3 in the Standards, (2003).

In order to determine ΔP, the differential pressure sensor is connected across the two taps of the venturi as shown in the figure 3.3. The manufacturer of the differential pressure sensor Omega (2019) states the accuracy of 0.08% full scale. The sensor with model no. PX409-10WDWU5V has a differential pressure range of $0 - 25mBar$ which is why it has been used for the flowrate range of $0 - 0.6\ m^3/hr$. The pressure sensor with the model no. PX409-005DWU5V has a differential pressure range of $0 - 350mBar$ and it has been used for a flowrate range of $0.7 - 2.5\ m^3/hr$. Both of these sensors have an output voltage range of $0 - 5\ Vdc$.

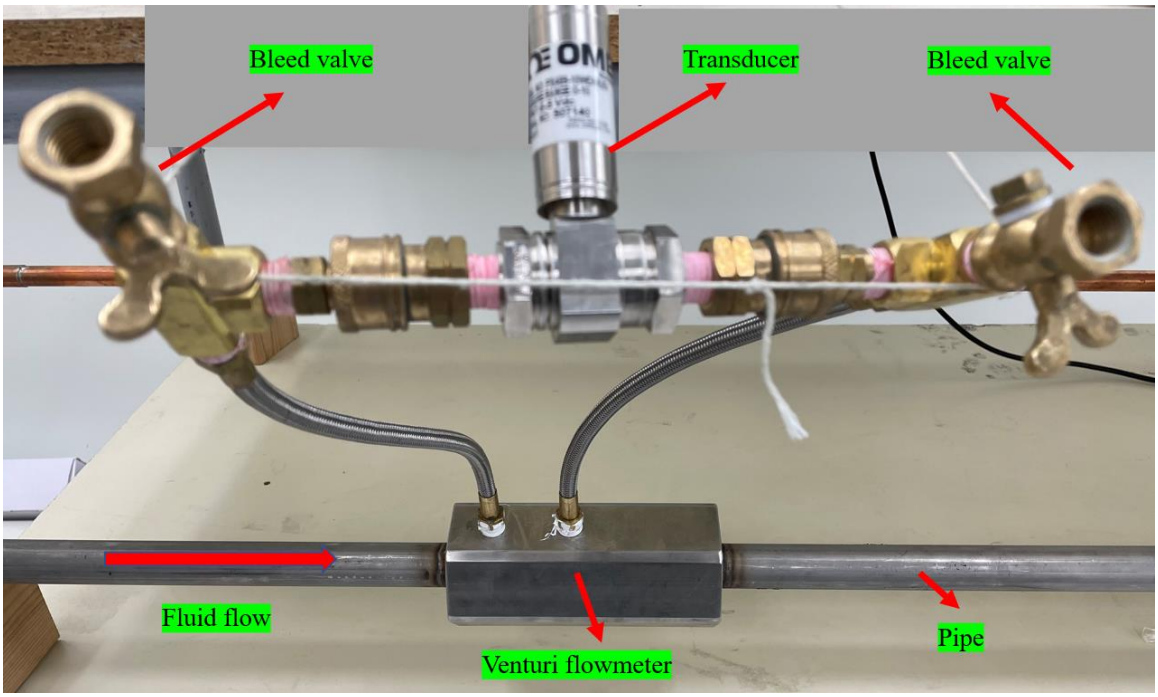

Figure 3.3 Venturi flowmeter with a differential pressure sensor

These differential pressure sensors are connected with a data acquisition (DAQ) device manufactured by Computing, (2019). The data is collected from the differential pressure sensor. The voltage data from the DAQ are averaged over a time of 5sec (as mentioned in section 3.4). The minimum and maximum output voltages of the sensors (0-5Vdc) correspond to the respective differential pressure ranges of the sensors (0-25mBar and 0-350mBar). Due to this direct correspondence between the output voltage and the differential pressure, the average differential pressure is estimated at each flowrate. The equation 3.1 is used to convert this average differential pressure into a flowrate.

The uncertainty in the readings measured by the venturi flowmeter including the differential pressure sensor has been tabulated by Dudalski (2020) at various flowrates. The average uncertainty as a percentage of reading value for the flowrate range of $0.3 - 2.5\ m^3/hr$ is 0.6%. A bucket test was performed at flowrates between $0.3 - 2.5\ m^3/hr$ and the results were compared with the venturi flowmeter's readings. The measurement uncertainty in the venturi flowmeter is an average of $\pm 1.1\%$ for the flowrate range of $0.3 - 2.0\ m^3/hr$ and $\pm 4.6\%$ for the flowrate range of $2.0 - 2.5\ m^3/hr$.

3.2.2 In-line ultrasonic flowmeter

An in-line ultrasonic flowmeter (B6 LiteVW) is used alongside the venturi flowmeter as a secondary reference measurement which is manufactured by Bove (2020) as shown in the figure 3.4. The flowrate range stated by the manufacturer for this flowmeter is $0.016 - 3.125\ m^3/hr$. The manufacturer has stated this ultrasonic flowmeter as class 2 which have an uncertainty in the flowrate of $\pm 5\%$ according to Internationale (2006). This flowmeter has no digital or analog output signal which can be recorded using the DAQ. In chapter 4, the readings taken by the clamp-on ultrasonic flowmeters and in-line ultrasonic flowmeter are compared with the venturi flowmeter readings. According to the experimental data shown in chapter 4, in-line ultrasonic flowmeter measures flowrate lower than the venturi flowmeter where the readings taken by the in-line ultrasonic flowmeter are within 6% of the venturi flowmeter readings.

Figure 3.4 In-line ultrasonic flowmeter used in the experimental setup

3.3 Test flowmeter

3.3.1 Clamp-on ultrasonic flowmeter

A total of 5 clamp-on ultrasonic flowmeters (FHM500 flow watch) are used as test flowmeters at locations A, B and C depicted in the figures 3.1 and 3.2. The flowrate range of this flowmeter is $0.13 - 6.13\ m^3/hr$ as mentioned by the manufacturer. According to Sentec, (2021) (the manufacturer) the uncertainty in the measurement is 2% (The manufacturer has not mentioned weather the uncertainty is of full scale or reading value). Figure 3.5 shows the clamp-on ultrasonic flowmeter used in the experimental study.

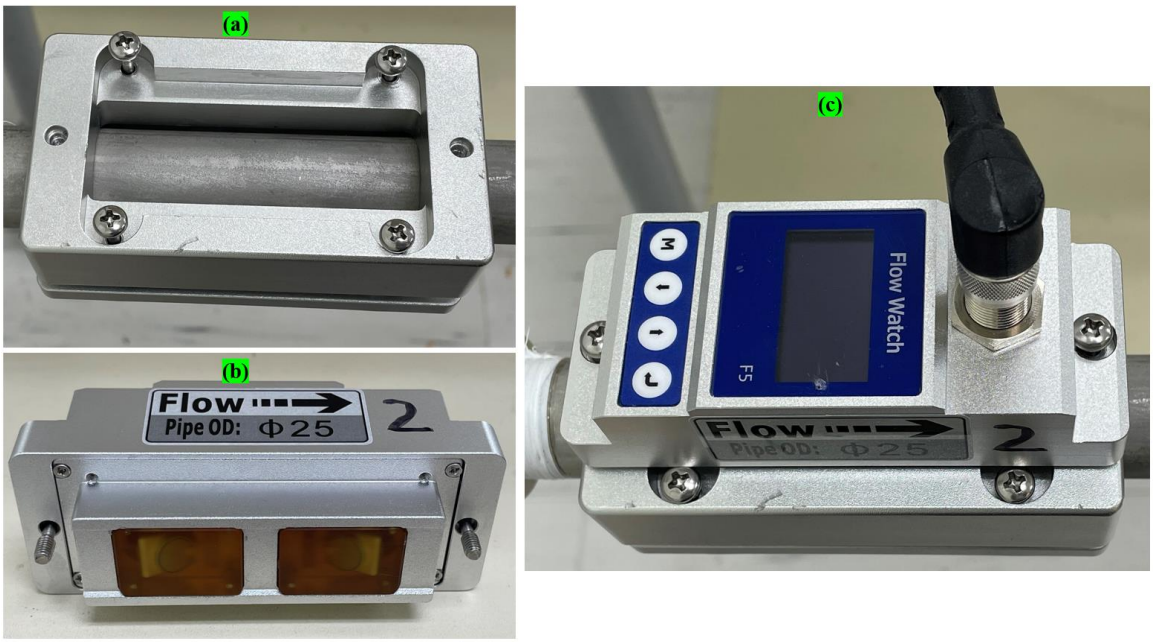

Figure 3.5 Clamp-on ultrasonic flowmeter (a) Clamping mount, (b) Side view showing the Transducers, (c) Top view showing the flowmeter clamped onto the pipe

The flowmeter has a "$4-20mA$" analog output. According to this output signal, 4mA corresponds to the flowrate of $0\,m^3/hr$ and 20mA corresponds to the flowrate of $10\,m^3/hr$. Due to this correspondence between the analog signal and the flowrate, the analog output signal stays between the $4mA-20mA$ range for the operating flowrate range ($0.13-6.13\,m^3/hr$) of this clamp-on ultrasonic flowmeter. According to the manufacturer any resistor less than 600 Ω can be used with the $4-20mA$ analog output of the clamp-on ultrasonic flowmeter (Sentec, 2021). A resistor of 237Ω (so that the current in the loop stays between $4-20mA$ range) is installed in series with the analog output (of the clamp-on ultrasonic flowmeter) in the DAQ which records the voltage drop across this resistor. This resistor creates a voltage range of $0.948-4.74V$ corresponding to the $4-20mA$ analog output. The uncertainty of the DAQ as a percentage of reading value is 0.2% according to Computing, (2019). The equation of a straight line is used to convert the voltage into the flowrate because they have a linear relation with each other.

$$f_{clamp-on} = (m \times V_{4-20mA}) + const \tag{3.2}$$

$$m = \frac{10-0\ (m^3/hr)}{(20mA \times 237\Omega)-(4mA \times 237\Omega)} \tag{3.3}$$

$$const = (10\ m^3/hr) - (m \times 20mA) \tag{3.4}$$

The sampled voltage data are averaged and equation 3.2 is used to convert the averaged voltage into the corresponding flowrate. The next section discusses the sampling time.

3.4 Sampling of the data in DAQ

A statistical averaging of the sampled data from the DAQ is performed to estimate the sample time for which the data reaches a steady state. Figure 3.6 shows the statistical average over time of the data obtained from the venturi and clamp-on ultrasonic flowmeter which is recorded by the DAQ. The data are recorded at the lowest and the highest flowrate to estimate the sample time for which the data reaches steady state.

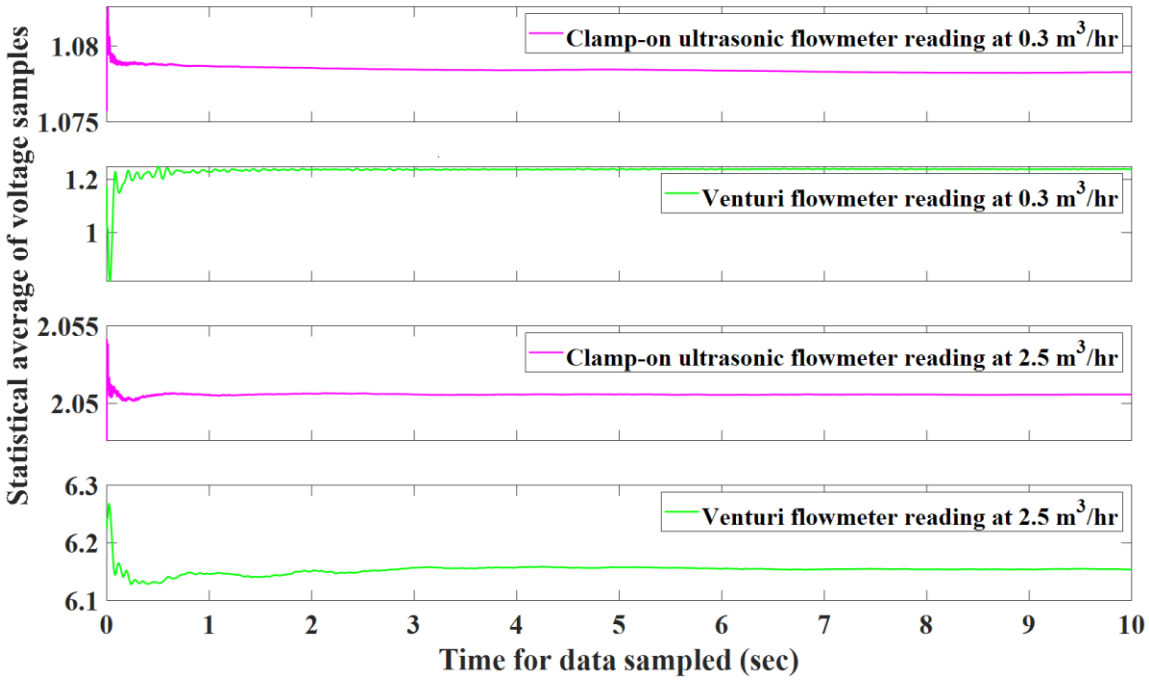

Figure 3.6 Statistical averaging of the sampled data (for 10 sec) from the venturi and clamp-on ultrasonic flowmeter at the lowest and the highest flowrate

From the figure 3.6, at both flowrates the data from both of the flowmeters reaches a steady state after 5 sec when the data reaches within $\pm 0.1\%$ over time. This is the selected sampling time for the flowmeters operating in the flowrate range of $0.3 - 2.5\ m^3/hr$.

3.5 Summary

The experimental procedure adopted in this thesis is discussed in this chapter. The schematic of the flow rig is discussed followed by the details of the reference and the test flowmeters. The data acquisition technique for the venturi and clamp-on ultrasonic flowmeters is discussed. The uncertainty in the measurements associated with the venturi, in-line ultrasonic flowmeter and the DAQ device are 0.6%, ±5% and 0.08% respectively. The results obtained from the numerical and experimental setups are discussed in the next chapter.

Chapter 4

4 Results and discussion

The results obtained through the numerical and experimental procedures discussed in the previous chapters are presented here. A comparison between the results is also conducted. As the numerical methodology was discussed earlier than experimental, so the numerical results are discussed first in this chapter.

4.1 Numerical results

4.1.1.1 Straight pipe case vs pipe with 90^0 elbow case

The numerical method used to simulate the phenomenon of a clamp-on ultrasonic flowmeter has been described in chapter 2. The numerical simulation is conducted on a straight pipe whose numerical domain is shown in figure 2.5 and a pipe with an elbow whose numerical domain is shown in figure 2.6. Figure 4.1 shows the propagation of the ultrasonic signal inside the fluid at different time instances. These time instances are randomly chosen to depict the propagation of the ultrasonic wave inside the fluid.

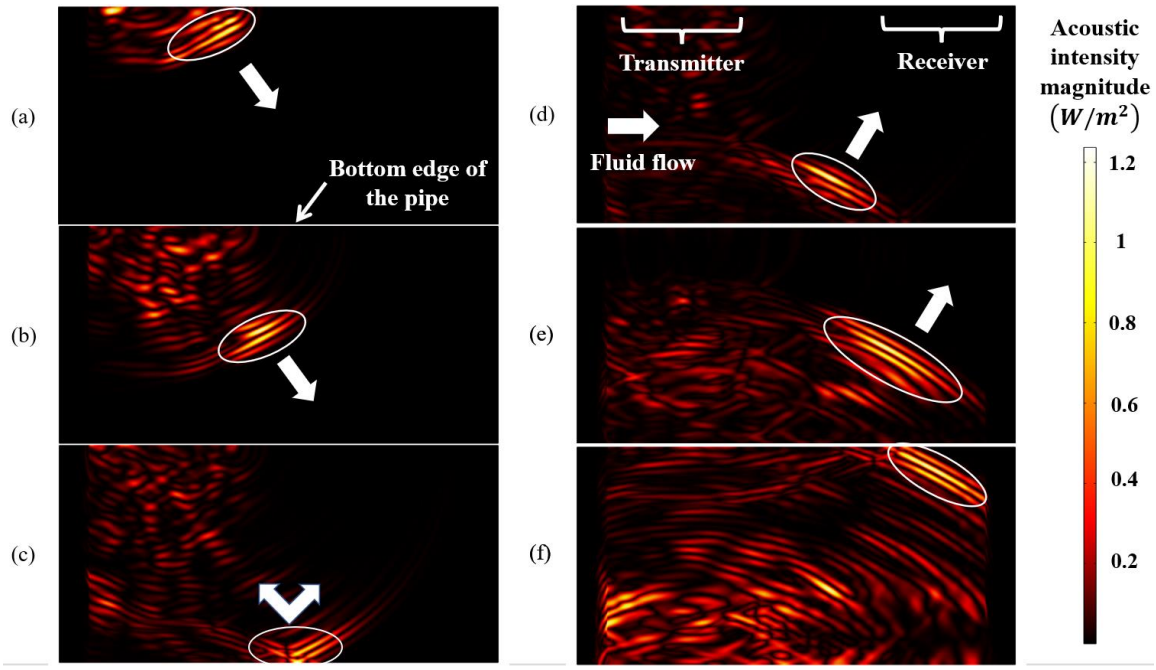

Figure 4.1 Depiction of ultrasonic signal propagation inside the fluid for the straight pipe case at different time instances (a) $7\mu s$, (b) $13\mu s$, (c) $20\mu s$, (d) $23\mu s$, (e) $28\mu s$ and (f) $35\mu s$

The ultrasonic wave generated by the transmitter (location shown in figure 4.1 (d)), propagates inside the fluid and is reflected from the bottom of the pipe wall (as shown in figure 4.1 (c)). The fluid flow is from left to right as shown in figure 4.1 (d). Figure 4.1 (f) shows the instance just before the ultrasonic wave reaches the receiver. The structure of the fluid flow that this ultrasonic wave encounters while propagating from transmitter to the receiver effects the time taken by the ultrasonic wave to travel inside the fluid. The fluid flow inside and downstream of the elbow is discussed further to understand the structure of the fluid flow which effects the propagation of the ultrasonic wave.

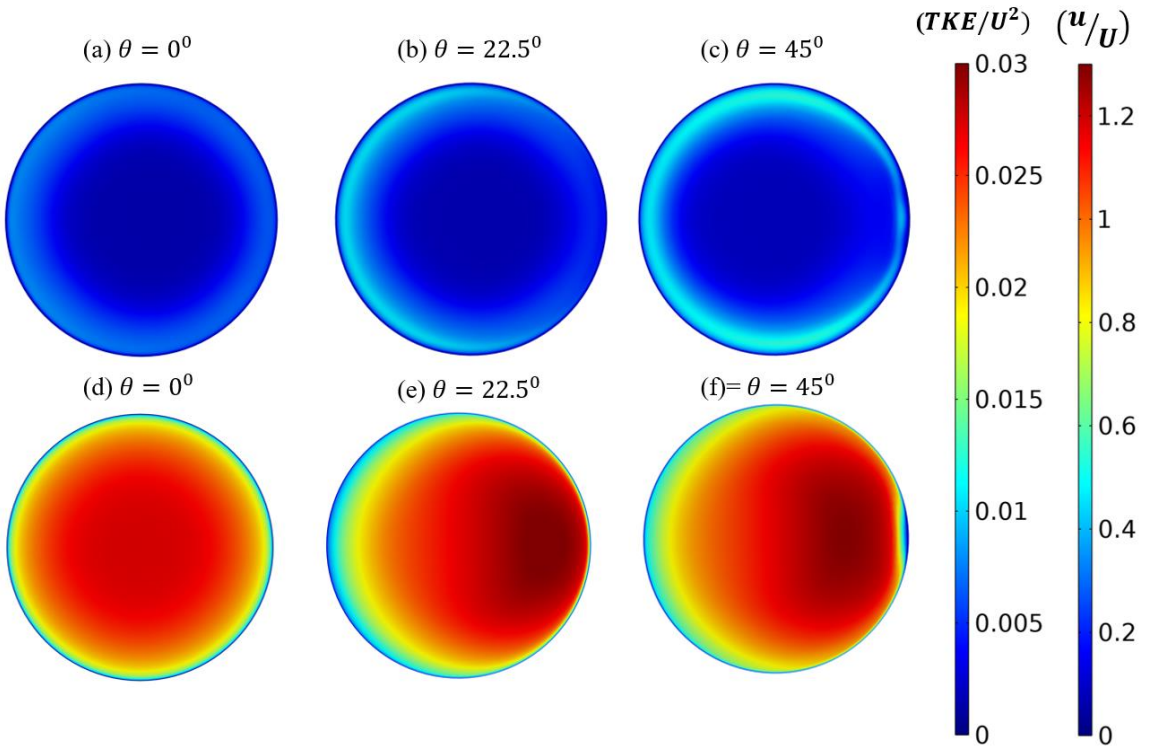

Figure 4.2 In-plane contours of normalized TKE and normalized streamwise velocity in first half of the elbow (a), (b), (c) are normalized TKE and (d), (e), (f) are normalized streamwise velocity

In figure 4.2 (a), (d) show the TKE and normalized velocity contours at the inlet of the elbow. The TKE is generated close to the walls as seen in figure 4.2 (a) light blue colour. In figure 4.2 (b), (e) show the TKE and normalized velocity contour inside the elbow at $\theta = 22.5^0$. The secondary flow due to the curvature of the elbow is generated and the TKE on the outer side of the elbow (left hand side in figure 4.2 (b)) is higher than anywhere else in the plane. The mean shear between the high and low velocity region on the outer side of the elbow (as shown in figure 4.2 (e) and (f) left hand side) causes the generation of TKE. The low velocity region is created on the outer side of the elbow (left hand side in figure 4.2 (e)) whereas a high velocity region is on the inner side of the elbow (right hand side in figure 4.2 (e)). At $\theta = 45^0$, the TKE is further increased all around the walls with a slight increase on the inner side of the elbow (right hand side in figure 4.2 (c)). The low velocity region has appeared on the inner side of the elbow (right hand side in figure 4.2 (f)) and the high velocity region has started to move towards the centreline of the elbow.

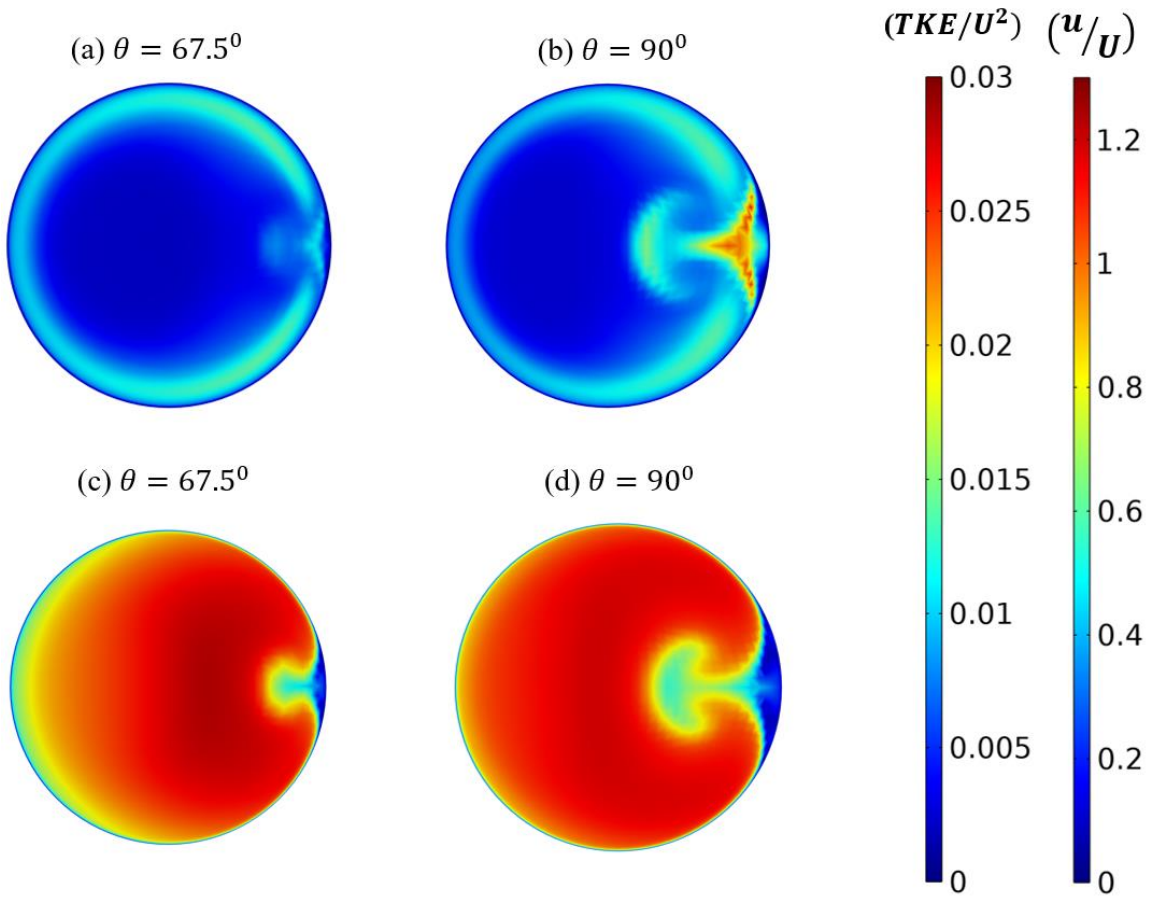

Figure 4.3 In-plane contours of normalized TKE and normalized streamwise velocity in second half of the elbow (a), (b) are normalized TKE and (c), (d) are normalized streamwise velocity

The secondary flow is stronger in the second half of the elbow shown in figure 4.3 compared to the first half shown in figure 4.2. The low velocity region is created on the inner side of the elbow. The mean shear between the low velocity region surrounded by the high velocity region generates the TKE on the inner side of the elbow (as shown in figure 4.3 (a), (b)). The trend of the fluid flow inside the elbow is consistent with the mean axial velocity contours presented by Sudo et al., (1998) and Enayet et al., (1982).

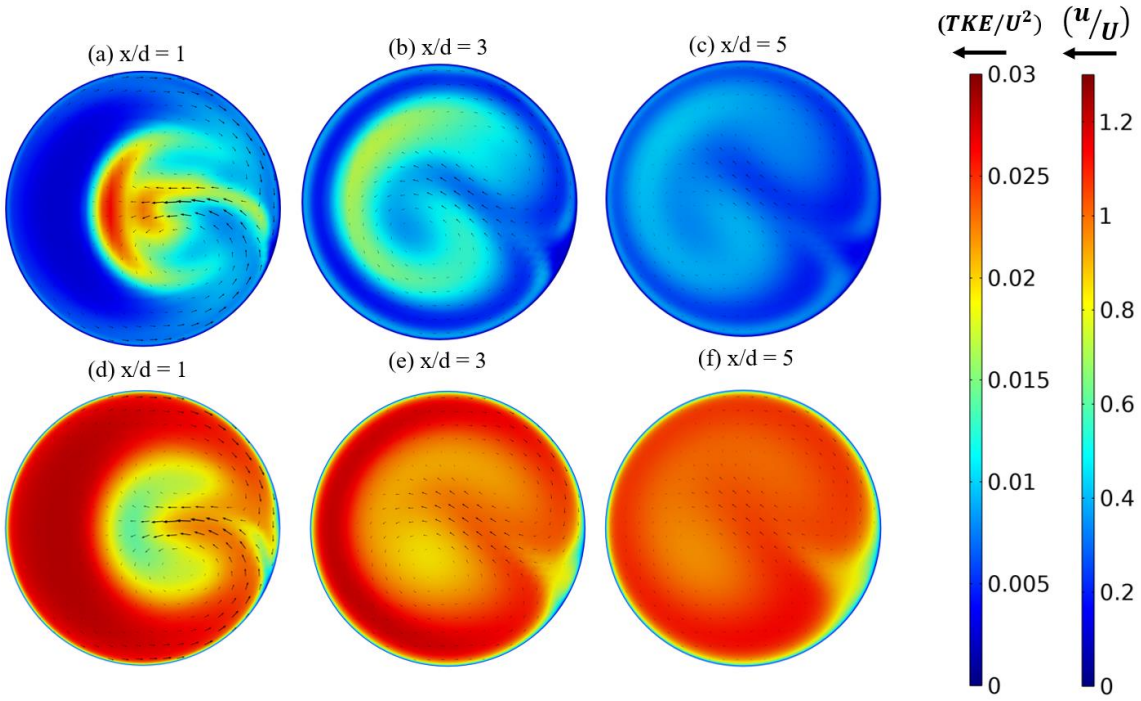

Figure 4.4 In-plane contours of normalized TKE and normalized streamwise velocity close to the elbow outlet (a), (b), (c) are normalized TKE and (d), (e), (f) are normalized streamwise velocity

The location of the low velocity region created due to the secondary flow is closer to the centre of the pipe with increasing downstream distance as shown in figure 4.4. The TKE is also greater in the regions of low velocity surrounded by high velocity as shown in figure 4.4 (a). The strength of the secondary flow is highest at the outlet of the elbow and x/d=1 downstream of the elbow. The strength of the secondary flow starts to diminish at x/d=3 compared to the strength at the outlet of the elbow. The strength of TKE is further reduced at x/d $\geq$ 5. These observations are consistent with the turbulence intensity and mean velocity contours presented by Ikarashi et al., (2018) at x/d=0.5 for r/d=1.5 and presented by Röhrig et al., (2015) at x/d=0.67 for r/d=1.58. The black arrows and their length depict the direction and strength of the secondary flow respectively.

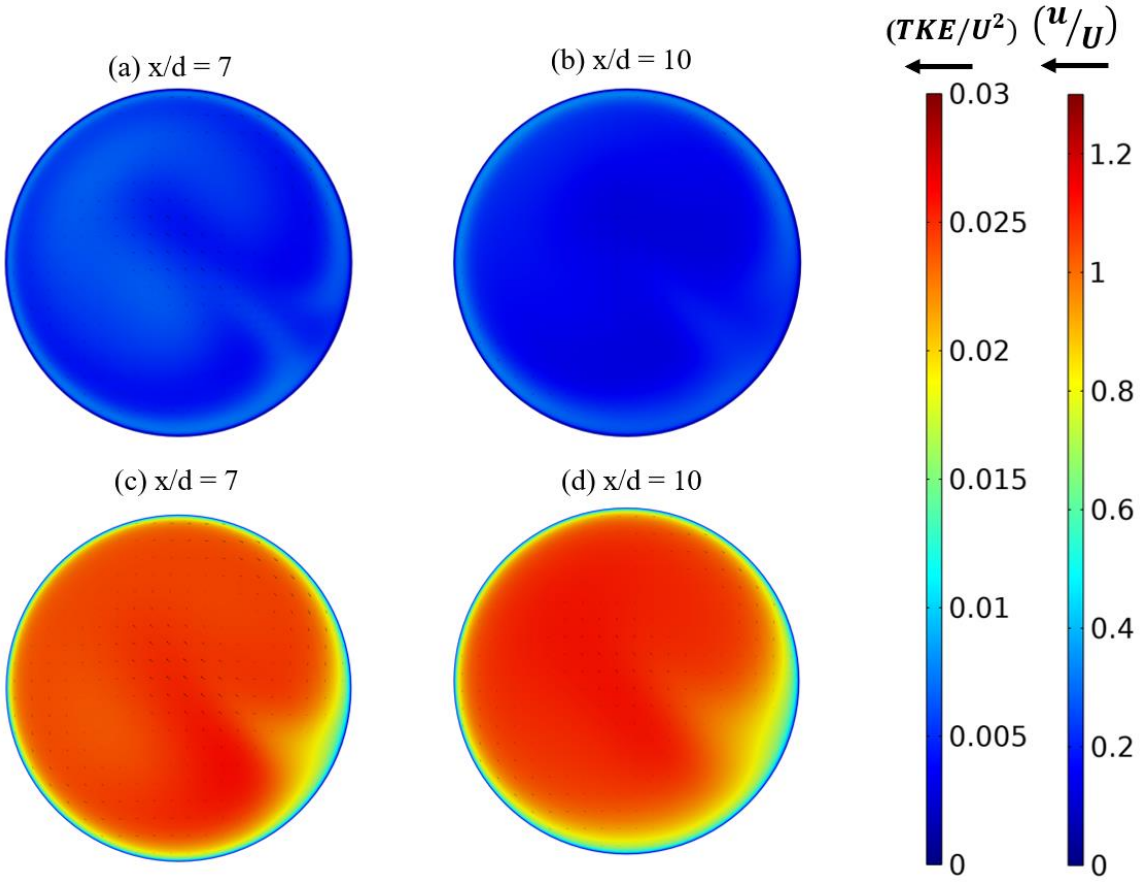

Figure 4.5 In-plane contours of normalized TKE and normalized streamwise velocity further away from the elbow outlet (a), (b) are normalized TKE and (c), (d) are normalized streamwise velocity

The TKE at x/d=10 (as shown in figure 4.5) looks similar to the one at the inlet of the elbow. The strength of the secondary flow is very low at this location compared to the outlet of the elbow.

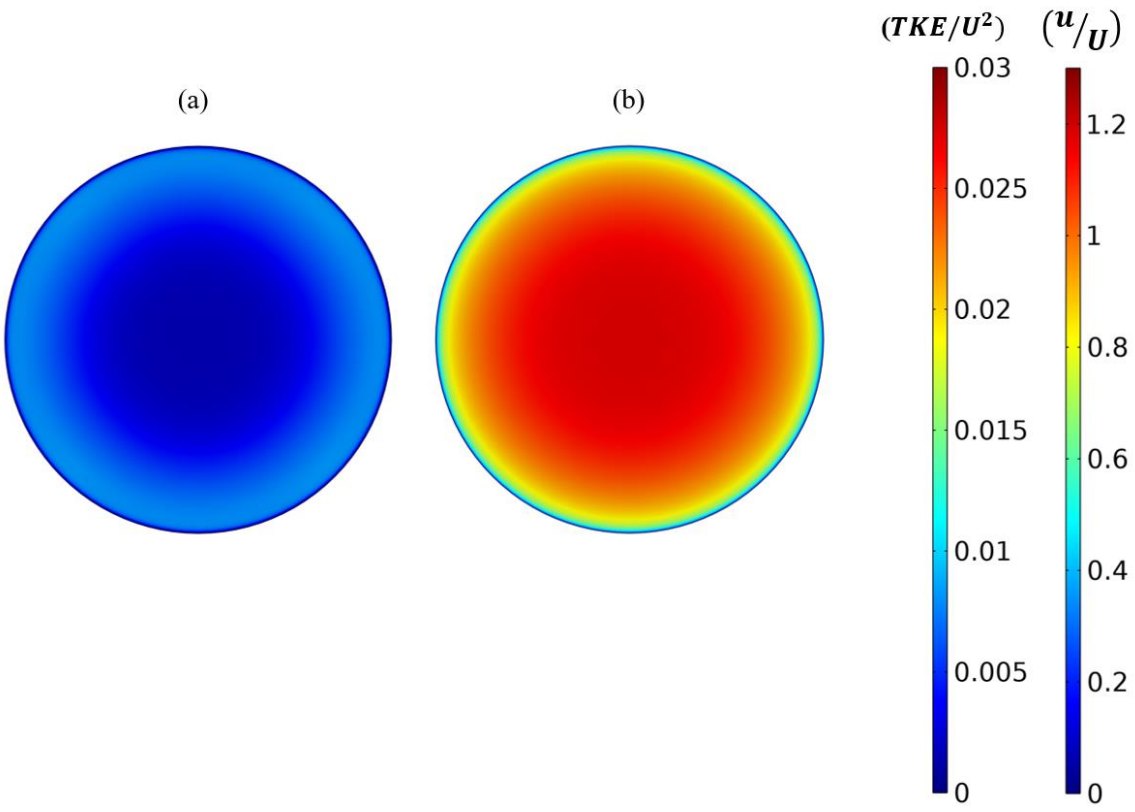

Figure 4.6 In-plane contours of normalized TKE and normalized streamwise velocity for a straight pipe case (a) is normalized TKE and (b) is normalized streamwise velocity

Figure 4.6 (a), (b) shows the contours of normalized TKE and normalized streamwise velocity for the straight pipe case. The flow is symmetric about the axis of symmetry and the TKE is generated near the walls of the pipe as expected. The normalized TKE (as observed from figure 4.6 (a) for the straight pipe case is around 0.01 whereas the normalized TKE at the outlet of the elbow (as shown in figure 4.3 (b)) is at a maximum of 0.03. The spike in TKE at the outlet of the elbow (as shown in figure 4.3 (b) and figure 4.4 (a)) is due to the mean shear between the low and high velocity regions created by the secondary flow generated due to the 90^0 elbow.

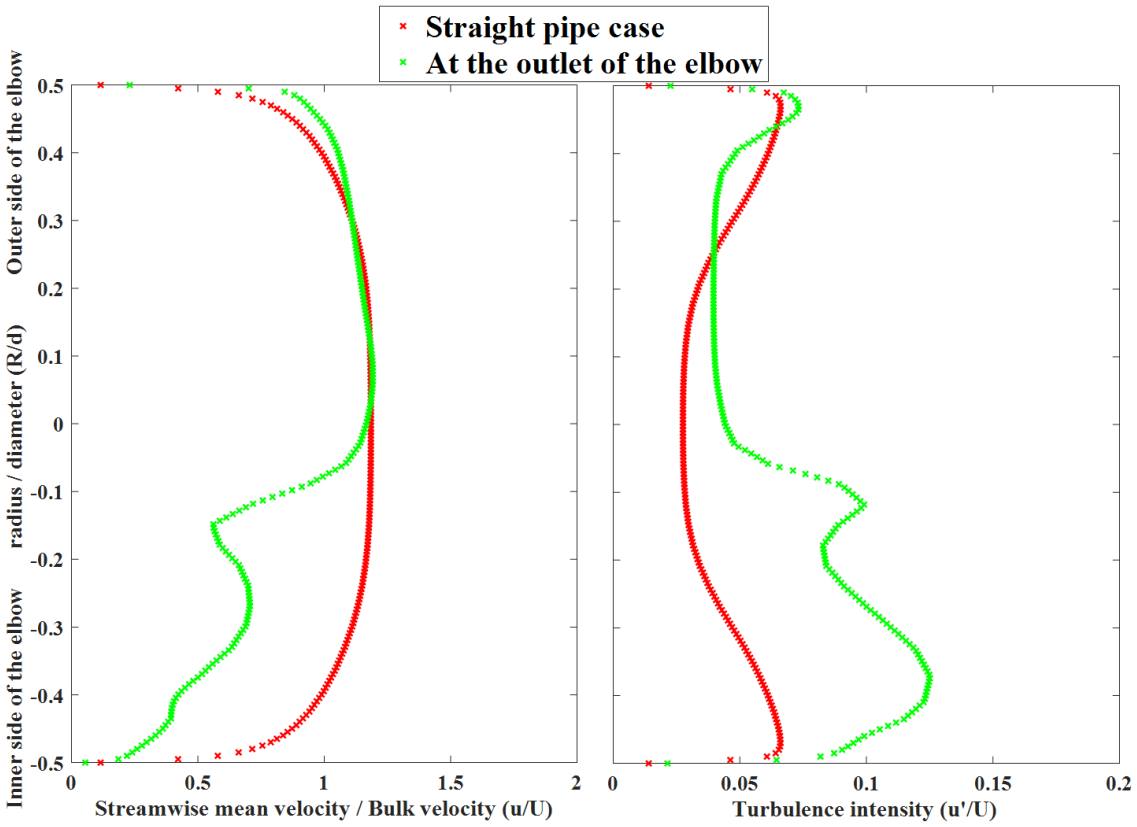

Figure 4.7 Comparison of normalized streamwise velocity and turbulence intensity at the outlet of the elbow and the straight pipe at Re = 33843

For the straight pipe case the normalized streamwise velocity plot (red) on the left hand side of figure 4.7, shows a typical turbulent flow profile in a pipe as presented by Ikarashi et al., (2018). The green curve shows a velocity deficit region on the inner side of the elbow as was observed in figure 4.3 (d). The turbulence intensity curve (red) on the right hand side of figure 4.7, shows a typical behaviour for a flow in the pipe where the turbulence intensity is higher close to the wall as turbulence is generated due to the boundary layer near the walls. The green curve (at the outlet of the elbow) of the turbulence intensity on the right hand side of figure 4.7, show a spike on the inner side of the elbow. This was also observed in figure 4.3 (b). The low velocity region created due to the secondary flow on the inner side of the elbow give rise to an increase in the turbulence intensity. Similar behaviour in the velocity profiles is shown by Ikarashi et al., (2018), Enayet et al., (1982), Taguchi et al., (2018), Tanaka & Ohshima, (2012) and Röhrig et al., (2015).

The behaviour of the streamwise velocity at the installation location of the clamp-on ultrasonic flowmeter (which is x/d=1) needs to be discussed to understand the source of uncertainty in the flowrate measurement.

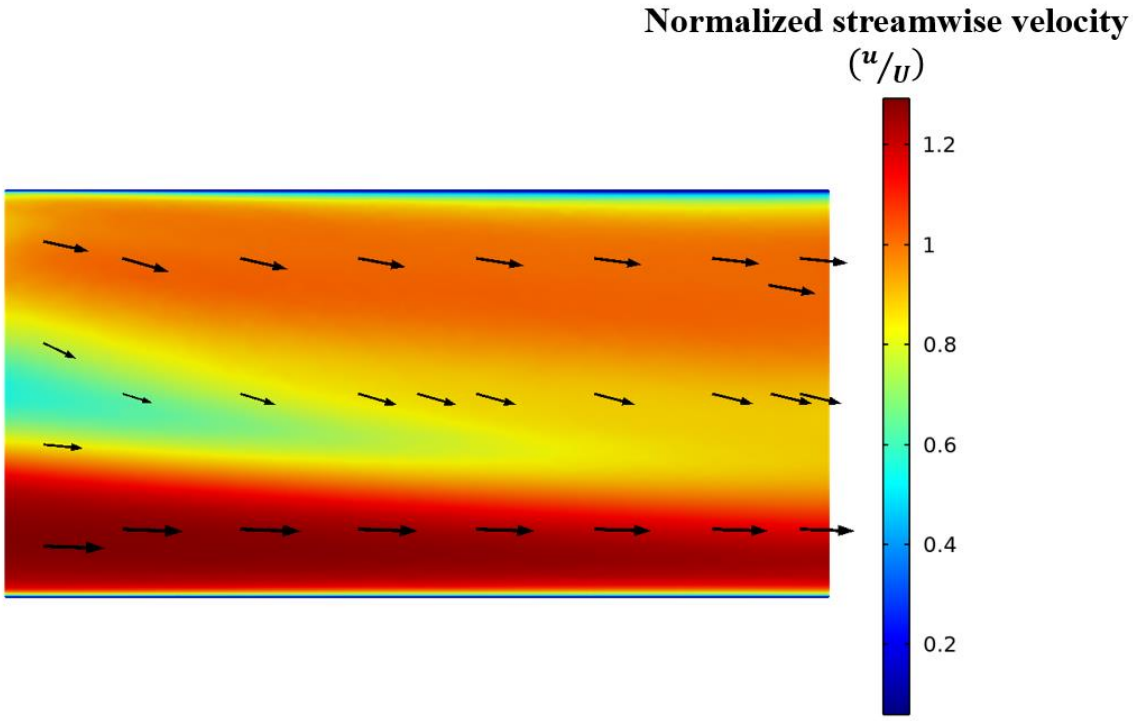

Figure 4.8 Normalized streamwise velocity on the symmetry plane at the installation location (x/d=1) of the clamp-on ultrasonic flowmeter for the pipe with an elbow case

The black arrows in figure 4.8 shows the direction of the fluid flow. The cyan colour region on the left hand side of figure 4.8 depicts the velocity deficit region created due to the secondary flow generated by the 90^0 elbow. Figure 4.9 depicts the superposition of two contours: normalized streamwise velocity contour and the ultrasonic signal depicted as acoustic intensity of the ultrasonic wave. Figure 4.9 is a superposition of figure 4.8 and figure 4.1.

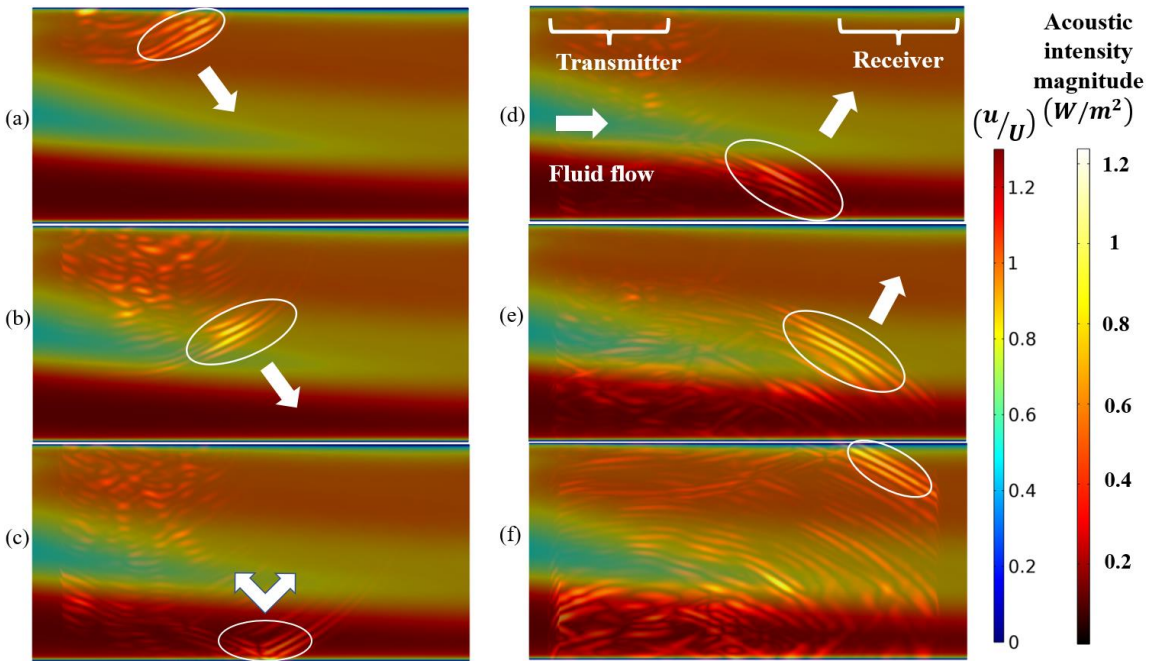

Figure 4.9 Superposition of ultrasonic signal propagation in the direction of the fluid at x/d=1 downstream of the elbow case at different time instances (a) 7µs, (b) 13µs, (c) 20µs, (d) 23µs, (e) 28µs and (f) 35µs

The ultrasonic signal propagation in the direction of the fluid flow at different time instances is shown in figure 4.9. Similarly, figure 4.10 shows the ultrasonic signal propagation in the opposite direction of the fluid flow at the same time instance as depicted in figure 4.9. The ultrasonic signals with high magnitude of acoustic intensity which are leading the propagation of the signal are highlighted with white circles in the figures 4.9 and 4.10. The white arrows show the direction of the propagation of the ultrasonic signals. The difference between the two ultrasonic signal paths in the figure 4.9 and 4.10 is the low velocity region in cyan colour.

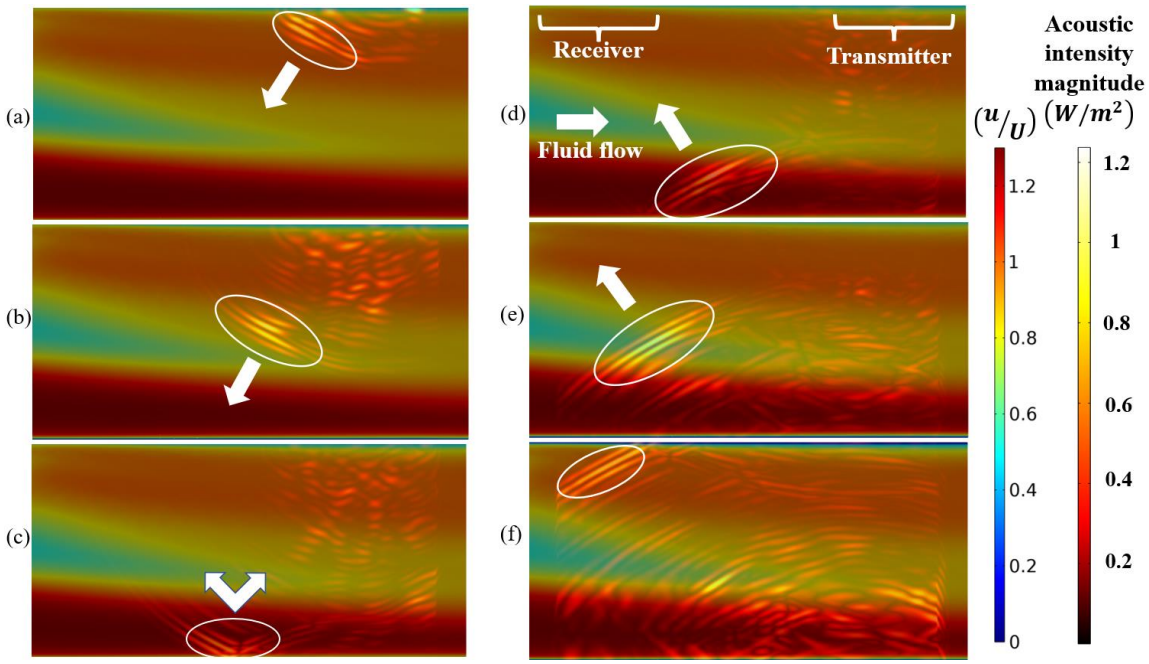

Figure 4.10 Superposition of ultrasonic signal propagation in the opposite direction of the fluid at x/d=1 downstream of the elbow case at different time instances (a) 7µs, (b) 13µs, (c) 20µs, (d) 23µs, (e) 28µs and (f) 35µs

If we compare the contour in figure 4.9 (e) with figure 4.10 (e), the ultrasonic signal in figure 4.10 (e) encounters the low velocity region (cyan colour) when compared to the ultrasonic signal in figure 4.9 (e). Similarly, the ultrasonic signal in figure 4.10 (b) will pass through the low velocity region whereas the ultrasonic signal in figure 4.9 (b) passes close to the low velocity region. Due to this the ultrasonic signal propagating in the opposite direction of the fluid flow (as shown in figure 4.10) encounters the low velocity region compared to the signal moving in the direction of the fluid flow. This causes the uncertainty in the flowrate measurement when the clamp-on ultrasonic flowmeter is installed at x/d=1 downstream of the elbow.

A total of 20 simulations (2 per flowrate) were carried out at 10 flowrates between the flowrate range of $0.3 - 2.5\, m^3/hr$. The flowrate estimated from the simulations at these flowrates is shown in figure 4.11.

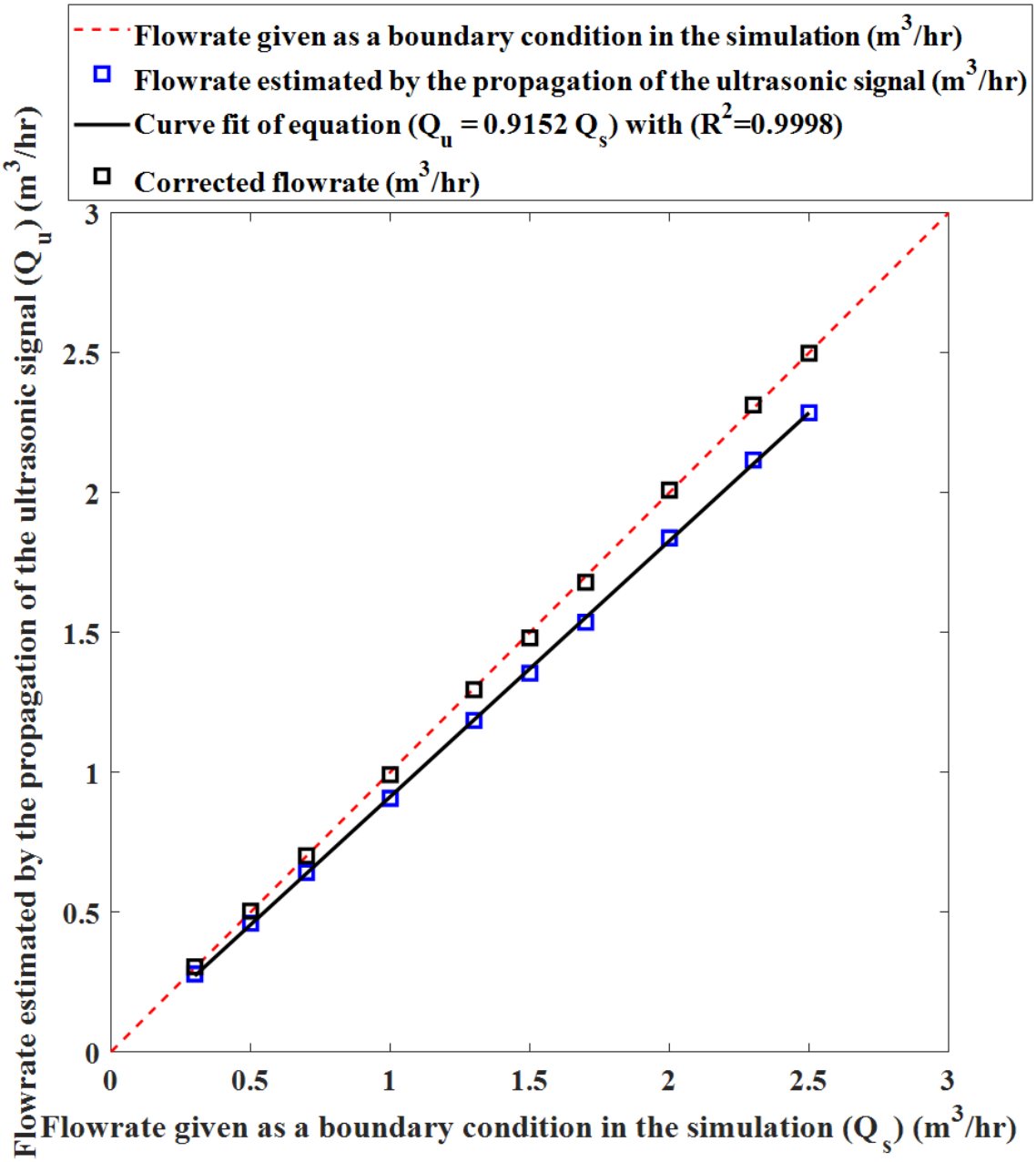

Figure 4.11 Estimated flowrate and its correction for the pipe with an elbow case at the downstream location of x/d=1

In the figure 4.11, dotted red line depicts the flowrate given as a boundary condition prior to the simulation. The blue data points show the estimated flowrate from the simulations for the pipe with an elbow case. The simulations predict lower flowrate compared to the

actual flowrate in the pipe. The average percentage error in the flowrate estimated from the ultrasonic signals (blue data points shown in figure 4.11) is -8.6%.

In the section 1.2.4.3, the time-of-flight principle was discussed. The velocity of the fluid along the ultrasonic path is integrated and estimated according to this principle (as shown in figure 4.13). The equations for the time-of-flight principle are as follows.

The time taken by the wave to propagate in the direction of the fluid flow is given by equations 4.1 and 4.2

$$t_1 = \frac{L}{c+u\sin\theta_3} + \frac{L}{c+u\sin\theta_3} \tag{4.1}$$

where $L = {d_3}/{\cos\theta_3}$

$$t_1 = \frac{2d_3}{\cos\theta_3(c+u\sin\theta_3)} \tag{4.2}$$

Similarly, the time taken by the wave to propagate in the opposite direction of the fluid flow is given by equations 4.3 and 4.4

$$t_2 = \frac{L}{c-u\sin\theta_3} + \frac{L}{c-u\sin\theta_3} \tag{4.3}$$

$$t_2 = \frac{2d_3}{\cos\theta_3(c-u\sin\theta_3)} \tag{4.4}$$

where d_3 is the internal pipe diameter and θ_3 is the angle of ultrasonic wave inside the fluid, c is the speed of sound in the fluid and u is the mean streamwise velocity of the fluid.

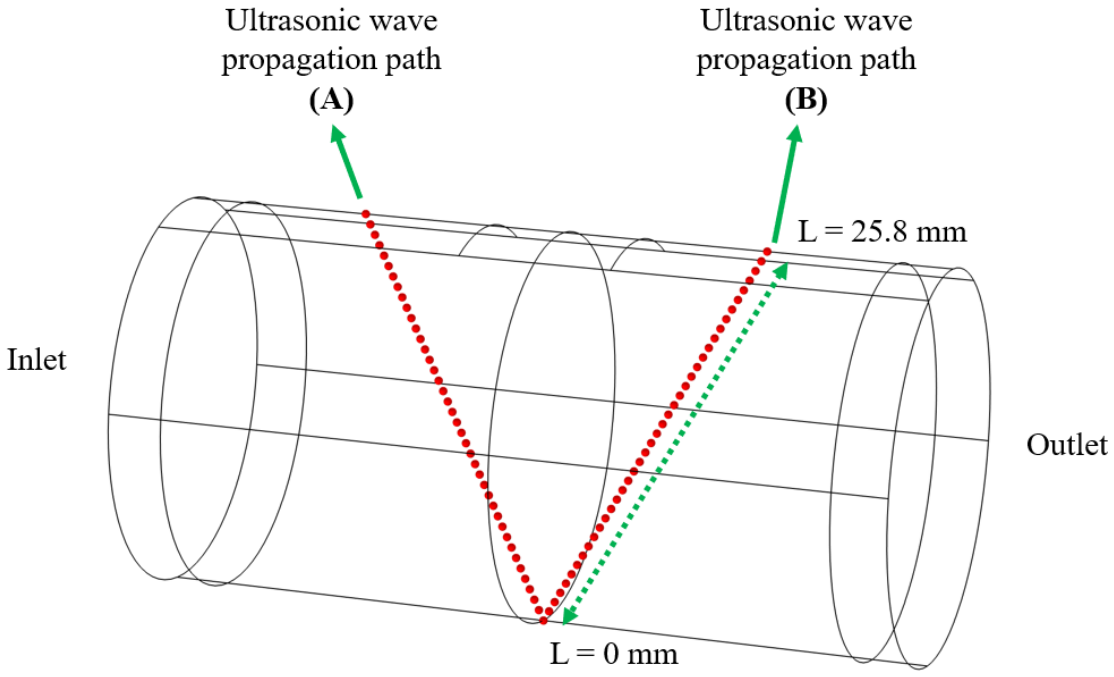

Figure 4.12 Depiction of ultrasonic wave path inside the pipe

The mean streamwise velocity along this path (red dotted line in the figure 4.13) can be obtained from the fluid flow simulations conducted in the numerical study. Each data point on the red dotted line (acoustical path) corresponds to a different value of mean streamwise velocity. The values of those mean streamwise velocity can be input into the equations 4.2 and 4.4 to obtain an array of times t_1 and t_2. Taking the mean of these time arrays give a single value of t_1 and t_2 which can be input into the equation 4.5 to estimate the velocity along the acoustical path.

$$u = \frac{t_2 - t_1}{t_2 + t_1}\left(\frac{c}{\sin\theta_3}\right) \tag{4.5}$$

For the straight pipe case, at a flowrate of 2.0 m^3/hr (which corresponds to a bulk velocity of 1.631 m/s), the numerical simulation of the ultrasonic signals yields a $\Delta t = 25\, ns$ which estimates a velocity of $V = 1.725\, m/s$. The fluid velocity estimated from the procedure explained above using equations 4.2, 4.4 and 4.5 is $u = 1.704\, m/s$.

If the flowrate Q is estimated using the value of u obtained from the equation 4.5 or the value of V estimated from the ultrasonic signals (where the Δt is estimated from the simulations) the value of flowrate Q would have larger error compared to if the value of flowrate Q is estimated from the bulk velocity (velocity integrated along the pipe cross-section).

$$Q = \left(\frac{V \text{ or } u}{K}\right)\frac{\pi.{d_3}^2}{4} \tag{4.6}$$

In order to correct the value of velocity (integrated along the red dotted path in figure 4.12), a flow profile correction factor $K = 1.119 - 0.011\log_{10}(Re)$, was estimated for a turbulent velocity profile in a smooth pipe proposed by Lynnworth, (1979) and Kocis & Figura, (1996). This value of K can be used in the equation 4.6 to estimate the fluid flowrate for a straight pipe case.

Similarly for the pipe with an elbow case, the velocity along the ultrasonic path (red dotted line in figure 4.12) is estimated using equations 4.2, 4.4 and 4.5. The time t_1 and t_2 are estimated and are used to estimate the velocity along the acoustic path which is $u = 1.525\ m/s$ for a flowrate of $2.0\ m^3/hr$. This value of u would change depending upon the number of points at which the velocity is integrated along the acoustic path (red dotted line in figure 4.12). The velocity estimated by the numerical simulation of the ultrasonic signals for this case has a $\Delta t = 22\ ns$ which estimates a velocity of $V = 1.518\ m/s$. However, the bulk velocity given as the boundary condition is $1.631\ m/s$.

So, a curve (black curve in figure 4.11) is fit to the numerical data (blue data points) in figure 4.11. A correction factor is proposed in equation 4.7 which is applied to the blue data points to achieve the black data points in the figure 4.11. This correction factor is specific for the pipe with a 90^0 elbow case (r/d=1.6) where the ultrasonic flowmeter is installed at x/d=1 downstream of the elbow for the Re number range of $5.077 \times 10^3 < Re < 4.23 \times 10^4$ which corresponds to the flowrate range of $0.3 - 2.5\ m^3/hr$.

$$Q_c = 1.093\ Q_u \tag{4.7}$$

where Q_c is the corrected flowrate (shown in black data points in figure 4.11) and Q_u is the flowrate estimated by the numerical simulations for the pipe and elbow case. The average percentage error of the corrected flowrate is 0.7%.

A contour of acoustic pressure is presented in figure 4.13 which is on a plane created at the location of the ultrasonic wave propagation path (B) shown in figure 4.12.

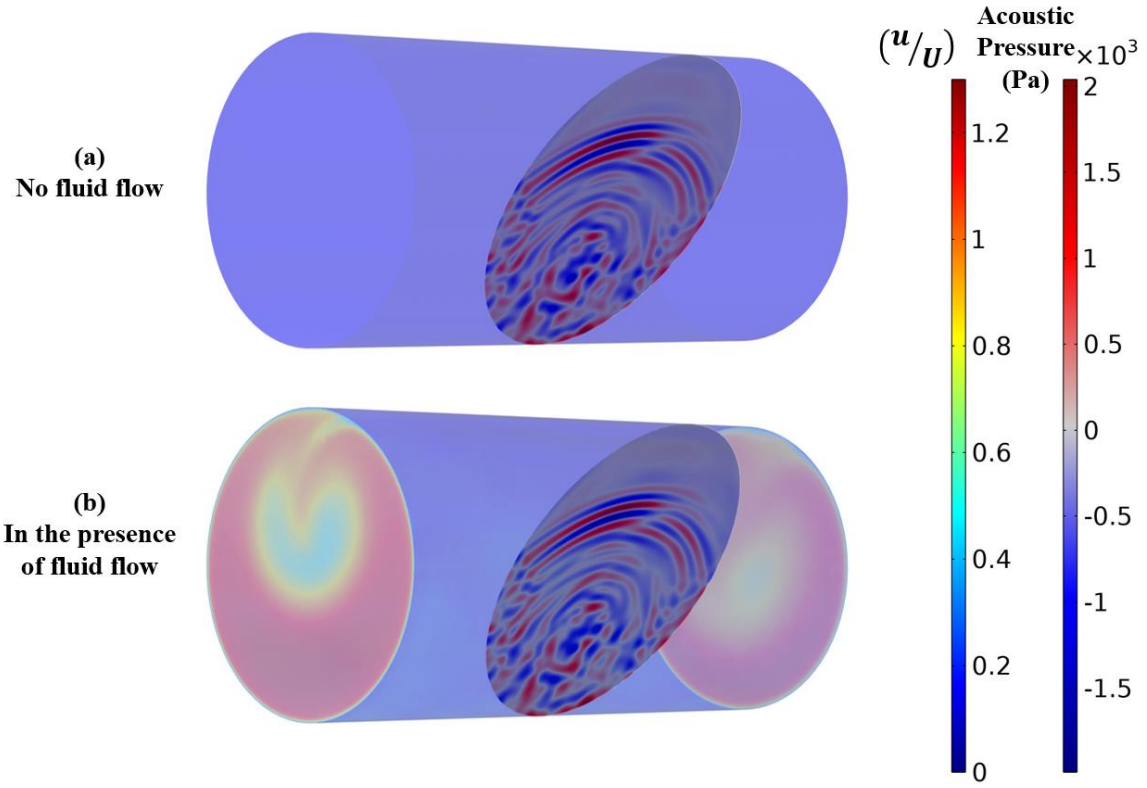

Figure 4.13 Acoustic pressure due to the ultrasonic wave at a plane on the ultrasonic wave path B (as shown in figure 4.12) at a time instance of 35μs (a) Ultrasonic wave propagation with no fluid flow, (b) Ultrasonic wave propagation in the presence of fluid flow

From the visual inspection of the contours presented in figure 4.13, the effect of the fluid flow on the propagation of the ultrasonic wave is not evident. As the ultrasonic propagation contours on the planes in both figure 4.13 (a) and figure 4.13 (b) look identical to each other. However, the fluid flow certainly effects the propagation of the ultrasonic wave which can be understood by figure 4.14.

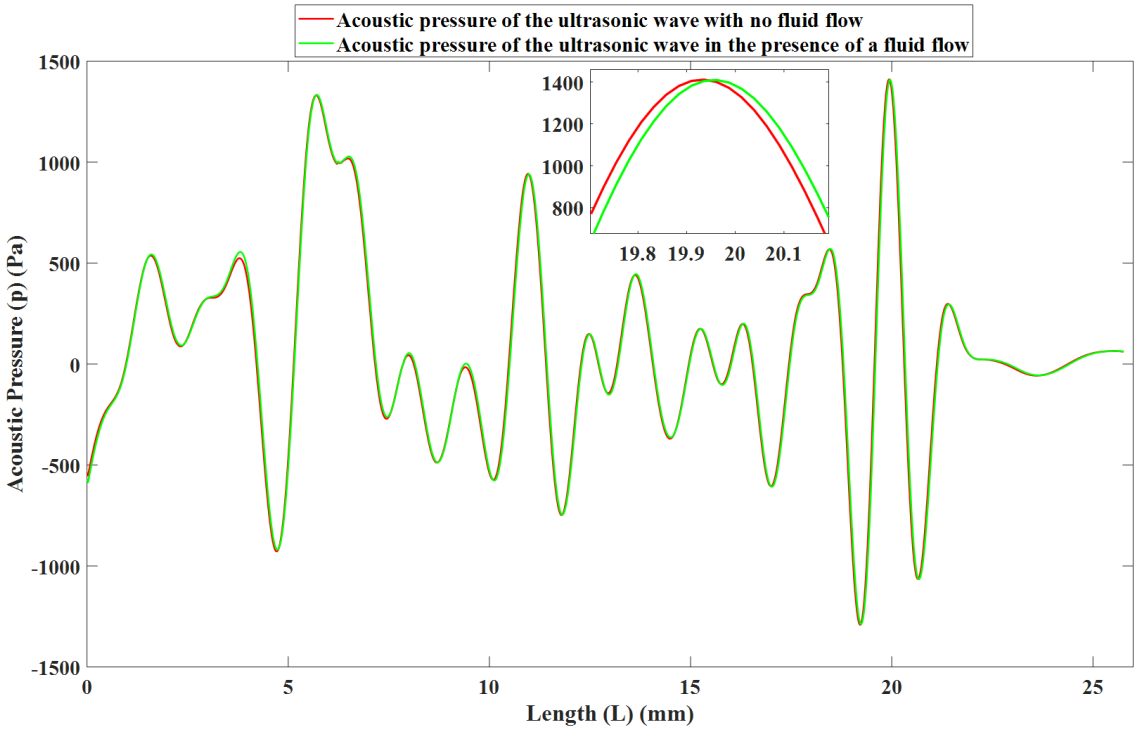

Figure 4.14 Comparison of acoustic pressures at a time instance of 35μs without the presence of fluid flow case and with a fluid flowrate case along the ultrasonic propagation path B (as shown in figure 4.12)

The acoustic pressure along the red dotted line (as shown in figure 4.12 path B) is shown in figure 4.14 for the two cases: one in the presence of fluid flowrate case and the other with no fluid flowrate case. The x-axis in figure 4.14 shows the length of the ultrasonic wave propagation path B (as shown in red dotted line in figure 4.12) where 0mm (in figure 4.14 left hand side) denotes the lower end (lower end of pipe wall) of the red dotted line and 25.8mm (in figure 4.14 right hand side) denotes the upper end of the red dotted line (just before entering the receiver). It can be observed in figure 4.14, that the acoustic pressure which corresponds to the ultrasonic wave which is propagating in the presence of fluid flow (green curve) is leading (by $1ns$) the acoustic pressure which corresponds to the ultrasonic wave which is propagation in a static fluid (red curve). This means that the speed of the ultrasonic wave is augmented by the presence of a fluid flowrate as evident from the green curve in figure 4.14. The comparison of figures 4.13 and 4.14 tells that the

orientation, amplitude and path of propagation of the ultrasonic wave inside a fluid is not disturbed by the fluid flowrate.

4.1.2 Summary of numerical results

The results of the numerical study include the modelling of fluid flow in a straight pipe and pipe with an elbow cases. The effects of secondary flow are evident inside and downstream of the elbow where TKE increases to a maximum value due to the low velocity region at the outlet of the elbow and gradually decays, away from the outlet of the elbow. The percentage error in the flowrate estimated from the simulations is -8.6% which is reduced to 0.7% after applying the correction factor. The orientation, path of the propagation and amplitude of the ultrasonic wave inside a fluid is not disturbed due to the fluid flowrate. The local fluid velocity attenuates the ultrasonic wave's velocity and pressure.

4.2 Experimental results

According to the experimental technique discussed in chapter 3, experiments were conducted on the straight pipe section and downstream of the elbow. Five clamp-on ultrasonic flowmeters from one manufacturer were used as test meters.

4.2.1 Repeatability of the clamp-on ultrasonic flowmeters

The repeatability tests were carried out on all five clamp-on ultrasonic flowmeters onto the straight pipe section. The mounting clamp of the clamp-on ultrasonic flowmeters was not disturbed, only the flowmeters were unclamped and re-clamped onto the mounting clamp for the repeatability test. This test was carried out at three flowrates in the flowrate range considered in this thesis which are lowest ($0.3\ m^3/hr$), highest ($2.5\ m^3/hr$) and the middle ($1.5\ m^3/hr$) flowrate. The figure 4.7 shows the data points for the repeatability test.

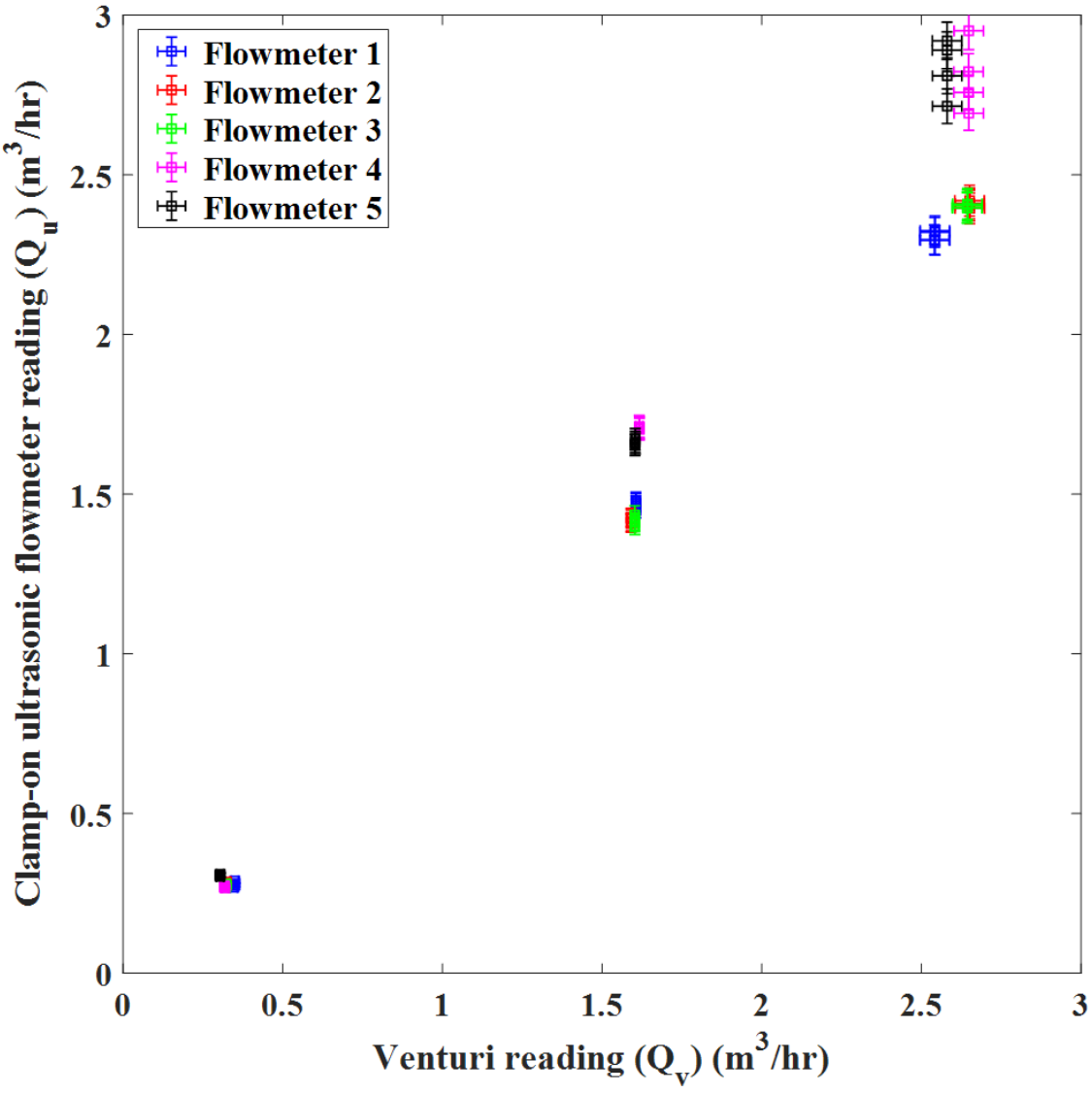

Figure 4.15 Repeatability results for clamp-on flowmeters at three flowrates

For flowmeter 1, 2 and 3, the data are not scattered for the flowrate range under consideration. For the flowmeter 4 and 5 the data are scattered at the highest flowrate. The signal quality of the flowmeter 4 and 5 at the highest flowrate is not stable due to which the flowrate readings are scattered. As shown in figure 4.15, each flowmeter was clamped and re-clamped four times at three flowrates and the value of flowrate is recorded. The recorded values of flowrate are shown in figure 4.15 with the horizontal error bars show the uncertainty in the measurement of the venturi flowmeter and vertical error bars show the uncertainty in the measurement of the clamp-on ultrasonic flowmeters. The

uncertainties mentioned as error bars are specified by the manufacturer. Equation 4.8 is used to compute the percentage difference between the 4 recorded value at each flowrate and for each flowmeter.

$$Percentage\ difference = \frac{|Value\ 1 - Value\ 2|}{(Value\ 1 + Value\ 2/2)} \times 100 \quad (4.8)$$

The percentage difference estimated from equation 4.8 between the recorded values for each flowmeter is averaged and presented in table 4.1.

Table 4.1 Average percentage difference for each flowmeter for the repeatability test

Flowmeter	Average percentage difference %
1	1.6
2	1.5
3	1.6
4	2.1
5	2.2

The table 4.1 provides an insight into how much the flowrate readings of these clamp-on ultrasonic flowmeter vary due to clamping and un-clamping process for the specified flowrate range. So, it can be concluded that for these specific clamp-on ultrasonic flowmeters, the average variability for all flowmeters is $\pm 1.8\%$ which contribute towards the uncertainty in the flowrate readings.

Having discussed the repeatability results, the performance of these flowmeters on the straight pipe and downstream of the elbow at x/d=1 is discussed further in this chapter.

4.2.2 Straight pipe vs downstream of the elbow measurements

The measurement locations for the test flowmeters (clamp-on ultrasonic flowmeter) are depicted in figure 3.2 as locations A, B and C. In this section, the measurements taken at the location B and C are discussed because the pipe material (stainless steel) is the same at these locations. Location C is a straight pipe section whereas location B is downstream of the elbow at x/d=1. At location B, the clamp-on ultrasonic flowmeter can be mounted in 2

ways: In the plane of the elbow and perpendicular to the plane of the elbow. In figure 3.2, the clamp-on flowmeter at the location B is mounted perpendicular to the plane of elbow. Similarly, at the location C (straight pipe), the flowmeters are installed in two orientations with a 90^0 angle between them.

Figures 4.16, 4.17, 4.18, 4.19 and 4.20 show the experimental data plotted for each clamp-on flowmeter at the location B and C in both orientations. The in-line ultrasonic data points (red) in these figures have a vertical error bar showing ±5% uncertainty in the reading value. The horizontal error bars on all data points show the venturi flowmeter's uncertainty which is ±1.1% in the reading value for flowrate range of 0.3 < flowrate < 2.0 m^3/hr and ±4.6% in the reading value for flowrate range of 2.0 > flowrate < 2.5 m^3/hr. The vertical error bars on clamp-on flowmeter's data points show the ±2% uncertainty in the reading value.

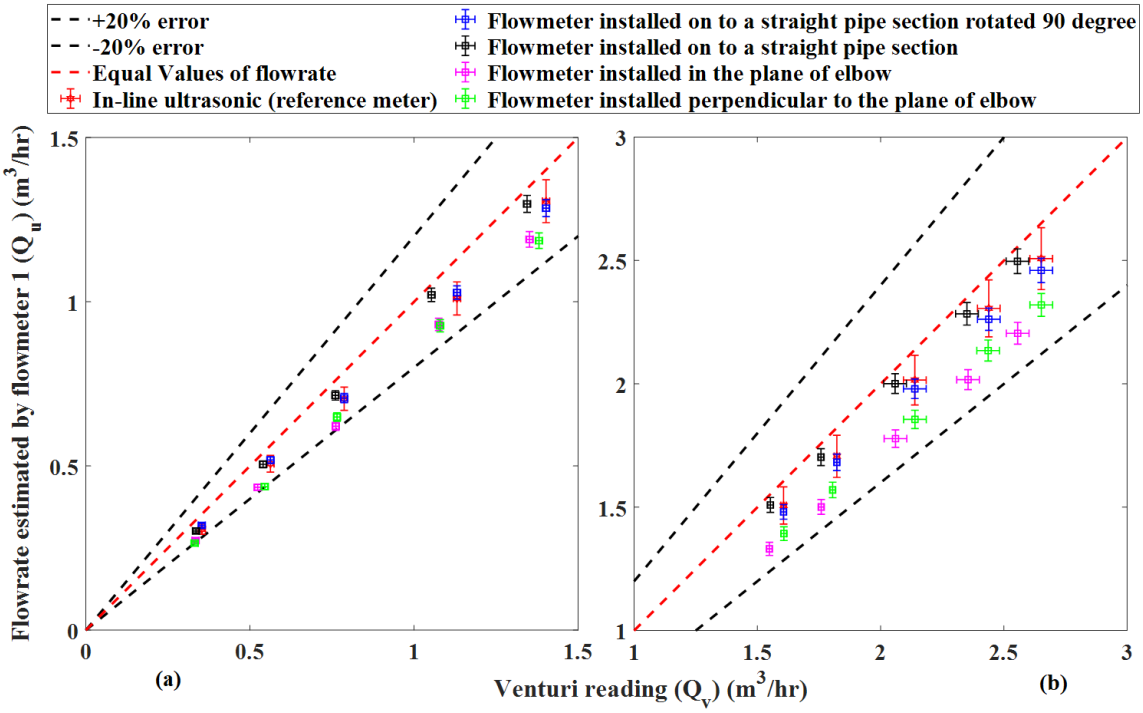

Figure 4.16 Data measured by clamp-on flowmeter 1 at different locations (a) flowrate range (0-1.5 m^3/hr), (b) flowrate range (1-3 m^3/hr)

In figure 4.16, the measurements of the clamp-on flowmeter at the straight pipe location (blue and black) are close to the inline and venturi measurements when compared to the data points when the clamp-on flowmeter is installed after the elbow (green and magenta).

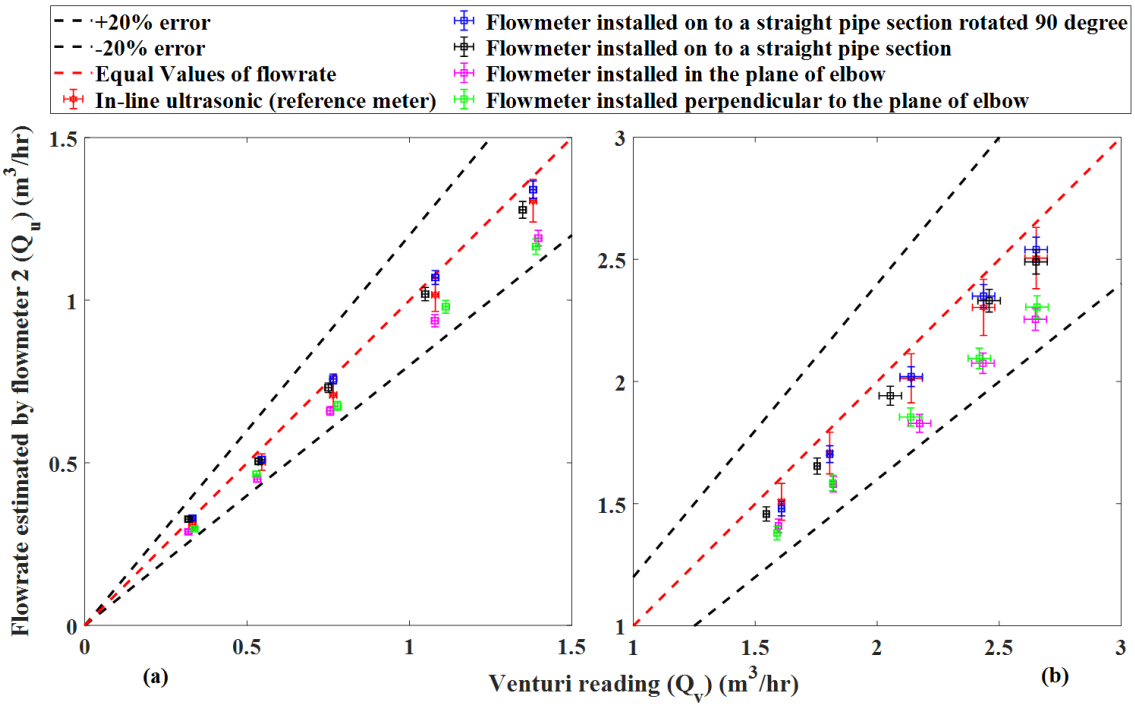

Figure 4.17 Data measured by clamp-on flowmeter 2 at different locations (a) flowrate range (0-1.5 m^3/hr), (b) flowrate range (1-3 m^3/hr)

The flowrates measured by the clamp-on flowmeter 2 are shown in figure 4.17. The difference in the data points for the straight pipe section compared to the data after the elbow is obvious at all flowrates. The trend in the readings is similar to that observed in the data of flowmeter 1.

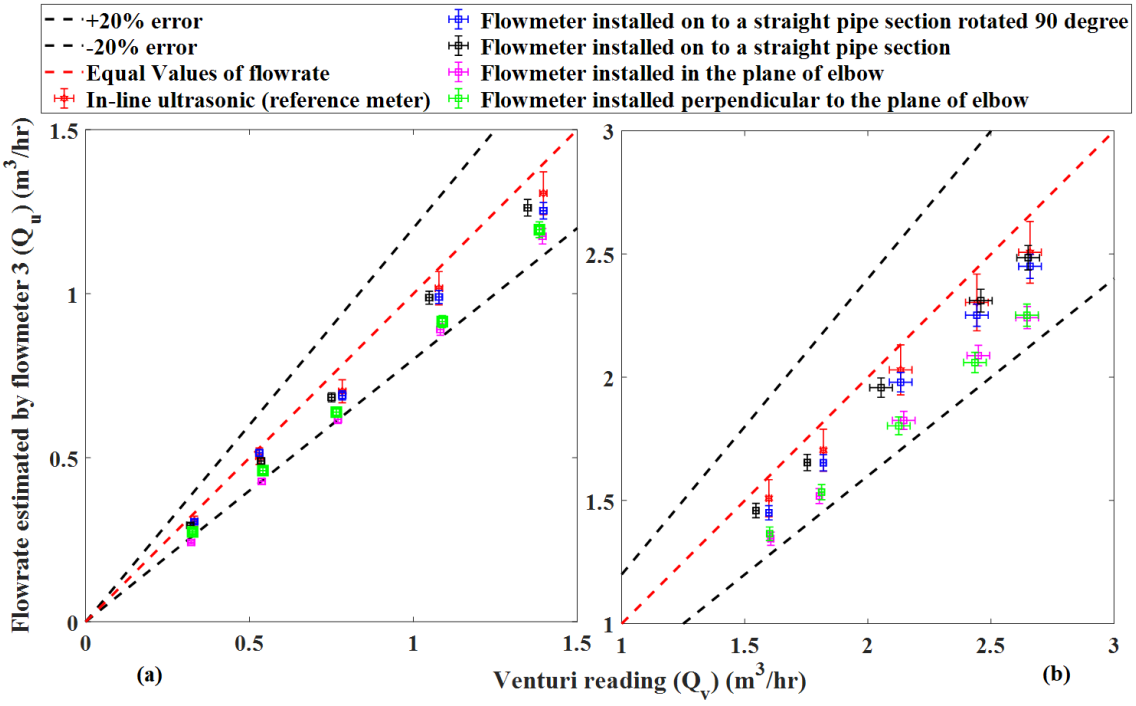

Figure 4.18 Data measured by clamp-on flowmeter 3 at different locations (a) flowrate range (0-1.5 m^3/hr), (b) flowrate range (1-3 m^3/hr)

A trend similar to that observed in the flowmeters 1 and 2 is observed in the flowmeter 3. The comparison between the data points measured by flowmeters 1, 2 and 3 are as follows.

- The average percentage difference between the venturi and the in-line ultrasonic readings for all of the experiments is 6.2%.

- The flowmeters 1, 2 and 3 are under predicting compared to the venturi reference reading by 7.4%, 4.3% and 7.4% respectively for the straight pipe case. For the downstream of the elbow case these meters underpredict by 16%, 13.3% and 16.4% respectively.

- For the straight pipe measurement location, the clamp-on readings are very close to the in-line ultrasonic meter reading (reference meter). The average percentage difference between the straight pipe clamp-on (for flowmeter 1, 2 and 3) readings and the in-line ultrasonic flowmeter are 1.1%, 2.2% and 2.4% respectively.

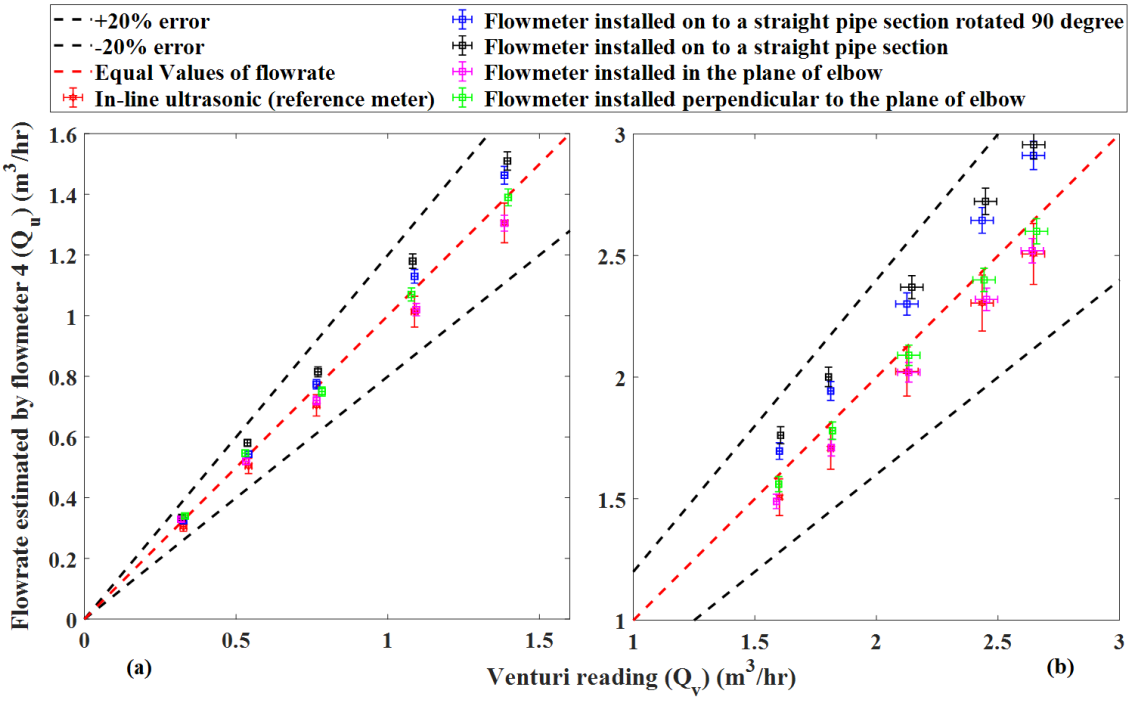

Figure 4.19 Data measured by clamp-on flowmeter 4 at different locations (a) flowrate range (0-1.5 m^3/hr), (b) flowrate range (1-3 m^3/hr)

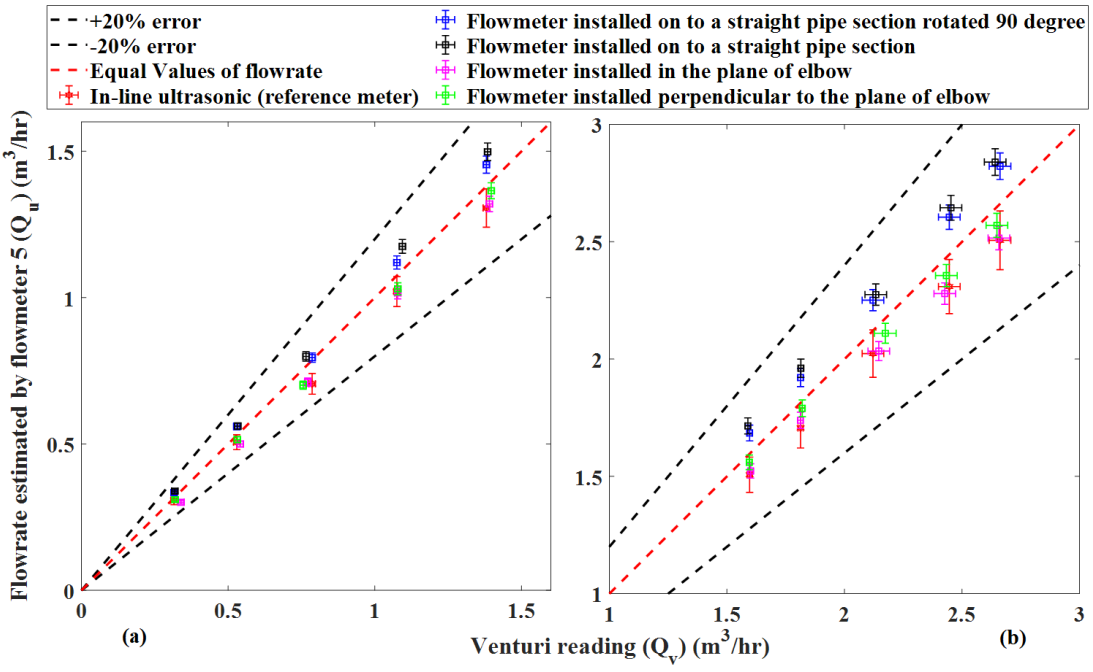

Figure 4.20 Data measured by clamp-on flowmeter 5 at different locations (a) flowrate range (0-1.5 m^3/hr), (b) flowrate range (1-3 m^3/hr)

The data measured by flowmeters 4 and 5 are presented in figures 4.19 and 4.20, respectively. These two flowmeters overpredict when compared to the venturi flowmeter for the straight pipe location (blue and black). For the in-plane of the elbow location (magenta) and perpendicular to the plane of the elbow location (green) the data underpredict compared to the venturi readings.

When the data from the flowmeters 4 and 5 is compared to the data from flowmeters 1,2 and 3 following conclusion can be drawn.

- The trend of the data measured by all of the flowmeters is similar which is that there is a relative difference between the straight pipe (blue and black) and downstream of the elbow (green and magenta) measurements. The average percentage difference between the straight pipe data and downstream of the elbow data for the flowmeters 1, 2, 3, 4 and 5 is 10.6%, 9.2%, 9.3%, 9.8% and 10.4%.

- The change in the orientation of the meters downstream of the elbow or on the straight pipe section has a minimal effect on the readings. The average percentage

difference for flowmeters 1, 2, 3, 4 and 5 in the readings due to the change in the orientation at the straight pipe and downstream of the elbow is 2.5%, 2.4%, 2.5%, 3.9% and 2.2% respectively.

- The data from the flowmeters 4 and 5 for all locations seem to be shifted when compared to the data from flowmeters 1, 2 and 3. Due to this, the data obtained downstream of the elbow for flowmeters 4 and 5 are close (with a percentage difference of 3.6% and 4.8% respectively) to the reference measurement when compared to the straight pipe location.

Table 4.2 summarizes the data presented in the figures 4.8, 4.9, 4.10, 4.11 and 4.12.

Table 4.2 Average percentage error for each flowmeter mounted on the straight pipe section and downstream of the elbow in both orientations for the specified flowrate range

Flowmeters	Mounting location	Average percentage error %
1	Straight pipe in both orientations	-7.4
	Downstream of the elbow at x/d = 1 in both orientations	-16.0
2	Straight pipe in both orientations	-4.3
	Downstream of the elbow at x/d = 1 in both orientations	-13.3
3	Straight pipe in both orientations	-7.4
	Downstream of the elbow at x/d = 1 in both orientations	-16.4
4	Straight pipe in both orientations	7.1
	Downstream of the elbow at x/d = 1 in both orientations	-3.6
5	Straight pipe in both orientations	6.1
	Downstream of the elbow at x/d = 1 in both orientations	-4.8

In order to use these flowmeters downstream of the elbow at x/d=1, the average percentage error at this location for these flowmeter needs to be corrected.

4.2.3 Proposed correction factors

In order to propose a correction factor, the data points from flowmeters 1, 2 and 3 are plotted on a single plot. Figure 4.21 shows the data points measured by the flowmeters 1, 2 and 3 downstream of the elbow at x/d=1 in both orientations.

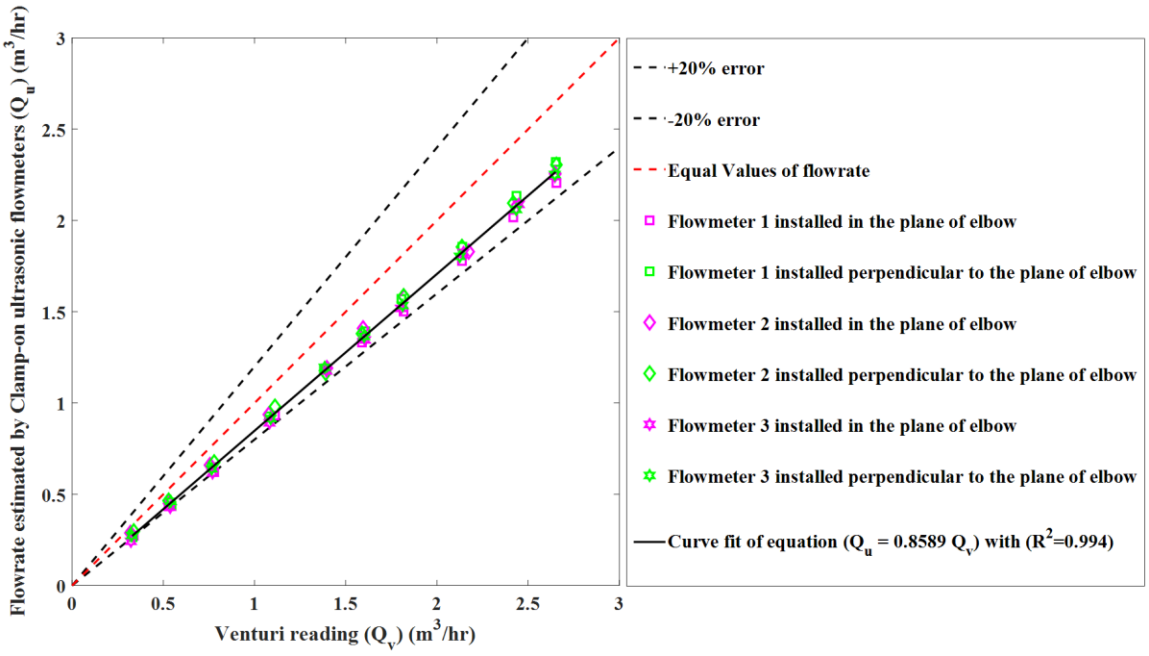

Figure 4.21 Data points measured by the flowmeters 1, 2 and 3 at x/d=1 downstream of the elbow in both orientations

A curve shown in solid black line is fit to the data points in figure 4.21. A linear equation (as shown in figure 4.21) describes the black solid curve fitted to the data. A correction factor in equation 4.9 is proposed that reduces the average percentage error in the reading of clamp-on ultrasonic flowmeters 1, 2 and 3.

$$Q_c = 1.18\, Q_u \tag{4.9}$$

where Q_u is the flowrate measured by the clamp-on ultrasonic flowmeter as shown in the data points in figure 4.21 and Q_c is the corrected flowrate as shown in the data points in figure 4.22.

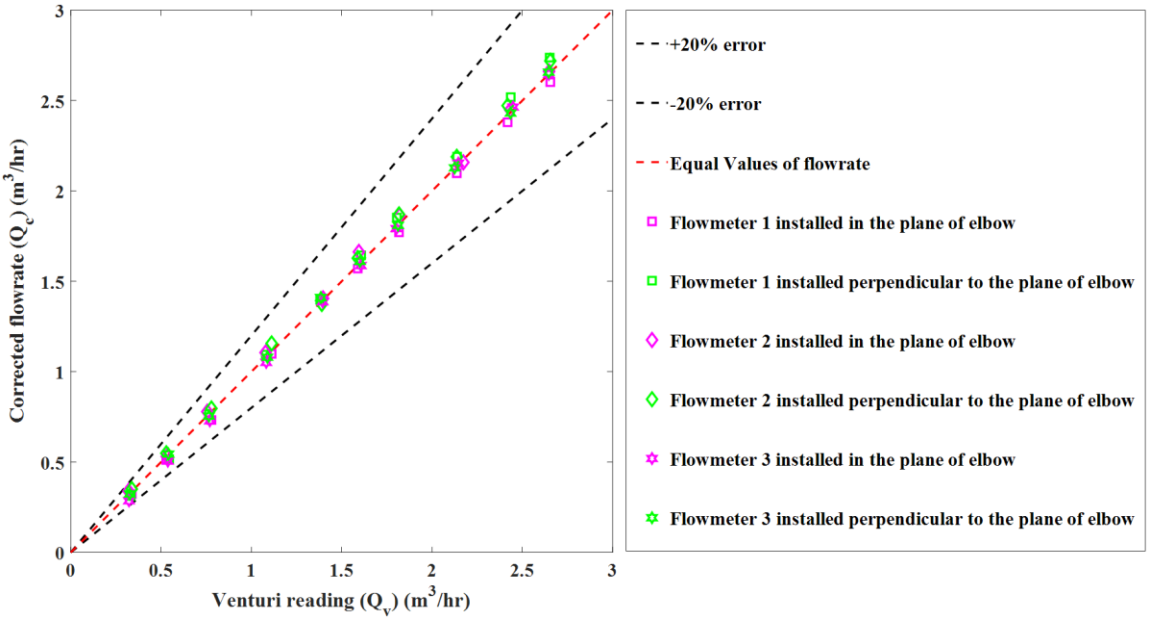

Figure 4.22 The estimated flowrate from flowmeter 1, 2 and 3 after applying the correction factor

After applying the correction factor specified in the equation 4.9, the average percentage error in the measurement of the flowmeters 1, 2 and 3 reduces to 2.6%, 2.4% and 1.8% respectively.

4.2.4 Summary of experimental results

For the experimental study, the repeatability test shows a $\pm 1.8\%$ uncertainty in the flowrate measured by the clamp-on ultrasonic flowmeters which is close to the $\pm 2\%$ stated by the manufacturer. Flowmeters 1, 2 and 3, for the straight pipe case, under predict the flowrate by an average of 6.3% whereas downstream of the elbow they under predict the flowrate by an average of 15.2%. Flowmeters 4 and 5, for the straight pipe case, the flowmeters over predict the flowrate by an average of 6.6% whereas downstream of the elbow they under predict the flowrate by an average of 4.2%. All of the five clamp-on ultrasonic flowmeters are of the same model and supplied by the same manufacturer.

Flowmeters 4 and 5 were bought 8 months before flowmeters 1, 2 and 3. According to the manufacturer, the algorithm for the flowmeters 1, 2 and 3 was updated compared to flowmeters 4 and 5. This is the reason for a similar trend obvious in the measurements taken by flowmeters 1, 2 and 3 compared to a slightly shifted trend in the measurements taken by flowmeters 4 and 5. The correction factor proposed by the experimental study for the downstream installation location for the flowmeters 1, 2, and 3 reduce the percentage error to an average of $\pm 2.3\%$. This correction factor is limited to the clamp-on ultrasonic flowmeters being used in this study which is clamped onto a stainless-steel pipe and elbow setup of r/d=1.6 at x/d=1 downstream of the elbow. The average percentage error in the measurements of flowmeters 4 and 5 at x/d=1 downstream of the elbow is -4.2%. The uncertainty in the measurements of the venturi flowmeter is $\pm 1.1\%$ for flowrate range of 0.3 < flowrate < 2.0 m^3/hr and $\pm 4.6\%$ for flowrate range of 2.0 > flowrate < 2.5 m^3/hr as shown in error bars in figures 4.16 to 4.20. Similarly, a $\pm 2\%$ uncertainty in the measurements of clamp-on ultrasonic flowmeters also exists. So, the correction factor for flowmeters 4 and 5 at the downstream location is not proposed.

4.3 Summary

The numerical simulation helps to understand and visualize the structure of the fluid flow inside and downstream of a 90^0 elbow. TKE is generated by the walls of the pipe and for the straight pipe case it is symmetric about the axis of the pipe's cross-section. For the pipe and elbow case, TKE starts to move towards the outer side of the elbow in the first half of the elbow and then moves towards the inner side of the elbow. The magnitude of TKE is highest at the outlet of the elbow compared to other locations inside or downstream of the elbow. The secondary flow generated due to a 90^0 elbow has two counter rotating vortices and a low velocity region is created. The fluid velocity accelerates or decelerate the acoustic wave propagation without changing the intensity, direction or amplitude of the ultrasonic wave. Due to the low velocity region at x/d=1 downstream of the elbow, an average percentage error of -8.6% is introduced in the clamp-on ultrasonic flowmeter's measurement. The experimental investigation of five clamp-on ultrasonic flowmeter show

an average percentage error of -10.8% at x/d=1 downstream of the elbow location. Stoker et al., (2012) estimated a percentage error of -9.8% at x/d=1.5 in the measurement of a clamp-on ultrasonic flowmeter and Johnson et al., (2001) estimated a percentage error of -12% at x/d=2 in the measurement of a clamp-on ultrasonic flowmeter. The proposed correction factors for the numerical and experimental studies reduce the average percentage error in the flowrate to $\pm 0.7\%$ and $\pm 2.3\%$ respectively. The repeatability experiments conclude an average percentage uncertainty of $\pm 1.8\%$ in the measurements of five clamp-on ultrasonic flowmeters compared to the ±0.2% estimated by Mahadeva et al., (2009), $\pm 0.4\%$ estimated by Schwery et al., (2012) and Asikainen & Halttunen, (2000). The higher value of percentage uncertainty compared to the literature, concluded in the repeatability tests depict the variability in the measurements taken by these clamp-on ultrasonic flowmeters. This together with the uncertainty in the measurements of the venturi at high flowrate range limits the effectiveness of the proposed correction factor for the experimental setup.

Chapter 5

5 Conclusions and proposed future work

The novel contributions of the study conducted in this thesis are as follows:

- The designing of a numerical model in COMSOL software which simulates the working of a clamp-on ultrasonic flowmeter entirely which includes: A 3D fluid flow simulation inside a straight pipe and pipe with an elbow case, A 3D piezoelectric transducer's simulation that models the generation and reception of the ultrasonic wave, A 3D simulation of the propagation of the ultrasonic wave in the presence of a fluid flow in an ideal and non-ideal flow conditions.

- The ultrasonic wave's path of propagation and amplitude is not affected by the fluid flow structure due to pipe disturbances. The velocity vector magnitude and pressure of the ultrasonic signal is affected due to the local fluid flow velocity.

- A simple 1-D acoustic path analysis could roughly predict the measurement uncertainty due to asymmetric flow profile. This analysis can vary depending upon the number of points considered for velocity integration along the acoustic path. In practical applications there is no process which can be used to integrate velocity of the fluid along a pipe diameter or cross-section which is why estimating a correction factor for clamp-on ultrasonic flowmeters by using 1-D acoustic path analysis is not recommended.

- The uncertainty in the measurements of a clamp-on ultrasonic flowmeter (induced due to the secondary flow at x/d=1 downstream of the elbow) estimated from the numerical and experimental study are in accordance with each other.

- Estimation of the performance of an existing clamp-on ultrasonic flowmeter on a straight pipe and downstream of the elbow case helps to propose a correction factor

(which is specific to that type of clamp-on ultrasonic flowmeter installed in similar conditions) that reduces the uncertainty in the measurements.

Some general conclusions drawn from this study are as follows:

- The fluid flow downstream of a 90^0 elbow contains a secondary flow. This creates a low velocity region on the inner side of the elbow. This low velocity region surrounded by high velocity fluid flow generates TKE.

- The ultrasonic signal propagating inside a static fluid propagates with the speed of sound in the fluid whereas when the ultrasonic signal propagates through a moving fluid, the signal's velocity and pressure is attenuated depending upon the fluid's velocity.

- At x/d=1 downstream of the elbow, the low velocity region causes an uncertainty in the measurement of a clamp-on ultrasonic flowmeter.

- There is no considerable effect of flowmeter's orientation on the flowrate readings at the straight pipe and downstream of the elbow locations.

- The repeatability tests depict that the clamp-on ultrasonic flowmeters have a variability in the flowrate reading, primarily due to clamping and unclamping process and signal quality of the received signal, which does not allow for a further reduction in the measurement uncertainty of these meters at the downstream location. Due to this reason the applicability of these flowmeters is not recommended for a flowrate measurement with an accuracy of ±1%.

The following are some recommendations for the future work:

- This numerical model can also be used to simulate the behaviour of a clamp-on ultrasonic flowmeter downstream of pipe disturbances other than a 90^0 elbow.

- The manufacturers do not disclose the algorithm or correction factors that they use in the clamp-on ultrasonic flowmeters. Therefore, the algorithm of a clamp-on ultrasonic flowmeter can be studied by taking apart a flowmeter from the

experimental study. This would help to improve the repeatability and accuracy of the flowmeter. Similarly, a method could be proposed to include a correction factor into the algorithm of the clamp-on ultrasonic flowmeter.

The industry partner can gain an insight into the range of percentage uncertainty associated with the clamp-on ultrasonic flowmeters when installed downstream of a 90^0 elbow. The algorithms of existing clamp-on ultrasonic flowmeters can be improved to reduce the measurement uncertainty associated with these meters when installed in such operating conditions. The clamp-on ultrasonic flowmeters tested in the experimental study can be used with the proposed correction in practical applications where an accuracy of ±2% is allowable.

References

Asikainen, S., & Halttunen, J. (2000). Experiences of clamp-on ultrasonic flowmeter in small pipes. *10th IMEKO TC9 Conference on Flow Measurement*, 419–425.

Atkinson, P. (1976). A fundamental interpretation of ultrasonic Doppler velocimeters. *Ultrasound in Medicine & Biology*, *2*(2), 107–111. https://doi.org/10.1016/0301-5629(76)90018-1

Baker, R. C. (2000). Flow measurement handbook: industrial Designs, operating principles, performance, and applications. In *Flow Measurement Handbook* (1st ed.). Cambridge University Press. https://doi.org/10.1017/CBO9780511471100

Baker, R. C., & Morris, M. V. (1985). Positive-displacement meters for liquids. *Transactions of the Institute of Measurement and Control*, *7*(4), 209–220. https://doi.org/10.1177/014233128500700405

Bécherrawy, T. (2012). *Mechanical and electromagnetic vibrations and waves*. John Wiley & Sons, Inc. https://doi.org/10.1002/9781118586525

Bove. (2020). *B6 Lite VW ultrasonic water meter*. Bove Intelligent Technology Co., Ltd. https://www.bovetech.com/Products_1_UltrasonicWaterMeter.html

Calogirou, A., Boekhoven, J., & Henkes, R. A. W. . (2001). Effect of wall roughness changes on ultrasonic gas flowmeters. *Flow Measurement and Instrumentation*, *12*(3), 219–229. https://doi.org/10.1016/S0955-5986(01)00014-0

Chevaugeon, N., Hillewaert, K., Gallez, X., Ploumhans, P., & Remacle, J.-F. (2007). Optimal numerical parameterization of discontinuous Galerkin method applied to wave propagation problems. *Journal of Computational Physics*, *223*(1), 188–207. https://doi.org/10.1016/j.jcp.2006.09.005

Chevaugeon, N., Remacle, J.-F., Gallez, X., Ploumans, P., & Caro, S. (2005, May 23). Efficient discontinuous galerkin methods for solving acoustic problems. *11th AIAA/CEAS Aeroacoustics Conference*. https://doi.org/10.2514/6.2005-2823

Choi, H. M., Yoon, B. R., Kim, C. G., & Choi, Y. M. (2011). Evaluation of flowmeters for heat metering. *Flow Measurement and Instrumentation*, *22*(5), 475–481. https://doi.org/10.1016/j.flowmeasinst.2011.08.001

Computing, M. (2019). *USB-1208LS user guide*. https://www.mccdaq.com/pdfs/manuals/USB-1208LS.pdf

Dane, H. J., & Wilsack, R. (1999). Upstream pipe wall roughness influence on ultrasonic flow measurement. *North Sea Flow Measurement Workshop*. https://nfogm.no/wp-content/uploads/2019/02/1999-09-Upstream-pipe-wall-roughness-influence-on-ultrasonic-flow-measurement-Dane-Dordrecht.pdf

Dudalski, N. (2020). *Thermal energy metering: Theoretical model for glycol correction factors and experimental results*.

Dutta, P., Saha, S. K., Nandi, N., & Pal, N. (2016). Numerical study on flow separation in 90° pipe bend under high Reynolds number by k-ε modelling. *Engineering Science*

and Technology, an International Journal, *19*(2), 904–910. https://doi.org/10.1016/j.jestch.2015.12.005

Enayet, M. M., Gibson, M. M., Taylor, A. M. K. P., & Yianneskis, M. (1982). Laser-Doppler measurements of laminar and turbulent flow in a pipe bend. *International Journal of Heat and Fluid Flow*, *3*(4), 213–219. https://doi.org/10.1016/0142-727X(82)90024-8

Erturk, A., & Inman, D. J. (2011). *Piezoelectric energy harvesting* (First). John Wiley and Sons, Ltd. https://www.wiley.com/en-au/Piezoelectric+Energy+Harvesting-p-9781119991359

Frei, W. (2016). *Keeping track of element order in multiphysics models*.

Gaimc. (2018). *Single-jet water meter*. https://www.facebook.com/GAIMChina/photos/2201324750189959

Ghassemi, H., & Fasih, H. F. (2011). Application of small size cavitating venturi as flow controller and flow meter. *Flow Measurement and Instrumentation*, *22*(5), 406–412. https://doi.org/10.1016/j.flowmeasinst.2011.05.001

Gu, X., & Cegla, F. (2019). The effect of internal pipe wall roughness on the accuracy of Clamp-on ultrasonic flowmeters. *IEEE Transactions on Instrumentation and Measurement*, *68*(1), 65–72. https://doi.org/10.1109/TIM.2018.2834118

Hartogh, L. . (2018). *Today's residential faucets*. Plumbing & HVAC Staff. http://plumbingandhvac.ca/todays-residential-faucets/

Heritage, J. E. (1989). The performance of transit time ultrasonic flowmeters under good and disturbed flow conditions. *Flow Measurement and Instrumentation*, *1*(1), 24–30. https://doi.org/10.1016/0955-5986(89)90006-X

Herrick, J. F., & Anderson, J. A. (1959). Ultrasonic flowmeters. *IRE Transactions on Medical Electronics*, *ME-6*(4), 195–197. https://doi.org/10.1109/IRET-ME.1959.5007962

Ikarashi, Y., Uno, T., Yamagata, T., & Fujisawa, N. (2018). Influence of elbow curvature on flow and turbulence structure through a 90° elbow. *Nuclear Engineering and Design*, *339*(April), 181–193. https://doi.org/10.1016/j.nucengdes.2018.09.011

Internationale, O. (2006). *Water meters intended for the metering of cold potable water and hot water*.

Iooss, B., Lhuillier, C., & Jeanneau, H. (2002). Numerical simulation of transit-time ultrasonic flowmeters: uncertainties due to flow profile and fluid turbulence. *Ultrasonics*, *40*(9), 1009–1015. https://doi.org/https://doi.org/10.1016/S0041-624X(02)00387-6

Johnson, A. L., Benham, B. L., Eisenhauer, D. E., & Hotchkiss, R. H. (2001). Ultrasonic water measurement in irrigation pipelines with disturbed flow. *Transactions of the ASAE*, *44*(4). https://doi.org/10.13031/2013.6254

Jung, J. C., & Seong, P. H. (2005). Estimation of the flow profile correction factor of a transit-time ultrasonic flow meter for the feedwater flow measurement in a nuclear

power plant. *IEEE Transactions on Nuclear Science*, *52*(3), 714–718. https://doi.org/10.1109/TNS.2005.846879

Kelly, J. F., Marras, S., Zhao, X., & McGough, R. J. (2018). Linear and nonlinear ultrasound simulations using the discontinuous Galerkin method. *The Journal of the Acoustical Society of America*, *143*(4), 2438–2448. https://doi.org/10.1121/1.5032196

Kim, J., Yadav, M., & Kim, S. (2014). Characteristics of secondary flow induced by 90-degree elbow in turbulent pipe flow. *Engineering Applications of Computational Fluid Mechanics*, *8*(2), 229–239. https://doi.org/10.1080/19942060.2014.11015509

Kocis, S., & Figura, Z. (1996). *Ultrasonic Measurements and Technologies* (First). Chapman & Hall. https://doi.org/10.1007/978-1-4613-1199-7

Kritz, J. (1955). An ultrasonic flowmeter for liquids. *International Society of Automation*, *10 (2)*(Paper No. 55-16-3), 1912–1913.

Larraona, G. S., Rivas, A., & Ramos, J. C. (2008). Computational Modeling and Simulation of a Single-Jet Water Meter. *Journal of Fluids Engineering*, *130*(5). https://doi.org/10.1115/1.2911679

Launder, B. E., & Spalding, D. B. (1974). The numerical computation of turbulent flows. *Computer Methods in Applied Mechanics and Engineering*, *3*(2), 269–289. https://doi.org/https://doi.org/10.1016/0045-7825(74)90029-2

Li, X., Huang, Z., Meng, Z., Wang, B., & Li, H. (2009). Oil-water two-phase flow measurement using a venturi meter and an oval gear flowmeter. *Chemical Engineering Communications*, *197*(2), 223–231. https://doi.org/10.1080/00986440902938469

Lynnworth, L. . (1979). Ultrasonic flowmeters. *Physical Acoustics*, *14*, 407–525. https://doi.org/10.1016/B978-0-12-477914-3.50010-4

Lynnworth, L. C. (1981). Ultrasonic flowmeters. *Transactions of the Institute of Measurement and Control*, *3*(4), 217–223. https://doi.org/10.1177/014233128100300405

Mahadeva, D. V., Baker, R. C., & Woodhouse, J. (2009). Further studies of the accuracy of clamp-on transit-time ultrasonic flowmeters for liquids. *IEEE Transactions on Instrumentation and Measurement*, *58*(5), 1602–1609. https://doi.org/10.1109/TIM.2009.2012954

Marburg, S. (2002). Six boundary elements per wavelength: is that enough? *Journal of Computational Acoustics*, *10*(01), 25–51. https://doi.org/10.1142/S0218396X02001401

Marx, T. (2019). *Oval gear flowmeter overview*. https://www.macnaughtusa.com/flow-meter-overview-oval-gear/

Masasi, B., Frazier, R. S., & Taghvaeian, S. (2017). *Review and operational guidelines for portable ultrasonic flowmeters*. https://extension.okstate.edu/fact-sheets/review-and-operational-guidelines-for-portable-ultrasonic-flowmeters.html

Matikainen, L., Irons, G. A., Morala, E., & Chang, J. (1986). Ultrasonic system for the detection of transient liquid/gas interfaces using the pulse-echo technique. *Review of Scientific Instruments*, *57*(8), 1661–1666. https://doi.org/10.1063/1.1138546

McDonald, T. (2014). *What are Single Jet & Multi Jet Water Meters?* https://www.heattracing.co.uk/blog/article/what-are-single-jet-and-multi-jet-water-meters

Menter, F. R. (1994). Two-equation eddy-viscosity turbulence models for engineering applications. *AIAA Journal*, *32*(8), 1598–1605. https://doi.org/10.2514/3.12149

Merzkirch, W., Gersten, K., Peters, F., Vasanta Ram, V., von Lavante, E., & Hans, V. (2005). *Fluid mechanics of flow metering* (W. Merzkirch (ed.)). Springer Berlin Heidelberg. https://doi.org/10.1007/b138000

Miaki, Y., Yasuaki, A., & Takeshi, A. (1967). *Ultrasonic flow quantity measuring apparatus* (Patent No. US3329017A). United States patent office.

Mirshab, B. (2015). *Ultrasonic sensing for water flow meters and heat meters* (Issue April).

Moore, P. I., Brown, G. J., & Stimpson, B. P. (2000). Ultrasonic transit-time flowmeters modelled with theoretical velocity profiles: methodology. *Measurement Science and Technology*, *11*(12), 1802–1811. https://doi.org/10.1088/0957-0233/11/12/321

Mori, M., Tezuka, K., & Takeda, Y. (2006). Effects of inner surface roughness and asymmetric pipe flow on accuracy of profile factor for ultrasonic flow meter. *Volume 2: Thermal Hydraulics*, 761–767. https://doi.org/10.1115/ICONE14-89729

Morrison, G. L., Hall, K. R., Holste, J. C., Macek, M. L., Ihfe, L. M., DeOtte, R. E., & Terracina, D. P. (1994). Comparison of orifice and slotted plate flowmeters. *Flow Measurement and Instrumentation*, *5*(2), 71–77. https://doi.org/10.1016/0955-5986(94)90039-6

O'Banion, T. (2013). Coriolis: the direct approach to mass flow measurement. *Chemical Engineering Progress*, 41–46.

O'Neill, K. (2019). *Magnetic flowmeter basics*. Assured Automation. https://assuredautomation.com/news-and-training/magnetic-flow-meter-basics/

Omega. (2019). *Wet differential pressure transmitters*. Omega Engineering Inc. https://www.omega.com/en-us/pressure-measurement/pressure-transducers/p/PX409-WWDIF

Ono, A., Kimura, N., Kamide, H., & Tobita, A. (2011). Influence of elbow curvature on flow structure at elbow outlet under high Reynolds number condition. *Nuclear Engineering and Design*, *241*(11), 4409–4419. https://doi.org/10.1016/j.nucengdes.2010.09.026

Pierce, A. D. (1990). Wave equation for sound in fluids with unsteady inhomogeneous flow. *The Journal of the Acoustical Society of America*, *87*(6), 2292–2299. https://doi.org/10.1121/1.399073

Pierce, A. D. (2019). *Acoustics: An introduction to its physical principles and*

applications (Third). Springer International Publishing. https://doi.org/10.1007/978-3-030-11214-1

Piezo. (2020). *Material properties - piezo support*. https://support.piezo.com/article/62-material-properties

Röhrig, R., Jakirlić, S., & Tropea, C. (2015). Comparative computational study of turbulent flow in a 90° pipe elbow. *International Journal of Heat and Fluid Flow, 55*, 120–131. https://doi.org/10.1016/j.ijheatfluidflow.2015.07.011

Russell, D. A. (2016). *Acoustics and vibration animations*. The Pennsylvania State University. https://www.acs.psu.edu/drussell/demos/waves/wavemotion.html

Rutten, F., Meinke, M., & Schroder, W. (2001). Large-eddy simulations of 90° pipe bend flows. *Journal of Turbulence, 2*, N3. https://doi.org/10.1088/1468-5248/2/1/003

Sanderson, M. L. (1982). Electromagnetic and ultrasonic flowmeters: their present states and future possibilities. *Electronics and Power, 28*(2), 161–164. https://doi.org/10.1049/ep.1982.0071

Sanderson, M. L., & Yeung, H. (2002). Guidelines for the use of ultrasonic non-invasive metering techniques. *Flow Measurement and Instrumentation, 13*, 125–142.

Satomura, S. (1959). Study of the flow patterns in peripheral arteries by ultrasonics. *Journal of the Acoustical Society of Japan*, *15*, 151–158.

Schlichting, H., & Gersten, K. (1979). *Boundary-layer theory* (Seventh). McGraw Hill.

Schwery, A., Staubli, T., & Abgottspon, A. (2012). *Field and laboratory experience with a clamp-on acoustic transit time flowmeter*.

Sentec. (2021). *FHM500 external card ultrasonic flow watch Snap on ultrasonic flowmeter*. Chengdu Sentec Technology Co., Ltd. https://www.cdsentec.com/productinfo/430555.html

Shekhter, Y. L. (2011). *Flow metering*. A-to-Z Guide to Thermodynamics, Heat and Mass Transfer, and Fluids Engineering; Begellhouse. https://doi.org/10.1615/AtoZ.f.flow_metering

Shercliff, J. A. (1962). *The theory of electromagnetic flow measurement* (First). Cambridge University Press.

Sifferman, T. R., Kemp, L. J., & Chilingarian, G. V. (1989). Chapter 2 Flow Rate Measurements. In *Surface Operations in Petroleum Production, II* (pp. 13–59). Elsevier B.V. https://doi.org/10.1016/S0376-7361(08)70501-6

Spalart, P., & Allmaras, S. (1992). A one-equation turbulence model for aerodynamic flows. *30th Aerospace Sciences Meeting and Exhibit*, *439*. https://doi.org/10.2514/6.1992-439

Standards, B. (2003). *Measurement of fluid flow by means of pressure differential devices inserted in circular cross-section conduits running full*.

Stoker, D. M., Barfuss, S. L., & Johnson, M. C. (2012). Ultrasonic flow measurement for pipe installations with nonideal conditions. *Journal of Irrigation and Drainage Engineering, 138*(11), 993–998. https://doi.org/10.1061/(ASCE)IR.1943-

4774.0000486

Sudo, K., Sumida, M., & Hibara, H. (1998). Experimental investigation on turbulent flow in a circular-sectioned 90-degree bend. *Experiments in Fluids*, *25*(1), 42–49. https://doi.org/10.1007/s003480050206

Sultan, G., & Hemp, J. (1989). Modelling of the Coriolis mass flowmeter. *Journal of Sound and Vibration*, *132*(3), 473–489. https://doi.org/10.1016/0022-460X(89)90640-8

Taguchi, S., Ikarashi, Y., Yamagata, T., Fujisawa, N., & Inada, F. (2018). Mass and momentum transfer characteristics in 90° elbow under high Reynolds number. *International Communications in Heat and Mass Transfer*, *90*, 103–110. https://doi.org/10.1016/j.icheatmasstransfer.2017.11.006

Tan, L., Zhu, B., Wang, Y., Cao, S., & Liang, K. (2014). Turbulent flow simulation using large eddy simulation combined with characteristic-based split scheme. *Computers and Fluids*, *94*, 161–172. https://doi.org/10.1016/j.compfluid.2014.01.037

Tanaka, M., Ohshima, H., & Monji, H. (2009). Numerical investigation of flow structure in pipe elbow with large eddy simulation approach. *Volume 3: Design and Analysis*, *3*, 449–458. https://doi.org/10.1115/PVP2009-77598

Tanaka, & Ohshima, H. (2012). Numerical Investigation on Large Scale Eddy Structure in Unsteady Pipe Elbow Flow at High Reynolds Number Conditions with Large Eddy Simulation Approach. *Journal of Power and Energy Systems*, *6*(2), 210–228. https://doi.org/10.1299/jpes.6.210

Terés-Zubiaga, J., Pérez-Iribarren, E., González-Pino, I., & Sala, J. M. (2018). Effects of individual metering and charging of heating and domestic hot water on energy consumption of buildings in temperate climates. *Energy Conversion and Management*, *171*, 491–506. https://doi.org/10.1016/j.enconman.2018.06.013

Thompson, E. (1978). Two beam ultrasonic flow measurement. In *Imperial College of Science and Technology, University of London*.

Tiersten, H. F. (1988). *IEEE standard on piezoelectricity: an american national standard*. Institute of Electrical and Electronics Engineers.

Vandervort, D. (2021). *Pipes & home plumbing for DIY plumbers*. https://www.hometips.com/how-it-works/pipes-water-supply.html

Walter, D., Mastaller, M., & Klingel, P. (2018). Accuracy of single-jet and multi-jet water meters under the influence of the filling process in intermittently operated pipe networks. *Water Supply*, *18*(2), 679–687. https://doi.org/10.2166/ws.2017.149

Wang, Y., Dong, Q., & Wang, P. (2015). Numerical Investigation on Fluid Flow in a 90-Degree Curved Pipe with Large Curvature Ratio. *Mathematical Problems in Engineering*, *2015*, 1–12. https://doi.org/10.1155/2015/548262

Wilcox, D. C. (2006). Turbulence modelling for CFD. In *Turbulence Modeling for CFD* (3rd ed.). http://www.dcwindustries.com

Worch, A. (1998). A clamp-on ultrasonic cross correlation flow meter for one-phase

flow. *Measurement Science and Technology*, *9*(4), 622–630. https://doi.org/10.1088/0957-0233/9/4/010

Xu, Y. (1992). A model for the prediction of turbine flowmeter performance. *Flow Measurement and Instrumentation*, *3*(1), 37–43. https://doi.org/10.1016/0955-5986(92)90014-V

Yalcin, M. Y. (2008). *Water meters*. https://commons.wikimedia.org/wiki/File:Su_sayacı-0103.jpg

Zanker, K. J. (1999). The effects of Reynolds number, wall roughness, and profile asymmetry on single-and multi-path ultrasonic meters. *North Sea Flow Measurement Workshop*. https://nfogm.no/wp-content/uploads/2019/02/1999-10-The-Effects-of-Reynolds-Number-Wall-Roughness-and-Profile-Asymmetry-on-Single-and-Multi-Path-USM-Zanker-Daniel.pdf

Zhang, H., Guo, C., & Lin, J. (2019). Effects of velocity profiles on measuring accuracy of Transit-time ultrasonic flowmeter. *Applied Sciences*, *9*(8), 1648. https://doi.org/10.3390/app9081648

Appendices

Appendix 1 Numerical simulation steps and parameters

1 Global Definitions

GLOBAL SETTINGS

USED PRODUCTS

COMSOL Multiphysics
Acoustics Module
CFD Module

1.1 PARAMETERS

PARAMETERS 1

Name	Expression	Value	Description
rho0	998[kg/m^3]	998 kg/m³	Background mean flow density
c0	1481[m/s]	1481 m/s	Speed of sound
f0	1e6[Hz]	1E6 Hz	Carrier signal frequency
omega0	2*pi*f0	6.2832E6 Hz	Carrier signal angular frequency
T0	1/f0	1E−6 s	Carrier signal period
lam0	c0/f0	0.001481 m	Carrier signal wavelength
alpha	30[deg]	0.5236 rad	Transducer tube pitch angle
V0	50[V]	50 V	Driving voltage

Name	Expression	Value	Description
alpha_dmp	3.0875e5	3.0875E5	Rayleigh mass damping parameter
beta_dmp	2.1944e-8	2.1944E−8	Rayleigh stiffness damping parameter
pipeod	1.05[inch]	0.02667 m	
pipeid	0.82[inch]	0.020828 m	
wlen	14[mm]	0.014 m	
wwid	3[mm]	0.003 m	
whei	(3*sqrt(3))/2	2.5981	
pipethick	0.115[inch]	0.002921 m	
len	1.5*pipeod	0.040005 m	
gap	15[mm]	0.015 m	
Zsteel	45.45e6[rayl]	4.545E7 rayl	
Zwat	1.5e6[rayl]	1.5E6 rayl	
Zmatch	sqrt(Zsteel*Zwat)	8.2568E6 rayl	
ab	2*lam0	0.002962 m	
areapipe	pi*((pipeid/2)^2)	3.4071E−4 m²	
flowrate	(1/3600)[m^3/s]	2.7778E−4 m³/s	

Name	Expression	Value	Description
vel_inlet	flowrate/areapipe	0.81529 m/s	
piezoangleup	sin(alpha)	0.5	upstream piezo 25 degree
h1	hyp*sin(alpha)	0.0025 m	corresponding height
hyp	5[mm]	0.005 m	
c_gel	1580[m/s]	1580 m/s	
ac_height	0.5[mm]	5E−4 m	
base	cos(alpha)*hyp	0.0043301 m	
ang1	26.75[deg]	0.46688 rad	
hmax	lam0/6	2.4683E−4 m	
dd	8.33[mm]	0.00833 m	

1.2 FUNCTIONS

1.2.1 Rectangle 1

Function name	rect_fct
Function type	Rectangle

1.2.2 Analytic 1

Function name	voltage_pulse_fct
Function type	Analytic

2 Component 1

2.1 DEFINITIONS

2.1.1 Nonlocal Couplings

LINEAR EXTRUSION 1

Coupling type	Linear extrusion
Operator name	linext1

SELECTION

Geometric entity level	Boundary
Selection	Geometry geom1: Dimension 2: Boundary 31

2.1.2 Coordinate Systems

BOUNDARY SYSTEM 1

Coordinate system type	Boundary system
Tag	sys1

COORDINATE NAMES

First	Second	Third
t1	t2	n

2.2 GEOMETRY 1

UNITS

Length unit	mm
Angular unit	deg

2.3 MATERIALS

2.3.1 Water, liquid

SELECTION

Geometric entity level	Domain
Selection	Geometry geom1: Dimension 3: All domains

2.4 TURBULENT FLOW, SST

EQUATIONS

$$\rho(\mathbf{u3}\cdot\nabla)\mathbf{u3}=\nabla\cdot[-p3\mathbf{I}+\mathbf{K}]+\mathbf{F}$$
$$\rho\nabla\cdot\mathbf{u3}=0$$
$$\mathbf{K}=(\mu+\mu_T)\left(\nabla\mathbf{u3}+(\nabla\mathbf{u3})^T\right)$$
$$\rho(\mathbf{u3}\cdot\nabla)k=\nabla\cdot\left[(\mu+\mu_T\sigma_k)\nabla k\right]+P-\beta_0^*\rho\omega k$$
$$\rho(\mathbf{u3}\cdot\nabla)\omega=\nabla\cdot\left[(\mu+\mu_T\sigma_\omega)\nabla\omega\right]+\frac{\gamma}{\mu_T}\rho P-\rho\beta_0\omega^2+2(1-f_{v1})\frac{\sigma_{\omega2}\rho}{\omega}\nabla k\cdot\nabla\omega,\quad \omega=\mathrm{om}$$
$$\nabla G\cdot\nabla G+\sigma_w G(\nabla\cdot\nabla G)=(1+2\sigma_w)G^4,\quad \ell_w=\frac{1}{G}-\frac{\ell_{ref}}{2}$$
$$\mu_T=\rho\frac{a_1 k}{max(a_1\omega,Sf_{v2})},\ S=\sqrt{2\mathbf{S}:\mathbf{S}},\ \mathbf{S}=\frac{1}{2}\left(\nabla\mathbf{u3}+(\nabla\mathbf{u3})^T\right)$$
$$P=min(P_k,10\rho\beta_0\omega k)$$
$$P_k=\mu_T\left[\nabla\mathbf{u3}:\left(\nabla\mathbf{u3}+(\nabla\mathbf{u3})^T\right)\right]$$
$$\phi=f_{v1}\phi_1+(1-f_{v1})\phi_2,\ \phi=\beta,\gamma,\sigma_k,\sigma_\omega$$

FEATURES

Name	Level
Fluid Properties 1	Domain
Initial Values 1	Domain
Wall 1	Boundary
Inlet 1	Boundary
Outlet 1	Boundary

2.5 MESH 1

3 Component 2

3.1 DEFINITIONS

3.1.1 Nonlocal Couplings

IDENTITY MAPPING 1

Coupling type	Identity mapping
Operator name	idmap1

SELECTION

Geometric entity level	Boundary
Selection	Geometry geom2: Dimension 2: Boundary 13

3.1.2 Coordinate Systems

BOUNDARY SYSTEM 2

Coordinate system type	Boundary system
Tag	sys2

COORDINATE NAMES

First	Second	Third
t1	t2	n

SYS_PZT

Coordinate system type	Base vector system
Tag	sys4

COORDINATE NAMES

First	Second	Third
x1	x2	x3

BASE VECTORS

	x	y	z
x1	cos(alpha)	0	-sin(alpha)
x2	0	1	0
x3	sin(alpha)	0	cos(alpha)

SIMPLIFICATIONS

Description	Value
Assume orthonormal	On

3.1.3 Artificial Domains

PERFECTLY MATCHED LAYER 1

Tag	pml1

SELECTION

Geometric entity level	Domain
Selection	Geometry geom2: Dimension 3: Domain 2

3.2 GEOMETRY 2

UNITS

Length unit	mm
Angular unit	deg

3.3 MATERIALS

3.3.1 Water, liquid

SELECTION

Geometric entity level	Domain
Selection	Geometry geom2: Dimension 3: Domains 2–3

3.3.2 Lead Zirconate Titanate (PZT-5H)

SELECTION

Geometric entity level	Domain
Selection	Geometry geom2: Dimension 3: Domain 1

3.3.3 Acrylic plastic

SELECTION

Geometric entity level	Domain
Selection	Geometry geom2: Dimension 3: Domain 5

3.3.4 Structural steel

SELECTION

Geometric entity level	Domain
Selection	Geometry geom2: Dimension 3: Domain 4

3.4 PRESSURE ACOUSTICS, TRANSIENT

EQUATIONS

$$\frac{1}{\rho c^2}\frac{\partial^2 p_t}{\partial t^2} + \nabla \cdot \left(-\frac{1}{\rho}\left(\nabla p_t - \mathbf{q}_d\right)\right) = Q_m$$

$$p_t = p + p_b$$

FEATURES

Name	Level
Transient Pressure Acoustics Model 1	Domain
Sound Hard Boundary (Wall) 1	Boundary
Initial Values 1	Domain

3.5 SOLID MECHANICS

EQUATIONS

$$0 = \nabla \cdot S + \mathbf{F}_V$$

FEATURES

Name	Level
Linear Elastic Material 1	Domain
Free 1	Boundary
Initial Values 1	Domain
Piezoelectric Material 1	Domain
Roller 1	Boundary

3.6 ELECTROSTATICS

EQUATIONS

$$\nabla \cdot \mathbf{D} = \rho_v$$
$$\mathbf{E} = -\nabla V$$

FEATURES

Name	Level
Charge Conservation 1	Domain
Zero Charge 1	Boundary

Name	Level
Initial Values 1	Domain
Charge Conservation, Piezoelectric 1	Domain
Ground 1	Boundary
Electric Potential 1	Boundary

3.7 MULTIPHYSICS

3.7.1 Piezoelectric Effect 3

3.7.2 Acoustic-Structure Boundary 1

EQUATIONS

Exterior:

$$-\mathbf{n}\cdot\left(\frac{1}{\rho_c}(\nabla p_t - \mathbf{q}_d)\right) = -\mathbf{n}\cdot\mathbf{u}_{tt}$$

$$\mathbf{F}_A = p_t\mathbf{n}$$

Interior:

$$-\mathbf{n}\cdot\left(\frac{1}{\rho_c}(\nabla p_t - \mathbf{q}_d)\right)_{up} = -\mathbf{n}\cdot\mathbf{u}_{tt}$$

$$-\mathbf{n}\cdot\left(\frac{1}{\rho_c}(\nabla p_t - \mathbf{q}_d)\right)_{down} = -\mathbf{n}\cdot\mathbf{u}_{tt}$$

$$\mathbf{F}_A = p_{t_{down}}\mathbf{n} - p_{t_{up}}\mathbf{n}$$

3.8 MESH 2

4 Component 3

4.1 DEFINITIONS

4.1.1 Selections

REC POINT

Selection type
Explicit

Selection
Point 61

4.1.2 Nonlocal Couplings

IDENTITY MAPPING 2

Coupling type	Identity mapping
Operator name	idmap2

SELECTION

Geometric entity level	Boundary
Selection	Geometry geom3: Dimension 2: Boundaries 44, 46

4.1.3 Coordinate Systems

BOUNDARY SYSTEM 3

Coordinate system type	Boundary system
Tag	sys3

COORDINATE NAMES

First	Second	Third
t1	t2	n

4.1.4 Artificial Domains

ABSORBING LAYER 1

Tag	ab1

SELECTION

Geometric entity level	Domain
Selection	Geometry geom3: Dimension 3: Domains 1, 10

4.2 GEOMETRY 3

UNITS

Length unit	mm
Angular unit	deg

4.3 MATERIALS

4.3.1 Acrylic plastic

SELECTION

Geometric entity level	Domain
Selection	Geometry geom3: Dimension 3: Domains 4–5, 8

4.3.2 Structural steel

SELECTION

Geometric entity level	Domain
Selection	Geometry geom3: Dimension 3: Domains 3, 7

4.3.3 Water, liquid

SELECTION

Geometric entity level	Domain
Selection	Geometry geom3: Dimension 3: Domains 1–2, 6, 10

4.3.4 Lead Zirconate Titanate (PZT-5H)

SELECTION

Geometric entity level	Domain
Selection	Geometry geom3: Dimension 3: Domain 9

4.4 TURBULENT FLOW, K-Ω 2

EQUATIONS

$$\rho(\mathbf{u2}\cdot\nabla)\mathbf{u2}=\nabla\cdot[-p2\mathbf{I}+\mathbf{K}]+\mathbf{F}$$
$$\rho\nabla\cdot\mathbf{u2}=0$$
$$\mathbf{K}=(\mu+\mu_T)\left(\nabla\mathbf{u2}+(\nabla\mathbf{u2})^T\right)$$
$$\rho(\mathbf{u2}\cdot\nabla)k2=\nabla\cdot\left[\left(\mu+\mu_T\sigma_k^*\right)\nabla k2\right]+P_k - \beta_0^*\rho\omega k2$$
$$\rho(\mathbf{u2}\cdot\nabla)\omega=\nabla\cdot\left[(\mu+\mu_T\sigma_\omega)\nabla\omega\right]+\alpha\frac{\omega}{k2}P_k - \rho\beta_0\omega^2,\quad \omega=\mathrm{om2}$$
$$\mu_T=\rho\frac{k2}{\omega}$$
$$P_k=\mu_T\left[\nabla\mathbf{u2}:\left(\nabla\mathbf{u2}+(\nabla\mathbf{u2})^T\right)\right]$$

FEATURES

Name	Level
Fluid Properties 1	Domain
Initial Values 1	Domain
Wall 1	Boundary
Inlet 1	Boundary
Outlet 1	Boundary

4.5 CONVECTED WAVE EQUATION, TIME EXPLICIT

EQUATIONS

$$\frac{\partial\rho}{\partial t}+(\mathbf{u}_0\cdot\nabla)\rho+(\mathbf{u}\cdot\nabla)\rho_0+\rho\nabla\cdot\mathbf{u}_0+\rho_0\nabla\cdot\mathbf{u}=f_p$$
$$\frac{\partial\mathbf{u}}{\partial t}+(\mathbf{u}_0\cdot\nabla)\mathbf{u}+(\mathbf{u}\cdot\nabla)\mathbf{u}_0+\frac{1}{\rho_0}\nabla p-\frac{\rho}{\rho_0^2}\nabla p_0=\mathbf{f}_v$$
$$\rho=\frac{p}{c_0^2}$$
$$p=\mathrm{p4}$$
$$\mathbf{u}=\mathrm{u4}$$

FEATURES

Name	Level
Convected Wave Equation Model 1	Domain
Sound Hard Wall 1	Boundary
Initial Values 1	Domain
Acoustic Impedance 1	Boundary
Acoustic Impedance 2	Boundary
Normal Velocity 1	Boundary

4.6 SOLID MECHANICS 2

EQUATIONS

$$0 = \nabla \cdot S + \mathbf{F}_V$$

FEATURES

Name	Level
Linear Elastic Material 1	Domain
Free 1	Boundary
Initial Values 1	Domain
Boundary Load 1	Boundary
Piezoelectric Material 1	Domain
Roller 1	Boundary

4.7 ELECTROSTATICS 2

EQUATIONS

$$\nabla \cdot \mathbf{D} = \rho_v$$

$$\mathbf{E} = -\nabla V$$

FEATURES

Name	Level
Charge Conservation 1	Domain
Zero Charge 1	Boundary
Initial Values 1	Domain
Charge Conservation, Piezoelectric 1	Domain
Ground 1	Boundary
Floating Potential 1	Boundary

4.8 MULTIPHYSICS

4.8.1 Piezoelectric Effect 2

4.8.2 Background Fluid Flow Coupling 1

4.9 MESHES

4.9.1 Mesh 3-cfd

4.9.2 Mesh 4-acoustic

4.9.3 Mesh 5-receiver

5 Study 1-cfd pipe

COMPUTATION INFORMATION

Computation time	2 h 40 min 24 s

5.1 WALL DISTANCE INITIALIZATION

STUDY SETTINGS

Description	Value
Include geometric nonlinearity	Off

MESH

Feature	Value
Geometry 1	mesh1
Geometry 2	nomesh
Geometry 3	nomesh

PHYSICS AND VARIABLES SELECTION

Physics interface	Discretization
Turbulent Flow, SST (spf)	physics

MESH SELECTION

Geometry	Mesh
Geometry 1 (geom1)	mesh1
Geometry 2 (geom2)	nomesh
Geometry 3 (geom3)	nomesh

5.2 STATIONARY

STUDY SETTINGS

Description	Value
Include geometric nonlinearity	Off

MESH

Feature	Value
Geometry 1	mesh1
Geometry 2	nomesh
Geometry 3	nomesh

PHYSICS AND VARIABLES SELECTION

Physics interface	Discretization
Turbulent Flow, SST (spf)	physics

MESH SELECTION

Geometry	Mesh
Geometry 1 (geom1)	mesh1
Geometry 2 (geom2)	nomesh
Geometry 3 (geom3)	nomesh

6 Study 2-cfd flowmeter

COMPUTATION INFORMATION

Computation time	26 min 58 s

6.1 STATIONARY

STUDY SETTINGS

Description	Value
Include geometric nonlinearity	Off

VALUES OF DEPENDENT VARIABLES

Description	Value
Settings	User controlled
Method	Solution
Study	Study 1 - cfd pipe

MESH

Feature	Value
Geometry 1	mesh1
Geometry 2	nomesh
Geometry 3	mesh3

PHYSICS AND VARIABLES SELECTION

Physics interface	Discretization
Turbulent Flow, k-ω 2 (spf2)	physics

MESH SELECTION

Geometry	Mesh
Geometry 1 (geom1)	mesh1
Geometry 2 (geom2)	nomesh
Geometry 3 (geom3)	mesh3

7 Study 3-map

COMPUTATION INFORMATION

Computation time	3 min 16 s

7.1 MAPPING

STUDY SETTINGS

Description	Value
Include geometric nonlinearity	Off

SOLUTION TO MAP

Description	Value
Study	Study 2 - cfd flowmeter

MESH

Feature	Value
Geometry 1	nomesh
Geometry 2	nomesh
Geometry 3	mesh4

MESH SELECTION

Geometry	Mesh
Geometry 1 (geom1)	nomesh
Geometry 2 (geom2)	nomesh
Geometry 3 (geom3)	mesh4

8 Study 4-transmitter

COMPUTATION INFORMATION

Computation time	14 h 57 min 4 s

8.1 TIME DEPENDENT

Times	Unit
range(0,T0/5,20*T0)	s

STUDY SETTINGS

Description	Value
Include geometric nonlinearity	Off

STUDY SETTINGS

MESH

Feature	Value
Geometry 1	nomesh
Geometry 2	mesh2
Geometry 3	nomesh

PHYSICS AND VARIABLES SELECTION

Physics interface	Discretization
Pressure Acoustics, Transient (actd)	physics
Solid Mechanics (solid)	physics
Electrostatics (es)	physics

MESH SELECTION

Geometry	Mesh
Geometry 1 (geom1)	nomesh
Geometry 2 (geom2)	mesh2

Geometry	Mesh
Geometry 3 (geom3)	nomesh

9 Study 5-cwe

COMPUTATION INFORMATION

Computation time	14 h 44 min 9 s

9.1 TIME DEPENDENT

Times	Unit
range(0,T0,50*T0)	s

STUDY SETTINGS

Description	Value
Include geometric nonlinearity	Off

STUDY SETTINGS

VALUES OF DEPENDENT VARIABLES

Description	Value
Settings	User controlled
Method	Solution
Study	Study 3 - map

MESH

Feature	Value
Geometry 1	nomesh
Geometry 2	mesh2
Geometry 3	mesh4

PHYSICS AND VARIABLES SELECTION

Physics interface	Discretization
Convected Wave Equation, Time Explicit (cwe)	physics

MESH SELECTION

Geometry	Mesh
Geometry 1 (geom1)	nomesh
Geometry 2 (geom2)	mesh2
Geometry 3 (geom3)	mesh4

10 Study 6-receiver

COMPUTATION INFORMATION

Computation time	

10.1 TIME DEPENDENT

Times	Unit
range(30*T0,T0/1000,50*T0)	s

STUDY SETTINGS

Description	Value
Include geometric nonlinearity	Off

STUDY SETTINGS

MESH

Feature	Value
Geometry 1	nomesh
Geometry 2	nomesh
Geometry 3	mesh5

PHYSICS AND VARIABLES SELECTION

Physics interface	Discretization
Solid Mechanics 2 (solid2)	physics
Electrostatics 2 (es2)	physics

MESH SELECTION

Geometry	Mesh
Geometry 1 (geom1)	nomesh
Geometry 2 (geom2)	nomesh
Geometry 3 (geom3)	mesh5

Curriculum Vitae

Name:	Muhammad Ali
Post-secondary Education and Degrees:	Institute of Space Technology Islamabad, Pakistan 2014-2018 B.S. The University of Western Ontario London, Ontario, Canada 2019-2022 MESc.
Related Work Experience	Teaching Assistant The University of Western Ontario 2021-2021